

**Determination of the top-quark pole mass
using $t\bar{t}+1$ -jet events
with the ATLAS detector at the LHC**

Ph. D. thesis dissertation by

Adrián Irlles Quiles

under the supervision of

Juan Fuster Verdú y Peter Uwer

DOCTORADO EN FÍSICA

Diciembre 2014



VNIVERSITAT
D VALÈNCIA

FACULTAT DE FÍSICA

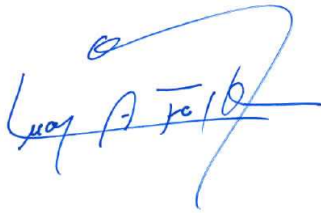
DEPARTAMENT DE FÍSICA ATÒMICA, MOLECULAR I NUCLEAR

Dr. Juan Antonio Fuster Verdú, *Profesor de Investigación, CSIC*,
Dr. Peter Uwer, *Professor at Humboldt-Universität zu Berlin*.

CERTIFICAN:

Que la presente memoria: “**Determination of the top-quark pole mass using $t\bar{t}$ +1-jet events with the ATLAS detector at the LHC.**” ha sido realizada bajo nuestra dirección en el Departamento de Física Atómica, Molecular y Nuclear de la Universidad de Valencia por Don Adrián Irlles Quiles y constituye su tesis para optar al grado de Doctor en Física.

Y para que así conste, firmamos el presente Certificado.



Firmado
Dr. Juan A. Fuster Verdú



Firmado
Dr. Peter Uwer

Declaration

This report is submitted to the University of Valencia for its evaluation and constitutes the work of my own PhD thesis. The results presented in this document are due to my own research. Explicit references are made when results from other studies are used. These results have not been presented elsewhere for the purpose of any other academic qualification.

Adrián Irlles Quiles.

It is not down on any map; true places never are.

I will have no man in my boat - said Starbuck -
who is not afraid of a whale.

[...] so that far from having lost his strength,
Ahab, to that one end, did now possess a thousand fold
more potency than ever he had sanely brought
to bear upon any one reasonable object.

Herman Melville, Moby Dick

Water is taught by thirst.
Land — by the Oceans passed.
Transport — by throe —
Peace — by its battles told —
Love, by Memorial Mold,
Birds, by the Snow

Emily Dickinson

Para mis abuel@s y, en especial,
para el verdadero *A. I. M.*:
aun te debo la nieve.

Acknowledgements/Agradecimientos

I have met so many people who participated in this project (called my life, my thesis, etc..) in one or other way. This fact, together with my bad memory, makes me to ask for your forgiveness before starting the section (yes, I know, to warn you before starting is a bit coward-like attitude..). So, if you think that your name should be here and that I am being unfair with you... probably you are right: I owe you one.

As I cannot be fair in the order of the acknowledgments, I am trying to be the most arbitrary possible:

First I want to thank to the University of Valencia and CSIC, both agglutinated at IFIC institution that support me academically, institutionally and economically and that allowed me to be part of CERN and, specifically, of the ATLAS collaboration. Thanks to all the people from IFIC secretary's office (Luis, Paqui(s), Amparo(s), Ana, Teresa, Jose, Pilar ...) and from University of Valencia's secretary's office for helping me with to deal with the nightmare of the bureaucracy. Thanks to Francisco Botella, director of IFIC, which allowed me to collaborate in the Theoretical Physics department before starting my PhD and made my life easier during my PhD period. Thanks to Eduardo Ros, one of the first colleagues I met at IFIC who always make me feel comfortable in his group. Thanks to all the people from the *Silici* group which supported and accompanied me all this time: Salva, Susana, Vasia, Marcel, Carlos, Carlos Escobar, Maria Jose and specially to Carmen for her support and patience that made possible my stay here and this work. Thanks also to Toni Ferrer for not doubting in helping me with the ATLAS bureaucracy when I was stunned like Josef K. Thanks to all the GRID IFIC people (Pepe, Santi, Javi, Álvaro...) for not giving me up for lost. Thanks to Rosa, Amparo, Rosario for all the logistic support and for making my stay at IFIC more comfortable. Thanks to Ximo and Carlos and all people from the IT departement for all the technical support and for their patience. Of course, thanks also to all the *non-seniors*: thanks to Carlos and Regina for helping me during my first summer at CERN; thanks to all the ADN-barbacues-(etc) people (from IFIC and from outside) Luis, Vicky, Tito, Neus, Javi, Josu and Josuvi, etc etc etc; thanks to all my colleagues of beer at the R1; thanks to my shift-partners Emma, Teresa and Maria; thanks to Maria (again) and Dani for being such honest and humble people; thanks to Miguel for all your help with C++ and for all the fun moments outside the office (and thanks for survive all your accidents!); thanks to the *chachis* for sharing the *bilis* but also good moments with me; and thanks to all of you that were around during my PhD. Thanks to all of you that saw me blaming against everything after a hard work day. Thanks to my lunch partners: Javi, JP, Umberto, Urmila, Carles, Juande, etc for giving me a breath every day. This fresh air every lunch charged my batteries every day. Thanks also to all people from Peter Uwer's group (Phillip, Mohammad, Olf,...) for making me feel so much recomfortable in my shorts (or not as shorts) stays in Berlin. Thanks for

all your comprehension and for all the help with bureaucracy, logistics and general life in there. A part of the hard work, I really had happy times in Berlin.

I cannot forget Ian Brock, Oleg Brandt, Stefanie Adomeit, Kevin Kroeninger as top quark mass conveners. Nor Markus Cristianzani, Maria Jose Costa, Tancredi Carli and Alison Alister as top quark group conveners. Nor Giorgio Cortiana, Borut Kersevan, Markus Wosbich and Christian Schwanenberger as the editorial board that accompanied us during last months. Thanks to all of you for your interest and all your suggestions, for your advice and your comments. I confess that (a few times) it has been hard (really really hard), but I really know that the work presented here is much better now than some months ago and this is due, in a large extent, thanks to all your comments. Also thanks to other members of the ATLAS collaboration that not being directly involved in this analysis as conveners or editorial board members have been very important to it: William Bell, Mark Owen, Stefan Kluth, Richard Hawking, etc... In general, thanks to all ATLAS and LHC people, that make possible that ATLAS works every day.

Of course, I want to thank to Simone Alioli, Sven-Olaf Moch, Marcel Vos and Patricia Fernández. Without them this work wouldn't be possible at all. Thanks to Simone and Sven for all your patience explaining me ... such a lot of things. I have really learned very much from you and I feel so grateful for that. I think that, this times of so much specialization and work in big collaborations, this kind of communication between theoreticians and experimentalists is not as common as it would be desired. I feel very lucky for that. Thanks to Marcel for all your help during all my PhD: I have asked you such a lot of things (about such a lot of topics) and I always had an answer and help from your side. Thanks to Patricia for understanding my codes, and sorry for the twiki (it is not my fault!). I know that I have not spent a lot of time helping you... but I hope that you learned a bit from me... (I mean about physics).

Last, but not least, I have the imperious need to thank Peter Uwer and Juan Fuster. It is clear that without them, this work would not even exist. I remember first times when we went to conferences or meetings, that I was completely convinced on these things about the top-quark mass issues: for me was so obvious, Juan told me and I did not doubt a second! the top-quark mass that people was measuring was not the pole mass. In most of the forums, specially in experimentalist forums, this topic was not started to be considered at all. I started feeling like Ismael in the Pequod: following a crazy captain in the search of an assassin whale that might be just a myth. But Juan was completely sure and he started convincing people that Moby Dick exists and that we were ready to kill it and come back home with its dead body in a big box (not like Ahab). Since then, we had a long journey, and finally here we are. I have learn a lot of physics from Peter and Juan, from ATLAS colleagues and from other physicists but, for me, this is only the tip of the iceberg of what I got during this time. Thanks Juan, thanks Peter, thanks for the journey.

Gracias Juan por ser, a parte de director, amigo. Gracias por tu humanidad.

Y como digo, esto no va sobre física, va sobre vosotros y sobre mi. Va sobre la gente. Sobre lo que traemos, recogemos, nos llevamos y sobre lo que dejamos. Va sobre los lugares que son nuestros. Va sobre Valencia que me ha dado una cantidad enorme de gente a la que quiero, que están aquí o fuera, y que a lo mejor os tengo un

poco olvidados porque soy un desastre con las distancias. Hoy sois mi hogar, porque así lo habéis hecho vosotros. Se que si empiezo a nombraros a todos, no acabaré... pero que os encontraréis en cualquiera de los lugares que menciono, cualquiera de los lugares que me traen un trocito de vosotros cuando lo veo o recuerdo. Como cuando paso por Xuquer, o por el Jack el Tuerto, o por el Picasso, o por Honduras, o si veo a alguien jugar a la jenka, o si paso por el mosset, o por la academia FIR, o por la confitería de blasco ibañez, o por el bierwinkel, o por el Morgan, o por la fnac... y me acuerdo de todos vosotros. O cuando recuerdo noches o fragmentos de noches en Picadilly, Miniclub, Excuseme, Murray o en algún antro de Polo y Pirolo. O cuando paso por Barón de Cárcer, o por la calle de la paz, o por el turmix ahora convertido en un local de adolescentes, o por cualquier calle del carmen. O si veo en las noticias sobre o Gales o Burgos o Xirivella, o Barcelona, o Madrid, o Murcia, o Rumania, o Chicago, o Bilbao, o Galicia, o Viena, o Zaragoza, o Asturias, o Alemania, o Nueva Zelanda, u Holanda o Bruselas, o Italia, o Suiza o casi de cualquier parte... os recuerdo a todos. Si paso por el burlón aun oigo el sonido que nunca olvidaré... y me acuerdo de ti y de ti y de lo que os quiero. Y de ti también, porque ni estando a 600km faltaste y de ti que nunca te fuiste. Y paro... porque me obligo a hacerlo.

Finalmente: Gracias a mi familia, y a Amparo en especial, por confiar en mi siempre y por compartir conmigo esa extraña clarividencia que posee. Gracias a mi abuelo porque sin su recuerdo nada tendría sentido. Gracias Celia por asustar a mis monstruos y por sorprenderme cada día. Y hablando de sorprender cada día... Gracias JP por tu ejemplo y valentía.

Contents

Introduction	1
1 The Standard Model of Particle Physics	5
1.1 The structure of the Standard Model	5
1.2 The gauge sector: Local $SU_C(3) \otimes SU_L(2) \otimes U_Y$ gauge invariance . . .	7
1.2.1 The theory of the electroweak interactions	8
1.2.2 The theory of the strong interactions	9
1.3 Spontaneous Symmetry Breaking	10
2 Quantum Chromodynamics for hadron colliders	15
2.1 Theoretical description of hadronic collisions:	
QCD improved parton model	16
2.1.1 Higher order calculations in pQCD: UV and IR divergences . . .	16
2.1.1.1 Ultraviolet divergences and renormalization procedure	16
2.1.1.2 Infrared divergences and infrared safe observables . .	20
2.1.2 Factorization and parton distribution functions	22
2.2 Monte Carlo Tools	24
2.2.1 Introduction to the Parton Shower algorithms in Standard Monte Carlo programs	25
2.2.2 Next-to-Leading order and Parton Showering	29
2.3 Jet physics	30
3 Top-quark physics and a new method to measure its mass	35
3.1 The top quark	35
3.1.1 The special role of the top quark in the EWSB sector and in Beyond Standard Model theories	38
3.2 Current top-quark mass measurements	43
3.2.1 Direct measurements	43
3.2.2 Top-quark mass extraction from inclusive cross section measurements	43
3.3 Precise top-quark mass determination methods	45
3.4 Top-quark mass measurement from jet rates	46

3.4.1	Next-to-leading order calculations of $t\bar{t}$ +1-jet topologies	47
3.4.2	Theoretical definition and study of the \mathcal{R} observable	53
3.5	Conclusions	57
4	The ATLAS detector at the Large Hadron Collider (LHC)	59
4.1	Large Hadron Collider	59
4.1.1	The LHC experiments	61
4.1.2	The Worldwide LHC Computing Grid (WLCG)	63
4.2	The ATLAS detector	63
4.2.1	The Inner Detector	65
4.2.2	The Calorimetry System	66
4.2.3	The Muon System	68
4.2.4	The Trigger System	69
5	Reconstruction of $t\bar{t}$ +1-jet events using the ATLAS detector	71
5.1	Experimental signature for $t\bar{t}$ +1-jet events	71
5.2	Object definition and event selection	72
5.2.1	Object definitions	72
5.2.2	Basic event selection	73
5.3	Data sample and event selection	74
5.3.1	Monte Carlo Simulation	75
5.3.2	Multijet events	76
5.4	Event yields after the basic selection	76
5.5	Reconstruction of the $t\bar{t}$ +1-jet events	79
5.5.1	Identification of the W bosons candidates	79
5.5.2	Reconstruction of the $t\bar{t}$ +1-jet system	80
5.5.3	Quality of the reconstructed events	81
5.6	Reconstructed $t\bar{t}$ +1-jet events	82
6	Experimental determination of the top-quark pole mass.	87
6.1	The $t\bar{t}$ +1-jet system at parton level.	87
6.2	Unfolding procedure	88
6.3	Fit to $t\bar{t}$ + 1-jet @NLO+PS	91
6.4	Independence of the unfolding procedure with the Monte Carlo mass.	92
6.5	Additional cross checks for the unfolding procedure.	97
6.6	Statistic and systematic uncertainties	97
6.6.1	Theoretical uncertainties	98
6.6.2	Detector modeling	99
6.6.3	Signal modeling	103
6.6.4	Background modeling	106
6.7	Results and discussions	107
7	Prospects for future analyses	113

8 Conclusions	115
Resumen en español	121
El quark top y su masa	122
Un nuevo método para medir la masa polo del quark top	123
Resultados y conclusiones	125
Appendices	131
A Unfolding correction based on the shape of the \mathcal{R} distribution.	131
B Matrix inversion and regularization algorithm	133
B.1 The regularized covariance matrix	133
B.2 One-step unfolding versus two-step unfolding	133
C Parametrization of the $t\bar{t}$ +1-jet on m_t^{pole} at NLO+PS accuracy	139
D Estimation of the Initial and final-state radiation (ISR/FSR) uncertainty.	141
E Breakdown of the uncertainties evaluated for the different $t\bar{t}$ decay channels.	143
F Validation of POWHEG samples	147
References	151

Introduction

The Standard Model (SM) of particle physics is the theoretical framework that describes the interactions and dynamics of the subatomic world. The SM assumes that matter is made of elementary, point-like and structureless particles characterised by their quantum numbers. These elementary particles are classified in two types: fermions and bosons. The bosons can be of two types: the ones that are responsible of the fundamental interactions (electroweak or strong) and the Higgs boson which has been recently discovered [1, 2]. The Higgs boson appears in the SM as the physical representation of the Brout-Englert-Higgs field which permeates the space and is responsible for the generation of the masses of the fundamental particles. The fermions are also divided in two types: the leptons and the quarks. The leptons, electrons and neutrinos, only feel the electroweak and weak interaction respectively. The quarks are the fermions that feel the electroweak interaction and the strong interaction. The latter particles are not found in nature as free particles since they are bound into composite particles, called hadrons, through the strong interaction.

Since quarks do not exist as free particles, quark masses are not observables in contrast with the masses of fermions which can be observed directly in nature. Quark masses are not observables and have to be extracted from the measurement of hadronic observables that depend on them since they are interpreted as effective couplings of the underlying theory (the SM in this case). This is a similar situation as the case of the determination of the strong interaction coupling constant, α_s , which is not measured directly but inferred through the measurement of cross sections, branching ratios, event shapes distributions, etc.,.

Due to the large coupling of the top quark with the Higgs boson, the top quark plays a special role in the Electroweak sector of the SM. Moreover, many models beyond the Standard Model predict deviations in the top-quark physics sector. Top-quark mass measurements with high precision are crucial to test the validity of the SM.

Since the discovery of the top quark in 1995 in $p\bar{p}$ collisions at the Tevatron in the CDF and D0 experiments [3, 4], high precision measurements of its properties have been performed. At present, the CDF and D0 experiments are no longer operative. Another accelerator, the Large Hadron Collider (LHC), is operative at present. It has been producing pp collisions at 7 TeV and 8 TeV during 2011 and 2012 respectively and it will work at ~ 13 TeV in the near future (2015). The ATLAS (A Toroidal Large Apparatus) and CMS (Compact Muon Solenoid) are the general purpose ex-

periments placed at the LHC that are currently detecting and studying top quarks produced through the pp interactions.

The most commonly used technique to determine the top quark mass consists in direct measurements of the invariant mass of its decay products. The interpretation of this measurement within a renormalization scheme (the pole mass) has an unknown uncertainty which might be of the order ~ 1 GeV [5, 6]. The achieved experimental precision obtained so far is however better than 1 GeV ($\sim 0.5\%$) (see, for example, Ref. [7]). Therefore, alternative methods with similar experimental precision and in which the mass is theoretically unambiguously defined become very relevant and important. The most well known *alternative* top-quark mass measurement is based on its extraction from inclusive top-quark pair cross section measurements. The mass extracted using this method is well defined in terms of the mass couplings that appear in the SM Lagrangian, but the uncertainties are larger than for the direct measurement since the sensitivity of the cross section on the top quark mass is limited.

The first part of this PhD describes the definition and study of a new method to determine the top-quark mass using a well defined theoretical framework. These studies are based on top-quark pair production in association with a hard jet using next-to-leading order QCD calculations [8, 9, 10]. More precisely, this new method employs the normalized differential $t\bar{t} + 1$ -jet cross section dependence on the top-quark mass to infer it. The method is specially sensitive to the top-quark mass in regions of the phase space where the invariant mass of the $t\bar{t} + 1$ -jet system is small. Moreover, due to the normalization of the measured quantity, some theoretical and experimental uncertainties are reduced due to cancellations between numerator and denominator. The defined method shares the rigorous interpretation of the mass with the top-quark mass extraction from the inclusive top-quark pair production cross section. This work has been performed by a close collaboration between experimental (from Valencia - IFIC) and theoretical (from Berlin - DESY and Humboldt-Universität) physicists. The results of this work have been published in the European Physics Journal in March 2013 [11].

The second part of this thesis reports the first experimental top-quark pole mass determination using the proposed method using data collected by the ATLAS collaboration during 2011 in pp collisions at 7 TeV. To this end, $t\bar{t} + 1$ -jet events are identified and the differential cross section is measured. A complete study of the systematic and statistic uncertainties associated to the top-quark mass determination has been performed. Two different types of systematic uncertainties have been carefully estimated: the experimental systematic uncertainties (associated to the signal, background, detector performance modeling) and the theoretical systematic uncertainties (due to the choice of the parton distribution function that describes the internal structure of the proton and the ones due to non calculated higher order terms in the $t\bar{t} + 1$ -jet cross section). The results were presented by the ATLAS collaboration in the Top2014 conference [12] and a paper to be submitted to the Journal of High Energy Physics (JHEP) is being prepared.

This thesis is organized as follows. The formalism and the matter content of the Standard Model is introduced in Chapter 1. In Chapter 2, a short review of the most important aspects related to the modeling of the interactions between hadrons at high

energies are presented. The LHC accelerator and the ATLAS detector are presented in Chapter 4. Top-quark physics is introduced in Chapter 3. In this chapter, the importance of a precise top-quark mass measurement is discussed in detail and the new method is presented and its theoretical properties largely discussed. The reconstruction of $t\bar{t} + 1$ -jet events with the ATLAS detector is shown in Chapter 5. In Chapter 6, the top-quark mass is extracted from the measured differential cross section. Finally, Chapters 7 and 8 contain the prospects for future improvements of this analysis and the conclusions, respectively.

1

The Standard Model of Particle Physics

According to present knowledge, matter is composed by fundamental bricks called elementary particles, which are supposed to be indivisible objects. Their classification and the way that they interact between them is, nowadays, understood within the theoretical framework of the Standard Model of Particle Physics.

The chapter starts in Section 1.1 with a short description of the Standard Model (SM) theory and of the classification of particles and interactions. In Section 1.2 the gauge formalism of the SM theory is introduced very briefly. In Section 1.3, the Brout-Englert-Higgs mechanism by which the elementary particles of the SM acquire their masses is covered.

This chapter presents a short summary of the most important concepts of the Standard Model related to the work presented in this thesis. A detailed review of them is omitted since it is beyond the scope of this work. To avoid the repetition of references in the text, some academic sources consulted during the writing of this part are given in references [13, 14, 15].

1.1 The structure of the Standard Model

There are four fundamental interactions among elementary particles: the electromagnetic interactions, which are described by Quantum Electro-Dynamics (QED), the weak interaction, the strong interaction which is described by Quantum Chromodynamics (QCD) and, finally, the gravitational interactions. The Glashow-Weinberg-Salam model [16, 17, 18] merges the QED theory with the theory that describes the weak interactions in the so-called Electroweak Theory (EW). The combination of QCD with Electroweak theory forms the Standard Model of the particle interactions. Gravity is not included in the SM and its implementation represents one of the majors goals in the field of particle physics.

Thus, the SM is based on the fact that the elementary particles are the building blocks of nature. These particles are structureless objects defined by a number of intrinsic properties: mass, spin and their quantum numbers that describe the SM dynamics. The elementary particles are classified in two types according to the SM: fermions (spin $\frac{1}{2}$, described by the Fermi-Dirac statistics) and bosons (integer spin, described by the Bose-Einstein statistics). More formally, the Standard Model is a gauge theory which describes the interactions between fermions and bosons. These interactions are mediated by the interaction or gauge bosons. These bosons arise from the requirement of the local gauge invariance of the fermion fields. The interaction bosons are manifestations of the symmetry group responsible for each interaction.

The SM is formulated as a quantum field theory in which the fermions and bosons are represented by quantum fields. The whole information of these fields and their interactions is encoded in the so-called SM Lagrangian, \mathcal{L} , which is a scalar function of the quantum fields. Similar to what it is done in classical mechanics, the equations of movement are derived assuming that the action is stationary: $\delta \int \mathcal{L} dt = 0$. The interaction between particles, and its physical representation as mediator bosons, arise from the requirement of the local gauge invariance of the fermion fields. Gauge invariance means that the action remains invariant under transformations of the fields in the space-time. These symmetric transformations can be global (for all the space) or local.

The SM fermions.

Fermions are classified in two different groups: leptons and quarks.

Leptons can also be classified in two groups: the ones that carry electrical charge and the others. The electron (e), muon (μ) and tau (τ) have electrical charge equal to $q = -1$. The other group of leptons does not have electrical charge but does carry weak isospin charge: the neutrinos (ν). The electrically charged leptons and the neutrinos are related to each other by their weak isospin charge. Following this description, the leptons are separated in three generations (three weak isospin doublets): 1st generation (e, ν_e), 2nd generation (μ, ν_μ) and 3rd generation (τ, ν_τ).

There are six types (or flavors) of quarks: up, down, strange, charm, bottom and top (u, d, s, c, b, t). Quarks are not found in nature as free particles since they are confined through strong interaction into composite particles called hadrons. Ordinary and stable matter is only composed by the up and down flavors, which are the building blocks that compose the protons and neutrons (both of them are also hadrons). The quarks are classified also in three families which separates them into doublets of weak isospin: 1st generation (u, d), 2nd generation (c, s) and 3rd generation (b, t).

Since the second and third families are unstable the heaviest quarks (strange, charm, bottom and top) the μ, τ and their neutrinos can only be found in nature when high energy interactions are produced (accelerator experiments, processes involving high energy cosmic radiation...).

Classification of all SM fermions and their properties are summarized in the Fig. 1.1.

The SM bosons.

The photon (γ) mediates the interactions between electrically charged particles (QED interactions). The W^\pm and Z bosons mediate the weak force. Finally, eight gluons (g) mediate the strong interaction.

The weak interaction mediator bosons and the fermions in the SM acquire mass through the Brout-Englert-Higgs (BEH) [19, 20, 21, 22, 23, 24] mechanism which causes a Spontaneous Electroweak Symmetry Breaking (EWSB) that keeps the invariance of the Lagrangian under the symmetry group, while the ground state of the system (the vacuum state) no longer exhibits the invariance. The Higgs boson is the physical state associated to the BEH field.

The general properties of the SM bosons are also found in Fig. 1.1.

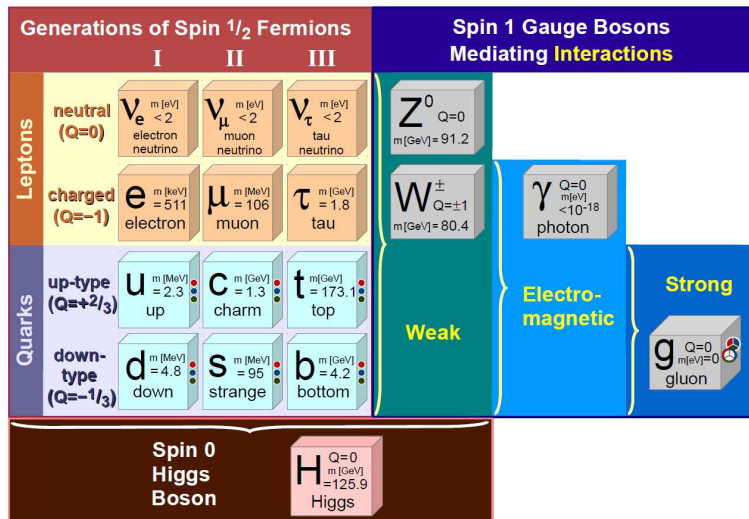


Figure 1.1: Fundamental particles (and their properties) of the Standard Model. The three firsts columns show the three different generations of fermions. The fourth column is filled by the representation of the gauge bosons related to the weak interaction. In the fifth column the photon, responsible of the electromagnetic interactions is shown. In the sixth, the gluon is presented. Finally, in the bottom part, the Higgs boson, which appears in the electroweak symmetry breaking processes, is listed. The listed properties are their mass (m), electrical charge (Q) and spin (S) [25]. The possible color states for the quarks and gluons are represented with color dots. The curly brackets indicate the participating particles for the interactions and the couplings to the Higgs boson.

1.2 The gauge sector: Local $SU_C(3) \otimes SU_L(2) \otimes U_Y$ gauge invariance

The SM theoretical formulation is based on the gauge symmetry group $SU_C(3) \otimes SU_L(2) \otimes U_Y$ of unitary gauge transformations. The strong interactions are described

by the first group, $SU_C(3)$ (the 3×3 unitary matrices with unit determinant group). The gauge theory of the electroweak interactions appears in the SM represented by the $SU_L(2) \otimes U_Y$. The first (the 2×2 unitary matrices group) describes the weak interactions, the second (the group of complex numbers with unit modulus) the weak hypercharge.

1.2.1 The theory of the electroweak interactions

The electromagnetic and weak interactions are described by the $SU_L(2) \otimes U_Y$ gauge symmetry group. The $SU_L(2)$ only affects the left-handed fermions f_L ¹ and is defined in the space of the weak isospin charge, T (its generators are; $T_i = \sigma_i/2$ where $i = 1, 2, 3$ and σ_i are the Pauli matrices). U_Y is defined in the space of the weak hypercharge, Y , which is constructed from the electromagnetic charge and the third component of the weak isospin.

The fermion fields, f , are divided in left-handed or right-handed, f_L, f_R :

$$\begin{bmatrix} \nu_l & q_u \\ l^- & q_d \end{bmatrix} \equiv \begin{pmatrix} \nu_l \\ l^- \end{pmatrix}_L, \begin{pmatrix} q_u \\ q_d \end{pmatrix}_L, l_R^-, (q_u)_R, (q_d)_R \quad (1.1)$$

where ν refers to the neutrino, l to the lepton and q to the quark fields.

The SM electroweak Lagrangian is:

$$\begin{aligned} \mathcal{L} &= \sum_{f=l,q} \bar{f} i \gamma^\mu D_\mu f \\ &- \frac{1}{4} W_{\mu\nu}^i W_i^{\mu\nu} - \frac{1}{4} B_{\mu\nu} B^{\mu\nu} \\ &+ \mathcal{L}_{GF} + \mathcal{L}_{FP} \end{aligned} \quad (1.2)$$

The first line represent the fermion term and the fermion-gauge bosons interaction terms of the Lagrangian where D_μ is the covariant derivative,

$$D_\mu = \left(\partial_\mu - ig \vec{T} \cdot \vec{W}_\mu - ig' \frac{Y}{2} B_\mu \right) \quad (1.3)$$

and \vec{W}_μ, B_μ are the gauge boson fields associated to the W^\pm, Z and γ bosons. The second line summarizes the gauge boson kinetic self-interaction terms, given by the field tensors:

$$\begin{aligned} W_{\mu\nu}^i &= \partial_\mu W_\nu^i - \partial_\nu W_\mu^i + g \epsilon^{ijk} W_\mu^j W_\nu^k, \\ B_{\mu\nu} &= \partial_\mu B_\nu - \partial_\nu B_\mu \end{aligned} \quad (1.4)$$

with ϵ^{ijk} being the Levi-Civita tensor. The associated physical gauge bosons W_μ^\pm, Z_μ

¹The left-handed and right-handed neutrinos are defined using the chirality operator $\gamma_5 = i\gamma_0\gamma_1\gamma_2\gamma_3$ as $f_L = \frac{1}{2}(1 - \gamma_5)f; f_R = \frac{1}{2}(1 + \gamma_5)f$

and A_μ are obtained from the electroweak eigenstates by,

$$\begin{aligned} W_\mu^\pm &= \frac{1}{\sqrt{2}}(W_\mu^1 \mp W_\mu^2), \\ Z_\mu &= \cos \theta_W W_\mu^3 - \sin \theta_W B_\mu, \\ A_\mu &= \sin \theta_W W_\mu^3 + \cos \theta_W B_\mu, \end{aligned} \quad (1.5)$$

where θ_W is the Weinberg angle and defines the rotation in the neutral sector. Identifying the interaction terms of A_μ with those of QED, we get the relation between the various couplings:

$$\begin{aligned} g &= \frac{e}{\sin \theta_W}, \quad g' = \frac{e}{\cos \theta_W} \\ Q &= T_3 + \frac{Y}{2} \end{aligned} \quad (1.6)$$

Finally, the last line in Eq. (1.2) shows the gauge fixing and Faddeev-Popov terms that are needed to quantize the gauge theory (which discussion is well far from the scope of this document).

1.2.2 The theory of the strong interactions

Strong interactions are described by a $SU(3)$ color-symmetry group (non abelian). The color is treated as the charge of the strong interaction. The QCD Lagrangian is:

$$\begin{aligned} \mathcal{L} &= \sum_f \bar{q}_f^\alpha (i\gamma^\mu D_\mu) q_f^\alpha \\ &+ g_s G_a^\mu \sum_f \bar{q}_f^\alpha \gamma_\mu \left(\frac{\lambda^a}{2} \right)_{\alpha\beta} q_f^\beta \\ &- \frac{1}{4} (\partial^\mu G_a^\nu - \partial^\nu G_a^\mu) (\partial_\mu G_\nu^a - \partial_\nu G_\mu^a) \\ &+ \frac{g_s}{2} f^{abc} (\partial^\mu G_a^\nu - \partial^\nu G_a^\mu) G_\mu^b G_\nu^c - \frac{g_s^2}{4} f^{abc} f_{ade} G_b^\mu G_c^\nu G_\mu^d G_\nu^e \end{aligned} \quad (1.7)$$

where λ^a ($a = 1, \dots, 8$) are the generators of the fundamental representation of $SU_C(3)$, G_a^μ are the gauge boson fields associated to the gluons, D_μ is the covariant derivative $D^\mu \equiv \partial^\mu - ig_s G^\mu(x) = \partial^\mu - ig_s \frac{\lambda_a}{2} G_a^\mu(x)$ and f^{abc} are the structure constants¹.

All the interactions are given in terms of the single universal coupling g_s . The strong coupling is then defined as $\alpha_s = \frac{g_s^2}{4\pi}$ in analogy with the electromagnetic con-

¹The matrices generators for $SU_C(3)$ λ^a , are traceless and satisfy: $[\lambda^a, \lambda^b] = 2if^{abc}\lambda^c$ with f^{abc} the $SU(3)_C$ structure constants which are real and totally antisymmetric:

$f_{123} = 1, f_{458} = f_{678} = \sqrt{3}/2, f_{147} = f_{165} = f_{246} = f_{345} = f_{376} = f_{257} = 1/2$

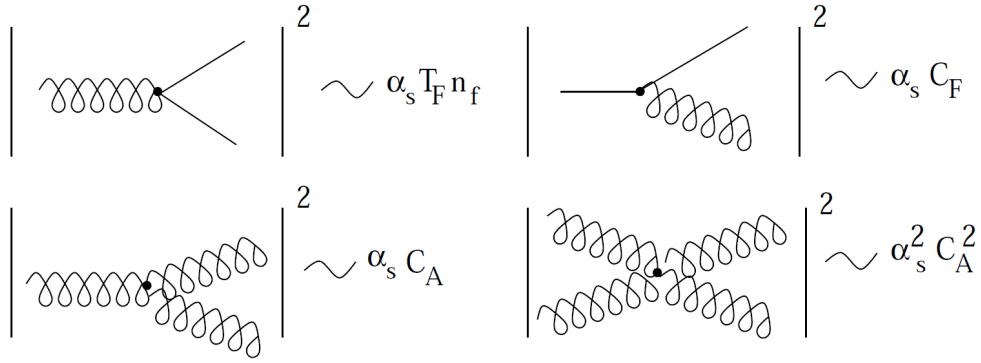


Figure 1.2: Relation between the $SU(N)$ group constants and the splitting functions

stant. The first and the second line in Eq. (1.7) represent the kinematic term of the quarks and the interaction term between quarks and gluons, respectively. The third line represents the free kinematic term of the gluon propagator and, in the last line, the gluon self interactions are shown.

For $SU(N)$, defining the color matrices as $T_a = \lambda_a/2$, the following relations can be obtained:

$$\begin{aligned}
 T_F &\equiv \delta_{ab} \text{Tr}(T^a T^b) = \frac{1}{2} \\
 C_F &\equiv \delta^{ac} \sum_A T_{ab}^A T_{bc}^A = \frac{N^2 - 1}{2N} \\
 C_A &\equiv \delta_{CF} \sum_{A,B} f^{ABC} f^{ABD} = N
 \end{aligned} \tag{1.8}$$

These quantities, characteristic of the gauge group chosen to construct the Lagrangian, are directly related to the strength of the different couplings between gluons and quarks. They are schematically shown in Figure 1.2 for $SU_C(3)$. This kind of diagrams used to represent the interactions are called Feynman diagrams: they are pictorial representation of the mathematical expressions that describe the dynamics of the particles within quantum field theories.

1.3 Spontaneous Symmetry Breaking

The electroweak and QCD Lagrangians only contain massless fields. This happens for the bosons and for the fermions. Adding mass terms will introduce a breaking of the gauge symmetry. The way to deal with this feature in the SM (since the weak interaction bosons (W^\pm and Z) and the fermions are known experimentally to be massive) is the so-called Brout-Englert-Higgs Mechanism. The basic idea consists of introducing a new term to the Lagrangian in such a way that it preserves the gauge

symmetry but the vacuum state of the system does not. Actually, it preserves the gauge symmetry in the $U_Y(1)$ group. This new Lagrangian will have a degenerate set of states of minimal energy. When one of these states is arbitrarily selected to be the ground state, the symmetry is spontaneously broken. The BEH mechanism introduces two new pieces to the SM Lagrangian.

ElectroWeak boson masses and Spontaneous Symmetry Breaking: the BEH mechanism I

The first is associated to the generation of the mediator weak bosons mass, the \mathcal{L}_{SSB} :

$$\begin{aligned}\mathcal{L}_{SSB} &= (D_\mu\Phi)^\dagger(D^\mu\Phi) - V(\Phi) \\ V(\Phi) &= -\mu^2\Phi\Phi^\dagger + \lambda(\Phi^\dagger\Phi)^2, \lambda > 0 \text{ and } \mu^2 < 0\end{aligned}\quad (1.9)$$

constructed adding a new system Φ which is an $SU(2)_L$ doublet of complex scalar fields with hypercharge $Y = 1$

$$\Phi = \begin{pmatrix} \phi^+ \\ \phi^0 \end{pmatrix}\quad (1.10)$$

This four components doublet of complex scalar fields has an infinite set of degenerate states with minimum energy, $|\Phi|^2 = \Phi^\dagger\Phi = -\frac{\mu^2}{\lambda} \equiv \frac{v}{2}$, being v the vacuum expectation value. All these states keep the $U(1)$ symmetry but not the $SU(2) \otimes U(1)$ symmetry. Therefore, when, according to the BEH mechanism, a particular vacuum is chosen, the symmetry is spontaneously broken.

As a consequence, three massless Goldstone bosons are generated, which are absorbed to give mass to the weak bosons W^\pm and Z . The remaining fourth component of the complex doublet Φ manifest itself in the scalar particle called Higgs boson. The acquired masses for the weak and Higgs bosons are:

$$\begin{aligned}M_W &= \frac{gv}{2} \\ M_Z &= \frac{v\sqrt{g^2 + g'^2}}{2} = \frac{M_Z}{\cos\theta_W} \\ M_H &= v\sqrt{2\lambda}\end{aligned}\quad (1.11)$$

The value of vacuum expectation value can be estimated using the $G_F/\sqrt{2} = g^2/(8M_W^2)$ relation obtained from the effective V-A theory:

$$v = \frac{1}{\sqrt{G_F\sqrt{2}}} \simeq 246 \text{ GeV},\quad (1.12)$$

where G_F is the Fermi constant. Using this estimated value for v , the known value of

fine structure constant and the estimation of the Weinberg angles (for example from muon and neutrino scattering), the mass of the W^\pm and Z boson can be estimated at first order:

$$\begin{aligned} M_W &= \sqrt{\left(\frac{\pi\alpha}{G_F\sqrt{2}}\right)} \frac{1}{\sin\theta_w} \simeq 78 \text{ GeV} \\ M_Z &= \frac{M_W}{\cos\theta_w} \simeq 89 \text{ GeV} \end{aligned} \quad (1.13)$$

Introducing calculations at high accuracy gives better agreement with experimentally measured values [25].

The mass of the Higgs bosons is determined by the λ coefficient which is unknown.

Fermion masses and Spontaneous Symmetry Breaking:

the BEH mechanism II

The second term introduced to the EW Lagrangian by the BEH mechanism is the so-called Yukawa Lagrangian. It is a gauge invariant fermion-scalar coupling:

$$\mathcal{L}_{YW} = \lambda_e \bar{l}_L \Phi e_R + \lambda_u \bar{q}_L \tilde{\Phi} u_R + \lambda_d \bar{q}_L \Phi d_R + \text{h.c} \quad (1.14)$$

where,

$$l_L = \begin{pmatrix} \nu_L \\ e_L \end{pmatrix}; q_L = \begin{pmatrix} u_L \\ d_L \end{pmatrix}; \tilde{\Phi} = i\sigma_2 \Phi^* = \begin{pmatrix} \phi_0^* \\ -\phi^- \end{pmatrix} \quad (1.15)$$

Similarly to previous case, expanding the Lagrangian around the vacuum and rotating the weak eigenstates to the mass eigenstates, a new set of mass terms is obtained:

$$\mathcal{L}_{YW} = - \left(\lambda_e \frac{v}{\sqrt{2}} \right) \bar{e}'_L e'_R - \left(\lambda_u \frac{v}{\sqrt{2}} \right) \bar{u}'_L u'_R - \left(\lambda_d \frac{v}{\sqrt{2}} \right) \bar{d}'_L d'_R + \dots \quad (1.16)$$

that corresponds to the mass terms of the massive fermions,

$$m_e = \lambda_e \frac{v}{\sqrt{2}}; m_u = \lambda_u \frac{v}{\sqrt{2}}; m_d = \lambda_d \frac{v}{\sqrt{2}}; \dots \quad (1.17)$$

being λ_f the Yukawa coupling of the fermion f with the Higgs field.

If the \mathcal{L}_{SSB} and \mathcal{L}_{YW} are rewritten in terms of the physical scalar fields, they can be understood as the free and interaction terms of the Higgs field,

$$\mathcal{L}_{SSB} + \mathcal{L}_{YW} \rightarrow \mathcal{L}_H^{free} + \mathcal{L}_H^{int} + \dots \quad (1.18)$$

where,

$$\mathcal{L}_H^{free} = \frac{1}{2} \partial_\mu H \partial^\mu H - \frac{1}{2} M_H^2 H^2 \quad (1.19)$$

is the Higgs free Lagrangian and,

$$\begin{aligned} \mathcal{L}_H^{int} = & -\frac{gM_H^2}{4M_W} H^3 - \frac{g^2 M_H^2}{32M_W^2} H^4 \\ & - \frac{m_f g}{2M_W} \bar{f} H f \\ & + M_W^2 W_\mu^+ W^{\mu-} \left(1 + \frac{g}{M_W} H + \frac{g^2}{4M_W^2} H^2 \right) \\ & + \frac{M_Z^2 Z_\mu Z^\mu}{2} \left(1 + \frac{g}{M_Z \cos \theta_w} H + \frac{g^2}{4M_Z^2 \cos^2 \theta_w} H^2 \right) \end{aligned} \quad (1.20)$$

where the interaction terms which are proportional to the gauge couplings and to the particle masses (including the Higgs mass). The first row in Eq. (1.20) shows the Higgs self-couplings. The couplings with the fermions, the W^\pm and the Z are shown in the second, third and fourth rows respectively.

The Brout-Englert-Higgs mechanism explains why particles acquire masses through their interaction with the Higgs field, but the value of their masses is undetermined by the SM.

Recently, in the Large Hadron Collider experiments (LHC), a new state compatible with the properties of the Higgs boson has been discovered [1, 2] with a measured mass of $M_H = 125.03$ GeV [26, 27]. With this mass value, the Higgs boson is the second heaviest elementary particle discovered so far, after the top quark, which measured mass is $m_t \simeq 173$ GeV [25]. In Chapter 3 the relation between the mass values of these two particles (and the electroweak bosons) and their role in the EWSB sector is discussed in more detail.

2

Quantum Chromodynamics for hadron colliders

The QCD Lagrangian that explains the strong interactions between quarks and gluons has been presented in the previous chapter. This Lagrangian presents two features that are not present in QED or the Weak Lagrangians: confinement and asymptotic freedom. The confinement is the property which makes quarks and gluons to be bounded into hadrons. The asymptotic freedom is the property of the strong interaction which explains that at high energies (i.e. short distances) the constituents of hadrons behave as quasi-free particles.

Understanding QCD is crucial to study the interactions that occur when two hadrons collide as it happens in the Large Hadron Collider (presented in Chapter 4) where pp collisions at high energy are produced and measured. These interactions occur between the constituent quarks and gluons (called partons) of the incident hadrons. To understand the dynamics of the interactions, theoretical calculations of the partonic cross sections must be performed with high precision. Moreover, a good knowledge of the internal structure of the incident hadrons is needed to obtain good theoretical predictions. The theoretical technique used to make predictions for high energy interactions between hadrons is called perturbative QCD (pQCD) which is presented in Section 2.1. In this section, concepts like the factorization of the cross section, renormalization of couplings (α_s , masses of the particles ...) and fields, infra-red safe observables, parton distribution functions, etc, are discussed. In Section 2.2, the Monte Carlo tools that are used by high-energy physicists to predict and to simulate these interactions in a framework in which they could be compared with experimental data are presented. Finally, in Section 2.3, the notion of jets is introduced.

More detailed reviews on the presented concepts can be found in Refs. [14, 28, 29, 30, 31] which have been used during the writing of this chapter.

2.1 Theoretical description of hadronic collisions:

QCD improved parton model

High-energy interactions between colliding hadrons occur between their constituents: quarks and gluons called constituent partons. The interactions are described by the so called QCD improved parton model. In this model, the $H_1 H_2 \rightarrow X$ cross section calculation for two hadrons, H_1 and H_2 , colliding at high energies and producing X as final state is:

$$d\sigma = \sum_{a,b} \int dx_1 dx_2 f_{a/H_1}(x_1, \mu_F) f_{b/H_2}(x_2, \mu_F) d\hat{\sigma}_{ab \rightarrow X}(\hat{s}, \mu_F) \quad (2.1)$$

where $f_{j/H}$ represents the parton distribution function (PDF) which qualitatively describes the probability of finding a parton j inside the hadron $H_{1,2}$ carrying a momentum fraction between x and $x + dx$. The factorized partonic cross section from matrix elements is represented by $d\hat{\sigma}_{ab \rightarrow X}$ with $\hat{s} = x_1 x_2 \cdot s_{H_1 H_2}$ the squared center of mass energy of the interaction between the incident partons. Since the coupling constant, α_s is small at high-energies, the partonic cross section can be calculated as a perturbative expansion in terms of α_s

The partonic cross section is model and process dependent. The PDF depend only on the incoming hadrons and are process independent. To calculate the cross section, both contributions are convoluted, by direct application of the factorization theorem [32] at certain scale μ_F known as factorization scale.

A more detailed description of the perturbative QCD calculations and the factorization and parton distribution functions can be found in the following sub-sections.

2.1.1 Higher order calculations in pQCD: UV and IR divergences

The parton level cross section $d\hat{\sigma}_{ab \rightarrow X}(\hat{s}, \mu_F, \mu_R)$ is calculated perturbatively as an expansion in α_s . Schematically:

$$\hat{\sigma} = \sigma_{Born} \left(1 + \frac{\alpha_s}{2\pi} c_1 + \left(\frac{\alpha_s}{2\pi} \right)^2 c_2 + \dots \right) \quad (2.2)$$

The leading-order (LO) approximation corresponds to the Born calculation of the tree level diagrams. For example, Fig. 2.1 shows the LO partonic contributions to the $pp \rightarrow t\bar{t} + X$ cross section. Next-to-leading-order (NLO) corrections offer a better description of the final state including extra radiation corrections, the so called real corrections. This additional radiation also opens the possibility of having additional initial state partonic channels.

2.1.1.1 Ultraviolet divergences and renormalization procedure

Gauge Quantum Field Theories are renormalizable [33], i.e. all the ultra violet (UV) divergences can be reabsorbed through the redefinition of a finite numbers of

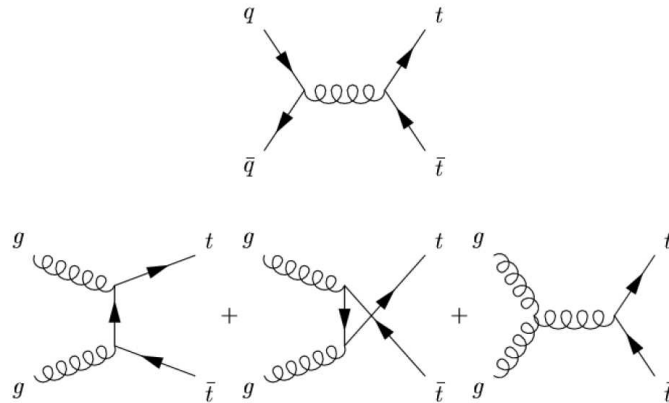


Figure 2.1: Partonic leading-order contributions for the $pp \rightarrow t\bar{t}$ cross section

fields and couplings of the theory. When computing NLO calculations, the application of the Feynman rules lead to the so called loop integrals responsible for the UV divergences. This kind of integrals are logarithmically divergent due to the behavior at high energy. Two examples are shown in Fig. 2.2: the gluon self-energy in the left and the quark self-energy in the right.

The usual strategy to deal with these divergences consist in:

- **Regularization:** localize and identify the divergence.
- **Renormalization:** absorb the divergent terms in a redefinition of the fields and couplings.

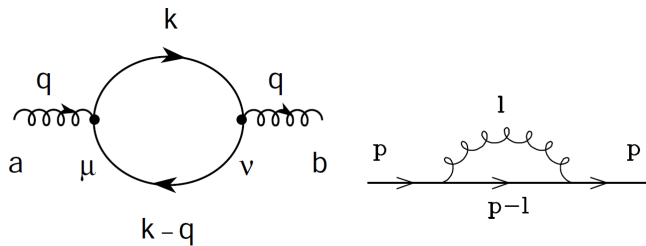


Figure 2.2: Self-energy diagrams example. The first diagram corresponds to the gluon self-energy and the second to the quark self-energy. The four momenta of the gluon and quark, respectively, are represented by q and p .

The most common procedure to regularize the integrals is the dimensional regularization which preserves the gauge symmetry of QCD. In this method the 4-dimensions integrals are converted in d -dimensions integrals with $d = 4 + 2\epsilon$ and $\epsilon \neq 0$.

A renormalization scale μ_R is introduced in order to keep the coupling constant dimensionless in d -dimensions. The divergences will appear as a function of $1/\epsilon$. They are isolated and separated to be reabsorbed by the coupling constants, but this

separation procedure is ambiguous, as far as the definition of the finite contribution can be split in different ways.

Therefore, a renormalization scheme to specify how the coupling constants will absorb the divergences is needed. One scheme is the $\overline{\text{MS}}$ scheme (Minimal subtraction) which only subtracts the divergent $1/\varepsilon$ term. The most used scheme is the $\overline{\text{MS}}$ scheme (Modified Minimal subtraction) in which $1/\hat{\varepsilon}$ is subtracted, with $1/\hat{\varepsilon} \equiv 1/\varepsilon + \gamma_E - \ln 4\pi$ ¹. After having chosen the renormalization scheme, the couplings absorb the divergences and the dependence with the scale μ_R .

Renormalization group equation and the running of the couplings

Two degrees of freedom have been introduced during the application of the renormalization procedure: the choice of the renormalization scheme and the introduction of a new scale μ_R . However, physical quantities can not depend on any of these arbitrary choices. This independence leads to the renormalization group equation for any observable $R(Q^2/\mu_R^2, \alpha_s(\mu_R), m(\mu_R)/Q)$:

$$\begin{aligned} 0 &= \mu_R^2 \frac{d}{d\mu_R^2} R(Q^2/\mu_R^2, \alpha_s(\mu_R), m(\mu_R)/Q) = \\ &= \left(\mu_R^2 \frac{\partial}{\partial \mu_R^2} + \beta(\alpha_s) \frac{\partial}{\partial \alpha_s} - \gamma(\alpha_s) m \frac{\partial}{\partial m} \right) R \end{aligned} \quad (2.3)$$

which defines two renormalization group coefficients: the β function and the anomalous mass dimension γ . The first is

$$\beta(\alpha_s) = \mu_R^2 \frac{\partial \alpha_s}{\partial \mu_R^2}, \quad \beta(\alpha_s) = -(\beta_0 \alpha_s^2 + \beta_1 \alpha_s^3 + \dots) \quad (2.4)$$

where β_j is referred to as the $j+1$ -loop beta function coefficient. For the 1-loop case and within the $\overline{\text{MS}}$ scheme: $\beta_0 = (33 - 2n_f)/(12\pi)$ where n_f is the number of active quark flavors in the calculation. The second is

$$\gamma(\alpha_s) = -\mu_R \frac{1}{m} \frac{\partial m}{\partial \mu_R}, \quad \gamma(\alpha_s) = \gamma_0 \alpha_s + \gamma_1 \alpha_s^2 + \dots \quad (2.5)$$

where γ is known as the mass anomalous dimension and its first coefficients are $\gamma_0 = 1/\pi$, $\gamma_1 = 1/(16\pi^2) [202/3 - 20n_f/9]$.

The solutions of these equations lead to the *running* of the coupling constants: they depend on the reference scale. For example, the running of α_s solved at LO is,

$$\alpha_s(\mu_R^2) = \frac{\alpha_s(\mu_0^2)}{1 + \beta_0 \alpha_s(\mu_0^2) \log(\mu_R^2/\mu_0^2)} \quad (2.6)$$

¹Where γ_E is the Euler constant.

In the case of the masses, solving the Eq. (2.5),

$$m(\mu_R^2) = m(\mu_0^2) \exp \left[- \int_{\alpha_s(\mu_0^2)}^{\alpha_s(\mu_R^2)} \frac{\gamma(\alpha_s)}{\beta(\alpha_s)} d\alpha_s \right] \quad (2.7)$$

is obtained.

Since $\gamma(\alpha_s)/\beta(\alpha_s)$ is positive, quark masses in the \overline{MS} scheme are smaller at higher energies.

In both cases the result can be expressed in terms of the value at a reference scale μ_0 or in terms of the non-perturbative constant Λ_{QCD} which is the scale where the coupling diverges. Only for scales with $\mu_R \gg \Lambda$ ($\alpha_s \ll 1$) the perturbative expansion is meaningful. Λ_{QCD} depends on the renormalization scheme and on the number of active flavors in the calculation.

Renormalization of the quark masses: pole and \overline{MS} quark masses

Specifically for the quark mass renormalization, another option is possible and often used in perturbation theory: the pole mass (or on-shell mass) scheme. The full quark propagator at LO is given by the Dyson summation of the leading-order quark propagator without corrections plus all the gluon propagator one-loop self-energy contributions, as it can be seen schematically in Fig. 2.3 (up and down respectively).

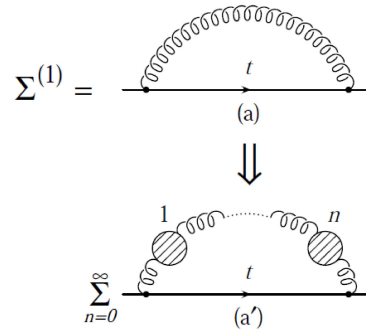


Figure 2.3: Dyson summation of the leading-order quark propagator. In the first row the diagram contributing to the quark self-energy at leading order in QCD is shown. In the second row, the result for summing to all orders in $\beta_0\alpha_s$.

The full propagator is written in terms of the renormalized quark mass and self-energy:

$$S(q) = \frac{1}{q - m_R - \Sigma_R} \quad (2.8)$$

where the self energy, in general, shifts the location of the pole of the propagator.

The pole mass renormalization scheme is chosen in such a way that the mass will

be the pole of the propagator:

$$\Sigma_R(q^2 = m^{pole}) = 0 \quad (2.9)$$

Since m^{pole} and $\bar{m}(\mu_R)$ are both the renormalization of the same coupling, a relation between both can be obtained. At NLO this relation is:

$$m^{pole} = \bar{m}(\bar{m}^2) \left[1 + \frac{4}{3\pi} \alpha_s(\bar{m}^2) + O(\alpha_s^2) \right] \quad (2.10)$$

It should be noticed that:

- a) the different mass schemes cannot be distinguished at LO;
- b) physics are independent of the choice of the mass scheme.

2.1.1.2 Infrared divergences and infrared safe observables

Virtual corrections may introduce other kind of divergences: the infrared (IR) divergences. They originate from soft or collinear configurations of the loop momentum and, as it happens with the UV divergences, they can be regularized. The real corrections to the Born diagrams (the LO diagrams) give emission of quarks and gluons in the final state. Diagrams of this type, as well as the virtual diagrams, are schematically shown in Fig. 2.4.

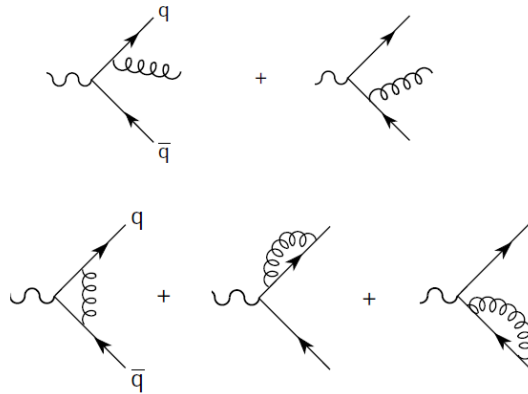


Figure 2.4: Gluon real emission (uppermost diagrams) and virtual (lowermost diagrams) corrections to the final state $X \rightarrow g \rightarrow q\bar{q}$ at LO

Real and virtual corrections lead to divergent integrals $\sim \int \frac{1}{(k_q+k_g)^2}$, which are divergent in two different regimes:

- collinear regime, when the final partons become collinear $k_q || k_g$ and indistinguishable;
- soft regime, when the parton emission is soft $E_g \rightarrow 0$.

IR safe observables

The divergences in the virtual and real corrections have the same form. The divergences from both corrections can be regularized to be cancelled with each other. The theoretical foundation is provided by the Kinoshita-Lee-Nauenberg (KLN) theorem [34, 35]. This theorem states that the divergences will cancel for properly defined observables. These observables are called infrared safe observables and fulfill the following requirements:

$$\begin{aligned} \hat{O}_{n+1}(\dots, k_i, \dots, k_j, \dots) &\xrightarrow{k_i \parallel k_j} \hat{O}_n(\dots, \cancel{k_i}, \dots, \cancel{k_j}, \dots, k_i + k_j, \dots) \\ \hat{O}_{n+1}(\dots, k_{soft}, \dots) &\xrightarrow{k_{soft} \rightarrow 0} \hat{O}_n(\dots, \cancel{k_{soft}}, \dots) \end{aligned} \quad (2.11)$$

which means that they are not sensitive to the collinear (first line) and soft (second line) emissions.

For example, let's consider two observables which are calculated for quark-antiquark pairs ($q\bar{q} + X$) final states and where the NLO corrections predict an extra gluon in the final state through real corrections, i.e. $q\bar{q} + g$:

- *the inclusive cross section* $\sigma(q\bar{q})$ is an IR safe observable since it contains all the possible final states $q\bar{q} + ng$ with $n = 0, 1 \dots$;
- *the number of final partons* is not a IR safe observable since the emission of a soft/collinear gluon modifies the final state multiplicity.

However, it is possible to define properly an IR safe observable that measures the final state multiplicity by defining the final state in a way that a soft/collinear emission does not modify the final state. Such observables are defined as a function of final objects which are non-sensitive to soft/collinear emissions. These objects can be obtained by clustering final state partons into the so-called jets. These are studied more deeply in Section 2.3.

Full NLO calculations

Assuming that the UV-divergences have been removed by renormalization and an IR safe observable has been defined, full NLO calculations can be performed. The soft and collinear divergences that appear in the NLO corrections have universal behavior. For the particular case of the cross section observable for a $x \rightarrow n - \text{partons}$ process, the calculation at NLO can be represented schematically as:

$$\sigma^{NLO} = \int_n \left(d\sigma^B + d\sigma^V + \int_1 d\sigma^A \right) + \int_{n+1} (d\sigma^R - d\sigma^A) \quad (2.12)$$

where $d\sigma^B$, $d\sigma^V$ and $d\sigma^R$ refer to the tree level contributions, virtual one-loop corrections and the real emission terms respectively. The $d\sigma^A$ correspond to the subtraction

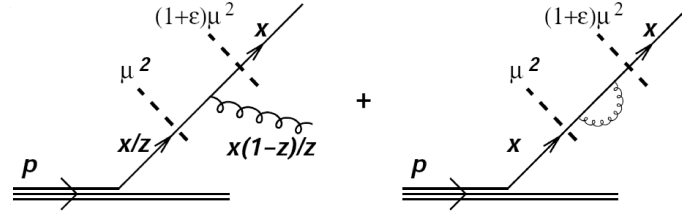


Figure 2.5: Initial state splitting. In the left, the emission of a gluon before the hard process changes the momentum of the quark that participates into the hard interaction and, the gluon, introduces a divergence in the integral in the collinear limit. In the right, the virtual contribution in the incidental quark that will cancel the the previous divergences.

terms needed to cancel the infrared singularities numerically. Due to the universal behavior of the singularities, the counter-terms of any specific process can be calculated using non process dependent algorithms. This way to deal with the IR divergences is called subtraction method, i.e., the Catani-Seymour dipole subtraction method [36].

2.1.2 Factorization and parton distribution functions

High energy interactions between hadrons occur between their internal constituents or partons: quarks and gluons. The hard interaction is calculated perturbatively thanks to the behavior of the strong coupling constant at high energies (asymptotic freedom) but the structure of the hadrons cannot be calculated perturbatively: it is derived from data. The two pieces of the total cross section in Eq. (2.2) are evaluated separately and independently, and finally factorized together to give the final result. In principle, the structure of the hadron can be studied by Lattice QCD calculations, but the accuracy that they can reach at the moment is not competitive with the high accuracy that hadron collider experiments demand.

In this context, the structure of the incident hadrons is modeled by the parton distribution functions (PDFs) which describe the possibility of finding a given parton with a specific fraction of momentum of the incident hadron. Figure 2.5 shows two possible initial states of a parton that carries the fraction x of the total p momentum of the hadron just before the hard interaction is produced. In the case that the hard interaction occurs after some parton splitting (leftmost diagram of the figure), the momentum entered in the hard process is lower than the initial fraction of hadron momentum that the mentioned parton carry, $x/z > x$. The hard interaction cross section also gets contributions from the virtual terms (rightmost diagram of the figure). Both contributions present divergences of the same type of the divergences presented in Section 2.1.1.2 and similarly they are removed by dimensional regularization and factorization. In a qualitative picture, the emissions that occur with $k_{\perp} \lesssim \mu_F$ are absorbed by the PDFs and the emissions $k_{\perp} \gtrsim \mu_F$ arise explicitly in the $O(\alpha_s)$ term, where the μ_F is the factorization scale.

The explicit dependence of the PDFs on μ_F is formally written in the Dokshitzer-Gribov-Lipatov-Altarelli-Parisi (DGLAP) evolution equation [37, 38, 39]. A simplified

version, where just one single quark flavor is included, reads:

$$\frac{d}{d \ln \mu_F^2} \begin{pmatrix} q \\ g \end{pmatrix} = \frac{\alpha_s(\mu_F^2)}{2\pi} \begin{pmatrix} P_{qq} & P_{qg} \\ P_{gq} & P_{gg} \end{pmatrix} \otimes \begin{pmatrix} q \\ g \end{pmatrix} \quad (2.13)$$

where represents the convolution

$$P_{ij} \otimes q = \int_x^1 dz P_{ij}(z) \frac{q(x/z, \mu_F^2)}{z} \quad (2.14)$$

of the so called splitting functions, $P_{ij}(z)$, with the parton distributions functions of the hadron H ($f_{q/H}(x/z, \mu_F^2) = q(x/z, \mu_F^2)$ and $f_{g/H}(x/z, \mu_F^2) = g(x/z, \mu_F^2)$). The splitting functions give the probability that a parton of type j converts into a parton type i carrying fraction z of the momentum of parton j . These quantities are universal and do not depend on the hard process. At first order and considering massless quarks, they are:

$$\begin{aligned} P_{qq}(z) &= C_F \left(\frac{1+z^2}{1-z} \right)_+ \\ P_{qg}(z) &= T_F [z^2 + (1-z)^2] = P_{\bar{q}g} \\ P_{gq}(z) &= C_F \left[\frac{1+(1-z)^2}{z} \right] \\ P_{gg}(z) &= 2C_A \left[\frac{z}{(1-z)_+} + \frac{1-z}{z} + z(1-z) \right] + \delta(1-z) \frac{11C_A - 4n_f T_F}{6} \\ P_{q\bar{q}}(z) &= P_{q\bar{q}}(z) = 0 \end{aligned} \quad (2.15)$$

where the subscript plus represents the “plus” prescription ¹.

The evolution of the PDFs with the scale is predicted perturbatively by the DGLAP equation. It predicts that, even if the initial condition is pure quark (gluon), evolution generates some amount of gluon (quark) density. Moreover, it is predicted (for example in Fig. 2.6) a depletion of the PDFs at large x and its increasing at low x , specially for gluons. It is common to choose the μ_F value as the scale of the interaction $Q^2, m_t^{\text{pole}}, \dots$ to minimize the size of the higher order corrections similar to the ones that appears in Eq. (2.2). The non-perturbative physics is characterized by the dependence on x for a fixed Q_0^2 which are evaluated by direct comparison with experiments: Deep Inelastic Scattering (DIS), neutrino scattering with hadrons, differential distribution of jet spectrum produced in hadron hadron collisions...

Different groups (MSTW, CTEQ, etc) (see, for example, Ref. [41]) provide PDFs with their associated uncertainties. They have been exhaustively tested and contin-

¹The “plus” prescription is defined as:

$$\int_x^1 dz [g(z)]_+ f(z) = \int_x^1 dz g(z) f(z) - \int_0^1 dz g(z) f(1) \quad (2.16)$$

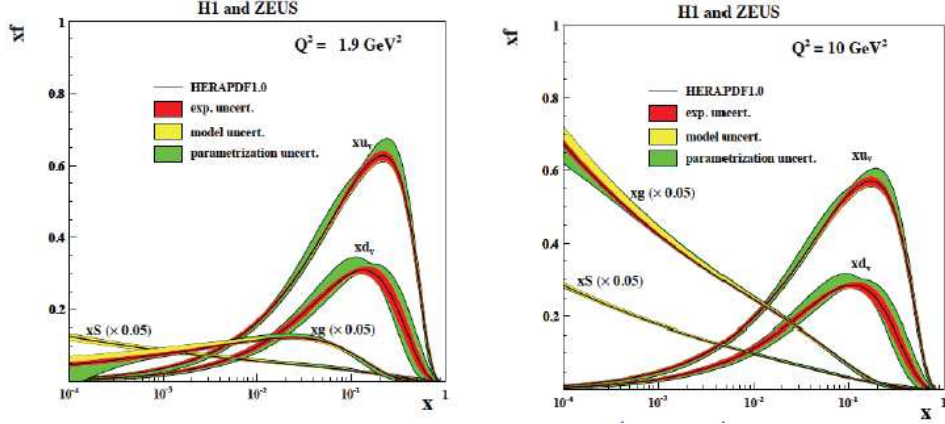


Figure 2.6: The distribution of different partons species in the HERAPDF1.0 parametrization at a scale $Q^2 = 1.9 \text{ GeV}^2$ (leftmost plot) and $Q^2 = 10 \text{ GeV}^2$ (rightmost plot). Figure taken from Ref. [40].

ously updated and used as input by hadron hadron collider experiments to perform their analysis. It is important to remark that the evolution equation presented here has been written for the leading-order case with splitting functions at the same order. NLO and NNLO corrections terms of Eq. (2.13) have also been calculated. The improvement of the PDF by using these corrections can be seen in Fig. 2.7.

2.2 Monte Carlo Tools

In the previous section, fixed order calculations have been presented. NLO predictions may introduce large logarithmically enhanced corrections in some regions of the phase space, where soft and collinear emissions spoil the perturbative behaviour. This can be improved through the resummation of leading logarithmically enhanced terms through the so called parton shower evolution (PS). Moreover, predictions of the cross section including the final states with very high particle multiplicity are desired in order to compare with the experimental results. These predictions should allow to incorporate experimental cuts, such as lepton acceptances, cuts on jets, etc... And they have to be predicted at the level of hadronized particles.

Naively, the high energy quarks and gluons predicted as final states in the fixed-order calculations evolve until they are bound into hadrons at low energies. This evolution is summarized in the following points:

1. High energy quarks and gluons are produced by the hard interaction (predicted using fixed-order calculations).
2. These highly accelerated quarks and gluons radiate (similar to the QED radiation from accelerated electric charges) showering more quarks and gluons until the energies are low enough. To explain the physics that happens at this regime, the Parton Shower approach is used.

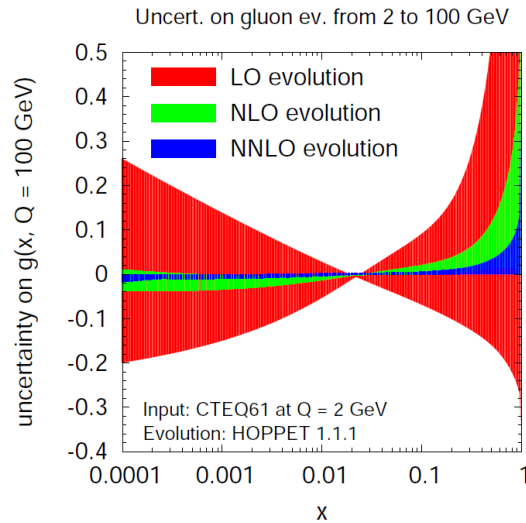


Figure 2.7: Uncertainties on the evolution of the gluon distribution from a fixed (CTEQ61) input at scale 2 GeV up to 100 GeV, for LO, NLO and NNLO evolution. The bands correspond to the envelope of the results with three scale choices $x_\mu = 1, 2, 1/2$ and what is plotted is the ratio to the result at a scale of 100 GeV, as obtained with NNLO evolution using $x_\mu = 1$. Figure extracted from Ref. [?]

3. Finally, these low-energy quarks and gluons are bound into hadrons. This process of hadronization is usually approached from phenomenological models, since the convergence of the perturbative expansions dependent on the α_s breaks down.

The way to calculate the fixed-order has been introduced in Section 2.1. In section 2.2.1 the principles that the Standard Monte Carlo programs (SMC) use to estimate the PS in the regime of soft and collinear emissions starting from a LO prediction of the hard interaction are briefly reviewed. Also in this section, some of the approaches developed to estimate how the hadronization processes happen are, briefly, presented. In Section 2.2.2, the way to match NLO calculations with parton shower algorithms is discussed.

2.2.1 Introduction to the Parton Shower algorithms in Standard Monte Carlo programs

The SMC programs usually perform LO calculations of the process to study. They implement the Parton Shower starting from the final state predicted using fixed LO calculations. Once the LO prediction of the final state is calculated, each quark or gluon in this final state can radiate softer quarks or gluons: the partons split. The general equation for a parton splitting (Fig. 2.8) in the collinear and soft approximation

is:

$$\sigma_{n+1} \simeq \sigma_n \frac{dp_T^2}{p_T^2} dz \frac{\alpha_s}{2\pi} P_{i,jk}(z) \quad (2.17)$$

where $P_{i,jk}(z)$ are the DGLAP splitting functions.

The squared transverse momentum p_T^2 can be written as a function of the emission angle: $p_T^2 \simeq z^2(1-z)^2\theta^2$ which in the soft and collinear limit fulfill the relation $\frac{d\theta^2}{\theta^2} = \frac{dp_T^2}{p_T^2}$.

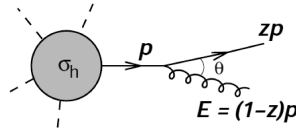


Figure 2.8: The quark i splits in j and the emitted gluon k . For this particular splitting, $P_{i,jk}(z) = C_F \frac{1+z^2}{1-z}$

The evolution of the partons from high energy to lower energies can be calculated in a recursive way considering that the subsequent emissions are ordered in some way (i.e. angle θ^2 , transverse momentum p_T^2) making each new emission more and more close to the collinear regime up to a predefined IR-cutoff (i.e. $p_T^2 > Q_0$) where the perturbative expansion breaks down. The chosen variable to perform the ordering is, in general, called the ordering variable t .

This evolution scheme only considers the real emissions of the partons (in the collinear and soft emissions regime) but, actually, the logarithmic corrections must be included in the parton shower. This is done through unitary constraints: the probability to have a resolvable emission plus the probability of not having it is equal to 1. Therefore the probability of going from the scale t_0 to the lower scale t_1 with no emission is recursively given by:

$$\begin{aligned} dP_{no-emission}(t_0, t_1) &= \lim_{N \rightarrow \infty} \prod_{n=1}^N \left(1 - \sum_{jk} \frac{\alpha_s(t_n)}{2\pi} \frac{dt_n}{t_n} \int P_{i,jk}(z) dz \right) \\ &= \exp - \int_{t_1}^{t_0} \frac{\alpha_s(t)}{2\pi} \frac{dt}{t} \sum_{jk} \int P_{i,jk}(z) dz \\ &\equiv \Delta_i(t_0, t_1) \end{aligned} \quad (2.18)$$

where Δ is the so called Sudakov-Factor and it resums all the leading virtual contributions.

The probability to generate the first branching at any scale from a higher t is independent from subsequent ones. Therefore, Eq. (2.18) can be written as a function

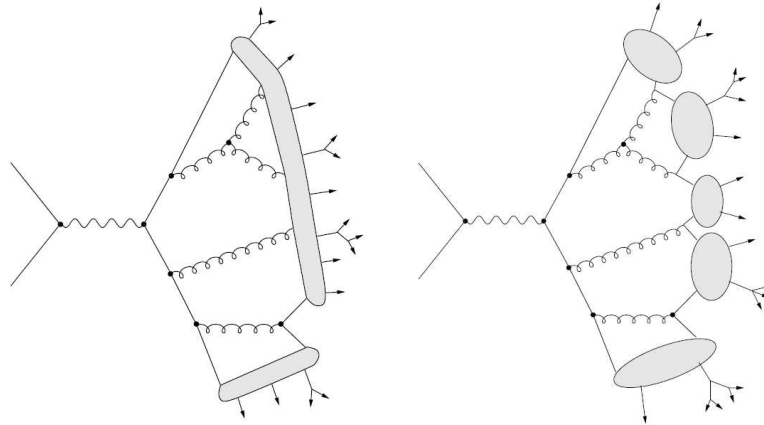


Figure 2.9: Color assignments are required in the hadronization model: Lund string model (leftmost plot), the cluster model (rightmost plot) etc. in order to form color singlet structures from color connected partons. One widely-used model involves stretching a colour ‘string’ across quarks and gluons, and breaking it up into hadrons (Lund model implemented in PYTHIA). The second model breaks each gluon into a $q\bar{q}$ pair and then groups quarks and anti-quarks into colourless ‘clusters’, which then give the hadrons (cluster model implemented in HERWIG).

of the Sudakov-factor:

$$d\sigma_n = d\sigma_0 \left[\Delta(t_0) + \Delta(t) \frac{\alpha_s}{2\pi} \frac{dt}{t} P(z) \right] \quad (2.19)$$

where $\Delta(t) = \Delta(t, t')\theta(t - t')$.

This equation explains the evolution of the parton shower produced by partons in the final and initial states (FSR and ISR) of the hard interaction.

Soft singularities ($z \rightarrow 0$) are also present in the DGLAP equations that contain gluons in the final state of the branching. Wide angle soft gluons cannot resolve the difference between a gluon and collinear quark and a gluon with the same quantum numbers. This is known as the color coherence and it is sensitive to the choice of the ordering variable.

SMC programs also have to estimate the evolution of the hadrons after the hard interaction which modify the internal structure of the hadrons. This is usually called *underlying event* (UE). These interactions, together with the FSR and ISR parton shower lead to states populated by high multiplicity colored partons. SMC programs must also estimate the QCD interactions between all these intermediate partons and also interactions between other partons that are softer than the primary hard interaction (called *multiple interactions*, MI). Finally, when showered partons reach to low energy regimes, the perturbative behavior of the parton shower breaks down (the perturbative expansion diverges at low energies). In this step, phenomenological models are used to color-connect these low energy partons and hadronize them. The most commonly used hadronization models are the Lund String Model and the Cluster Model. A pictorial scheme of how both hadronization models work can be seen in Fig. 2.9

These features of SMC programs (color coherence, UE, MI, hadronization, etc...)

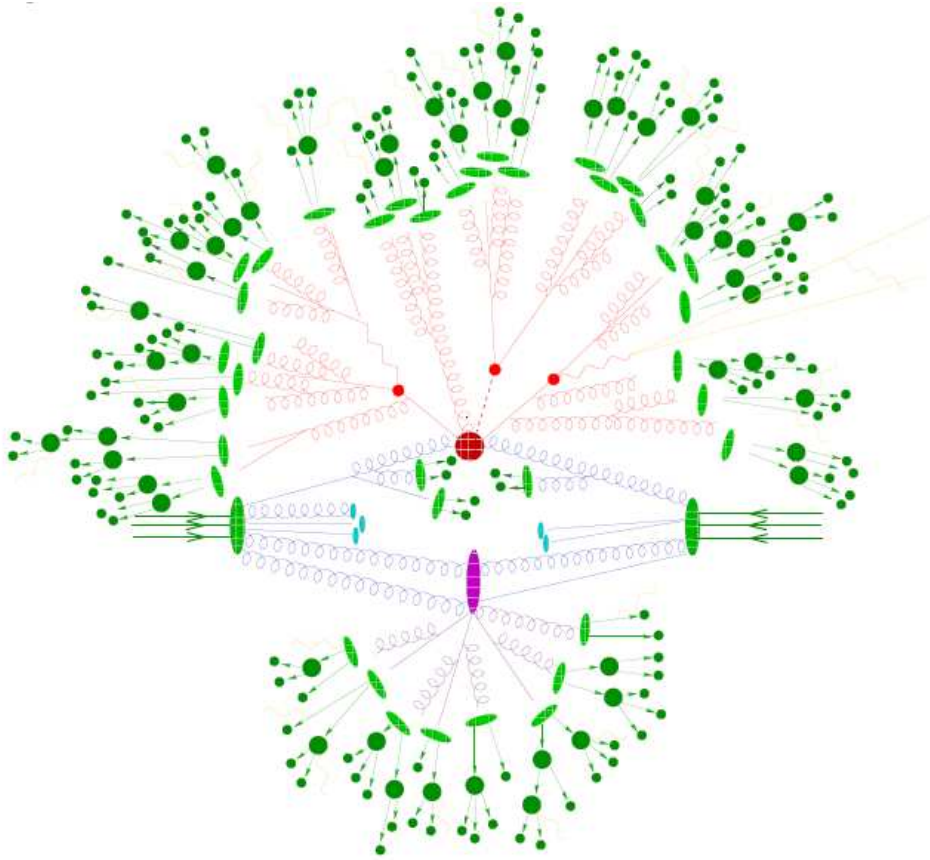


Figure 2.10: Schematic representation of a high energy hadron-hadron collision. Figure taken from Ref. [31].

surpass the scope of this thesis and will not be discussed in much more detail. We will just summarize the general features of two of the most known SMC programs, PYTHIA [42] and HERWIG [43].

PYTHIA

In the last versions of PYTHIA (PYTHIA8, in C++) the parton shower are p_{\perp} -ordered, interleaved with multi-parton interactions and dipole-style recoil. The matrix element for first emission in many processes is included and a large range of hard processes too (at LO). The hadronization is performed by the Lund String Model which tends to describe hadronization processes better than the cluster models.

HERWIG

Last versions (HERWIG++) are also implemented in C++ language. HERWIG performs the angular-ordered parton shower optimizing in this way the color coherence. It also adds a quasi-collinear limit and recoil strategy based on colour flow. It include some NLO processes automatically matched with the parton-shower algorithm (see next section).

Moreover, a general picture with the complete evolution of an hadronic interaction simulated by SMC programs is shown in Fig. 2.10. In the central part of the picture, we see the representation of both incident hadrons, with the three valence quarks represented by three straight lines (all in green). The interacting partons of both hadrons are represented by dark-blue lines. In the central part of the figure, the partonic hard interaction is shown with maroon lines and a maroon bullet. Just above of the hard interaction, the FSR radiation is shown, with red lines and bullets. And just below the hard interaction, the ISR interactions are shown using blue lines. The magenta bullet represents the UE and MI processes. When, for all the processes simulated, the parton shower reaches low energies, the fragmentation process starts. It is represented by light-green bullets which afterwards produce the hadrons (dark-green bullets) which, afterwards, decay (small dark-green bullets).

2.2.2 Next-to-Leading order and Parton Showering

Next-to-leading order calculations are required for high precision measurements. As it has been presented previously, they have to be matched with parton shower algorithms to reduce the large corrections caused by the soft and collinear corrections. Since the real corrections to the fixed order cross section includes also soft and collinear emissions, a naive combination of NLO predictions with a parton shower can not be performed without avoiding a double-counting for these emissions.

One possible solution is based on the inclusion of further real emissions and avoids the double counting by a proper matching, i.e. the MLM matching algorithm [44, 45, 46]. Since the approach is based on LO predictions, it suffers from large uncertainties under scale variations.

General methods to match NLO fixed order calculations with PS algorithms have been developed, i.e., MC@NLO [47] and POWHEG [48]. In this chapter the POWHEG method is described in more detail, as it is most often referenced in this thesis even though both approaches are equivalent.

The POWHEG method can be summarized in three steps:

- It generates only the hardest emission including full tree level real matrix element and virtual corrections (see next paragraphs for more details);
- the shower generates subsequent emissions, performing (N)LL resummation of collinear and soft partons;
- the emissions performed by the PS are vetoed if harder than the first.

The POWHEG method to calculate the hardest emission is based on the following redefinition of parton shower equation (Eq. (2.19)):

$$d\sigma_{NLO} = \bar{B}(\Phi_n) d\Phi_n \left[\Delta_{POW}(\Phi_n, p_{\perp}^{min}) + \Delta_{POW}(\Phi_n, k_{\perp}) \frac{R(\Phi_{n+1})}{B(\Phi_n)} \right] d\Phi_{rad} \quad (2.20)$$

where the $\bar{B}(\Phi_n)$ includes all the NLO cross section information with the integral over the phase space of the extra emission done implicitly, in such a way that $\sigma_{NLO} = \int \bar{B}(\Phi_n) d\Phi_n$. The $R(\Phi_{n+1})$ refers to the real correction terms and the complete n phase space is defined as $d\Phi_{n+1} = d\Phi_n d\Phi_{rad}$. The factors associated to the soft and collinear emissions in Eq. (2.18) and Eq. (2.19) have been exchanged with a factor between the real corrections and the Born term:

$$\frac{\alpha_s}{2\pi} \frac{P(z)}{t} \longleftrightarrow \frac{R(\Phi_{n+1})}{B(\Phi_n)} \quad \Delta \longleftrightarrow \Delta_{POW} \quad (2.21)$$

which are equivalent in the soft and collinear limit

$$\lim_{p_T \rightarrow 0} \frac{R(\Phi_{n+1})}{B(\Phi_n)} = \frac{\alpha_s}{2\pi} \frac{P(z)}{p_T^2} \quad (2.22)$$

where the transverse momentum, p_T , is chosen as ordering variable.

The POWHEG-Sudakov factor, i.e. the probability of not emitting with transverse momentum harder than p_T is now related to the actual real corrections which keep the LL accuracy of the parton shower programs. In the soft and collinear region $\bar{B} \simeq B(1 + O(\alpha_s))$. Moreover, in the hard p_T region, the NLO accuracy is preserved since $\Delta_{POW} \simeq 1$. Events (with the hardest emission included) are generated according to Eq. (2.20) and afterwards the parton shower of a SMC program is implemented vetoing emissions harder than the generated by POWHEG.

The MC@NLO method follows similar ideas (actually MC@NLO was the first method to be developed). This method first calculates the NLO matrix element corrections to an n -body process using subtraction terms. Then the first shower emission of an n -body topology populating an $n + 1$ phase space is calculated analytically without using Sudakov terms. In the next step, the shower expression is subtracted from the $n + 1$ ME and the rest of σ_{NLO} is considered as n -body. Finally, the shower is added to both kind of events.

2.3 Jet physics

The concept of a “jet” has been introduced very naively in Section 2.1.1.2. When quarks and gluons are present in the final state (partonic cross section) an infrared safe prescription to define final objects, called jets, is needed. At parton level just a few partons are present in the final state but when parton shower calculations are performed, new quarks and gluons appear due to soft and collinear emissions. This must not change the number of final number of jets. The same must occur when the partons hadronize and they interact with the detector. Both theory and experimental results are often presented in terms of jet cross section and thus jets provide the

meeting point between the two.

The definition of a jet involves two steps:

- Jet algorithm: definition of the criteria and rules chosen to decide which particles (or partons) have to be combined. These rules may be based on distance and energy parameters like the angular distance or the p_T .
- Recombination scheme: combine the particles (or partons) chosen to group inside the jet. One example is the E-scheme which simply adds the four momentum of the particles.

The historical approach to the jet algorithm definition in hadron hadron colliders is based in the so called cone-algorithms. In a very naive picture they chose, in some way, the hardest particles and iteratively join to them all the particles inside a cone of radius R . They are not described in detail, as they are no longer used at ongoing hadron-hadron colliders. The reason to not use them is that, to some extent, they all suffer from infrared unsafety. The present approach to the definition of jet algorithms for hadron colliders consists in the so called clustering algorithms. In this chapter, the generalized k_T algorithms are presented and discussed since they are the most commonly used by LHC general purpose experiments.

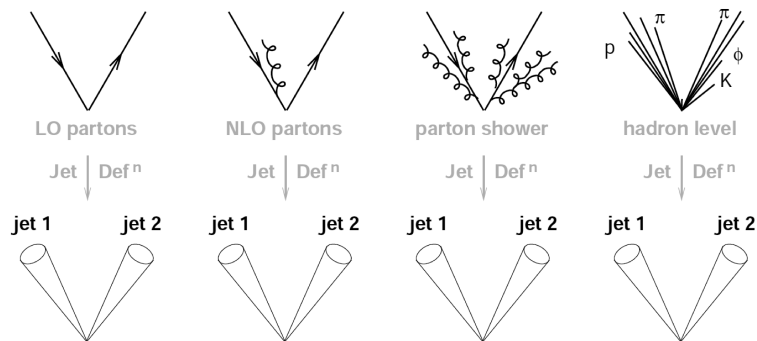


Figure 2.11: The pictures refer to the application of a jet definition to a variety of predictions that differ just through soft/collinear branching should give identical jets in all cases and with the real data reconstructed through the interaction of the hadrons with the detector.

Generalized k_T algorithm

This algorithm has been designed for hadron hadron collisions and DIS. It can be applied to partons or particles which, in both cases, will be called pseudojets from now on. It defines two distances: d_{ij} between each pair of pseudojets and d_{iB} between

each pseudojet and the beam:

$$d_{ij} = \min(p_{Ti}^{2p}, p_{Tj}^{2p}) \frac{\Delta R_{ij}^2}{R^2} \quad (2.23)$$

$$d_{iB} = p_{Ti}^{2p}$$

where p is some integer value which specifically define the algorithm, R is a parameter whose role is similar to the R used in cone algorithms and that is usually chosen to be $R \lesssim 1$, and $\Delta R_{i,j} = \sqrt{(\eta_i - \eta_j)^2 + (\phi_i - \phi_j)^2}$ ¹. The inclusive algorithm proceeds as follows:

- 1 Searching of the smallest of the d_{ij} and d_{iB} for all possible i, j .
- 2a If the minimum is a distance d_{ij} then the i and j pseudojets are recombined into a new pseudojet following the recombination scheme.
- 2b If the minimum is the distance d_{iB} , then the pseudojet i is removed from the list of and the pseudojet is called a jet.
- 3 Repeat until no pseudojets remain

The usual choices of p are: $p = 1$ (k_T algorithm), $p = 0$ (Cambridge/Aachen C/A) or $p = -1$ (anti- k_T algorithm). The features of the k_T and anti- k_T algorithms are briefly discussed in the following paragraphs.

k_T algorithm: In the k_T algorithm arbitrarily soft pseudojet can form jets. A minimum cut-off $p_{T,min}$ is usually introduced. It defines what a jet is in “hard” physics. The R parameter can be seen as a cone radius. If $\Delta R_{i,j} < R$ then $d_{ij} < d_{iB}$ and both pseudojets will be recombined instead of forming separated jets. If a pseudojet is well separated of all the rest of pseudojets, $\Delta R_{i,j} > R$, then it will be classified as an independent jet. The k_T -jets can have very irregular edges because many of the soft pseudojets may have an early recombination in patterns that are determined by random distribution of these pseudojets in a detector environment. The irregular edges can complicate the energy calibration of jets.

A very attractive feature of this algorithm is that it is possible to study, for every jet, the clustering sequence from the pseudojets to the final jets. Studying the jet substructure can be very interesting for high- p_T physics where objects are very collimated and can form jets with a rich substructure [49].

anti- k_T algorithm: In this case, the recombination of pseudojets is performed around high p_T pseudojets and grow concentrically around them. Their jets have very conical edges which make their energy calibration easier. This algorithm has been adopted as the default algorithm for the LHC collaborations with R between 0.4 and 1 depending on the experimental group and in the specific analysis.

¹The η variable is the so-called pseudorapidity defined as $\eta = -\ln[\tan(\theta/2)]$ where θ is the angle between the pseudojet momentum p and the beam axis. The ϕ angle is defined as the azimuthal angle in the transverse plane

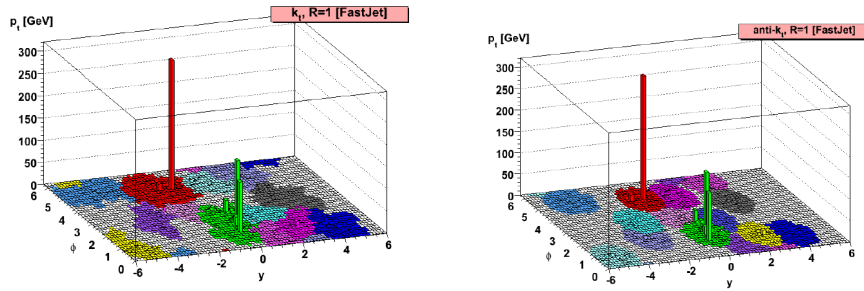


Figure 2.12: Regions of the $y-\phi$ plane covered by jets in an illustrative (simulated) hadron-collider event with the inclusive longitudinally-invariant k_t algorithm (left) and the anti- k_t algorithm (right). The y denotes the rapidity, $y = \frac{1}{2} \ln \frac{E+p_z}{E-p_z}$, which is equivalent to the pseudorapidity. The z direction is defined as the beam direction. Figure taken from Ref. [49].

To study high-multiplicity final states in hadron hadron colliders, a good understanding of jet-physics is needed. This, together with the theoretical calculations using the pQCD approach, allows to understand and study the top-quark related physics.

3

Top-quark physics and a new method to measure its mass

The top-quark is the heaviest elementary particle discovered so far. It is predicted by the SM as the isospin partner of the b -quark and its mass has been measured to be ~ 35 times that of the b -quark (the second heaviest quark). Due to the large value of its mass, the top-quark presents the strongest coupling to the Higgs boson. Therefore, top-quark physics measurements are crucial to better understand the electroweak sector in the SM or in beyond Standard Model (BSM) theories. Specifically, the measurement of the top-quark mass is of high physics relevance. In this chapter, the current top-quark mass measurements are discussed and a new method based on its extraction from the measurement of jet rates is proposed.

This chapter starts with a short introduction to the top-quark physics and its role within the SM and BSM, in Section 3.1. In the following section, Section 3.2, current top-quark mass measurement methods are discussed and the latest measured values are presented. In Section 3.3 the basic requirements needed to define alternative methods to measure the top-quark mass are listed. Finally, in Section 3.4, the new method to measure the top quark mass from jet rates is presented and extensively discussed. This observable was presented for first time in Ref. [11] and has been used to extract the m_t^{pole} using ATLAS data, as it can be seen in Ref. [12] and with more detail in Chapters 5 and 6 of this thesis.

3.1 The top quark

The top quark was discovered at Fermilab in 1995 [3, 4] by the Tevatron experiments CDF and D0. Measurements of the top quark intrinsic properties have been carried out by the Tevatron and the LHC collaborations. It is the weak isospin partner of the b -quark with spin $s = 1/2$ since it is a fermion and has electric charge $Q = -2/3$. Its mass (Yukawa coupling with the Higgs) and the matrix elements of

the Cabibbo-Kobayashi-Maskawa (CKM) (V_{td}, V_{ts}, V_{tb}) are free parameters within the SM, although they are constrained (i.e. the unitarity of the CKM matrix constrains the V_{td}, V_{ts}, V_{tb} to be $V_{td}, V_{ts} \ll V_{tb}$).

A summary of the measured top-quark properties until the summer of 2014 can be seen in Fig. 3.1. Firstly, the top-quark mass measurements are listed. They are more extensively discussed in Section 3.2. Secondly, the difference between the quark and antiquark masses is listed. These results have been obtained by the Tevatron experiments and the CMS experiment at the LHC. Following, the top-quark decay width measured at Tevatron is listed. The top-quark EW couplings extracted from the measured W helicity fractions in top decays are listed: F_0 is the fraction of longitudinal and $F_{+(-)}$ the fraction of right-handed (left-handed) W bosons. F_{V+A} is the fraction of $V + A$ (vector plus axial couplings) current in top decays. Finally, the results for the different decay modes are summarized. The measurement of the top-quark electric charge is not in the table since current measurements are only able to exclude the $Q_t = -4/3$ at 95% CL which is predicted in some extension of the SM.

t

$$I(J^P) = 0(\frac{1}{2}^+)$$

$$\text{Charge} = \frac{2}{3} e \quad \text{Top} = +1$$

Mass (direct measurements) $m = 173.21 \pm 0.51 \pm 0.71$ GeV [a,b]
 Mass (\overline{MS} from cross-section measurements) $m = 160_{-4}^{+5}$ GeV [a]
 Mass (Pole from cross-section measurements) $m = 176.7_{-3.4}^{+4.0}$ GeV
 $m_t - m_{\bar{t}} = -0.2 \pm 0.5$ GeV (S = 1.1)
 Full width $\Gamma = 2.0 \pm 0.5$ GeV
 $\Gamma(Wb)/\Gamma(Wq(q = b, s, d)) = 0.91 \pm 0.04$

t-quark EW Couplings

$F_0 = 0.690 \pm 0.030$
 $F_- = 0.314 \pm 0.025$
 $F_+ = 0.008 \pm 0.016$
 $F_{V+A} < 0.29, CL = 95\%$

t DECAY MODES	Fraction (Γ_i/Γ)	Confidence level	P (MeV/c)
$Wq(q = b, s, d)$			—
Wb			—
$\ell\nu_\ell$ anything	[c,d] (9.4±2.4) %		—
$\gamma q(q=u,c)$	[e] < 5.9	$\times 10^{-3}$	95%
$\Delta T = 1$ weak neutral current (T1) modes			
$Zq(q=u,c)$	T1 [f] < 2.1	$\times 10^{-3}$	95%

Figure 3.1: Review of the measured top-quark properties in 2014 as they appear in the Particle Data Group book [25].

The top quark decays through the weak interaction by flavor changing processes. The ratio of the branching ratios (BR) of the top-quark decays are related to the CKM

matrix elements:

$$\frac{BR(t \rightarrow Wb)}{BR(t \rightarrow Wq)} = \frac{|V_{tb}|^2}{\sum_q |V_{tq}|^2} = |V_{tb}|^2 \sim 1 \quad (3.1)$$

being $q = d, s, b$ and the predicted branching ratios: $BR(t \rightarrow Wd) \simeq 0.0006\%$, $BR(t \rightarrow Ws) \simeq 0.17\%$ and $BR(t \rightarrow Wb) \simeq 99.9\%$ [25].

Owing to its large mass, $m_t \sim 173$ GeV, the top-quark lifetime becomes extremely short ($\sim 0.5 \times 10^{-24}$ s), inhibiting top-quark bound states to be formed. As an important consequence, top quarks offer the unique possibility to study the properties of a quasi-free quark: due to their parity violating and fast decay it is possible to study the top-quark polarization since the spin information is not diluted through the hadronization. The top quark can be identified in an experiment through the identification of its decay products. The b -quark produces a jet of particles and the W boson leaves its signature through its decay products: at LO, the W boson decays always in a lepton plus a neutrino (of the same flavor) or into two quarks (of different flavor) which produce two jets of particles. Thus top-quark pair events can be classified according to the decay of the W bosons produced by the top quarks. This is shown in Figure 3.2. Three main different topologies are usually differentiated:

Dileptonic channel: both bosons decay into lepton plus neutrino. This is $t\bar{t} \rightarrow b + \bar{b} + l_1 + \bar{\nu}_1 + \nu_2 + \bar{l}_2$. The signature of these events in the detector is: two jets produced by the b -quarks, two high p_T leptons of opposite sign and the presence of a large amount of missing E_T due to the presence of non-detected neutrinos. This channel is very clean but presents limited reconstruction efficiency due to the presence of the two neutrinos.

Hadronic channel: both bosons decay into quarks that produce high p_T jets. The signature of these events are four jets produced by the light quarks from the W boson and two jets produced by the b -quarks. There are no leptons to trigger and it is not easily distinguishable from the large SM QCD multijet background.

Semileptonic channel: is a mix of both previous channels, where one of the W bosons, produced from the decay of the top, decays leptonically and the other hadronically. In this case, the presence of a high p_T lepton allows to largely suppress the multijet background.

The top quarks are predominantly produced in pairs at hadron colliders through strong interactions. At the LHC, the energy of the collision was 7 and 8 TeV during 2011 and 2012 respectively which is ~ 4 times the energy obtained at the Tevatron. Moreover the LHC produces pp collisions while the Tevatron was colliding $p\bar{p}$. Therefore, at the LHC the $t\bar{t}$ pairs are produced mainly through gluon fusion ($gg \rightarrow t\bar{t} \sim 90\%$) while at the Tevatron the quark-antiquark annihilation ($q\bar{q} \rightarrow t\bar{t} \sim 85\%$) was the dominant production mechanism. The inclusive $t\bar{t}$ cross section predicted for the LHC working conditions has been calculated at next-to-next-to leading order (NNLO) in QCD including resummation of next-to-next-to-leading logarithmic (NNLL) soft gluon terms [50, 51, 52, 53, 54, 55]. The PDF and α_S uncertainties were calculated following the PDF4LHC prescription [56] for different sets of PDFs [41, 57, 58, 59, 60]. The results of these calculations, for a top quark pole mass of $m_t^{\text{pole}} = 172.5$ GeV are:

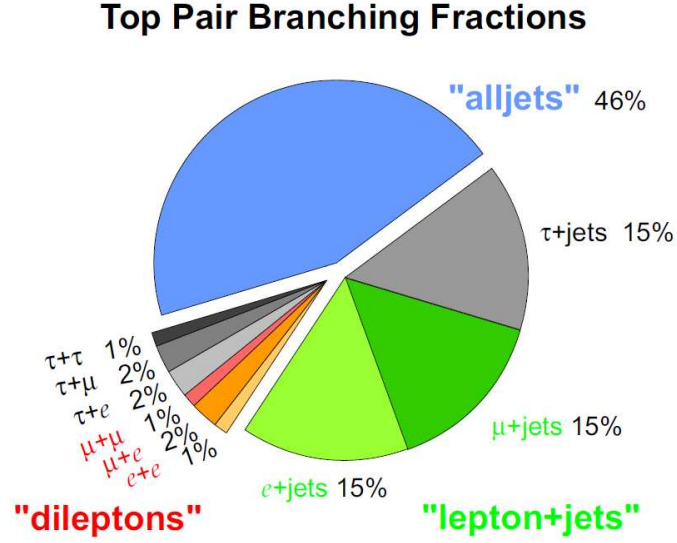


Figure 3.2: Graphical representation of the $t\bar{t}$ decay channels as a function of the W boson decay channels.

$$\begin{aligned}\sigma_{t\bar{t}} &= 177_{-11}^{+10} \text{ pb} \quad (\sqrt{s} = 7 \text{ TeV}) \\ \sigma_{t\bar{t}} &= 253_{-15}^{+13} \text{ pb} \quad (\sqrt{s} = 8 \text{ TeV})\end{aligned}\quad (3.2)$$

The collected integrated luminosity at the general purpose experiments placed in the LHC, i.e. CMS and ATLAS, is $\sim 5 \text{ fb}^{-1}$ at 7 TeV and $\sim 20 \text{ fb}^{-1}$ at 8 TeV (see Chapter 4) that corresponds to $\sim 9 \cdot 10^5$ (7 TeV) and $\sim 5 \cdot 10^6$ (8 TeV) $t\bar{t}$ events. With these values, the LHC is the largest top factory of the world and the ATLAS and CMS the machines that study its properties.

3.1.1 The special role of the top quark in the EWSB sector and in Beyond Standard Model theories

Due to the large value of the top-quark mass, the top-quark Yukawa coupling λ_t (see Eq. (1.16)) is very close to one,

$$\lambda_t = \frac{\sqrt{2}}{v} m_t \simeq 1 \quad (3.3)$$

this means that the top-quark has the strongest coupling to the Higgs boson and therefore the top quark represents an ideal laboratory for detailed tests of the Higgs mechanism. The loop corrections to the Higgs boson propagator contains very large

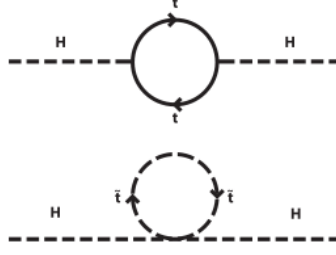


Figure 3.3: Cancellation of the Higgs boson quadratic mass renormalization between fermionic top quark loop (upper diagram) and scalar stop squark Feynman (lowermost diagram) diagrams in a supersymmetric extension of the Standard Model.

corrections specially due to the large top-quark mass, see Fig. 3.3 uppermost diagram, which translate into corrections to the squared Higgs boson mass of:

$$M_H^2 = M_H^2(LO) + \Delta M_H^2$$

$$\Delta M_H^2 = -\frac{3\lambda_t^2 \Lambda_{UV}^2}{8\pi^2} + \dots \quad (3.4)$$

where λ_t is the yukawa coupling of the top quark and Λ_{UV} is an ultraviolet momentum cutoff which is interpreted as the energy scale at which new physics enters to alter the high-energy behavior of the theory (assuming that there is new physics at such scale). In the SM there is no symmetry which protects such a strong dependence of the Higgs mass on a possible new scale. This is known as the *hierachy* problem of the Higgs.

Many Beyond Standard Models (BSM) propose different alternatives to avoid these fine tunings. In general, all these models expect deviations from the SM predictions in the top-quark sector. One of the most well known extension of the SM is the Supersymmetry. The supersymmetric models, called SUSY (see for example Ref. [61] for a more complete review), postulate the invariance of the theory under the interchange of fermions and bosons. According to this theory, each fermion should have a partner boson, and each boson should have a partner fermion. Therefore the SUSY theories predict a set of new particles, called superpartners. The scalar top superpartner (the *stop*) helps to cancel the large divergences within the Higgs mass loop corrections and *naturally* fix the large corrections:

$$M_H^2 = M_H^2(LO) + \Delta M_H^2 + \Delta M_H^2(stop)$$

$$\Delta M_H^2(stop) = \frac{\lambda_{stop}^2}{16\pi^2} \left[\Lambda_{UV}^2 - 2m_{stop} \ln \frac{\Lambda_{UV}}{m_{stop}} + \dots \right] \quad (3.5)$$

where λ_{stop} is the SUSY Yukawa coupling of the top-quark superpartner and m_{stop} is its mass. This equation is schematized in Fig. 3.3 lowermost diagram, in which the

loops generated by *stop* are shown.

On the other hand, the SM radiative corrections to the W mass are as follows:

$$\begin{aligned}
 M_W &= M_W^{LO} + \Delta r_{top} + \Delta r_H \\
 \Delta r_{top} &\simeq -\frac{3G_F m_t^2}{8\sqrt{2}\pi^2} \frac{1}{\tan \theta_W} \\
 \Delta r_H &\simeq \frac{11G_F M_Z^2 \cos \theta_W}{24\sqrt{2}\pi^2} \ln \frac{M_H^2}{M_Z^2}
 \end{aligned} \tag{3.6}$$

where G_F is the Fermi's constant, θ_W is the Weinberg angle, and m_t , M_H , M_Z are the top-quark, Higgs and Z boson masses respectively.

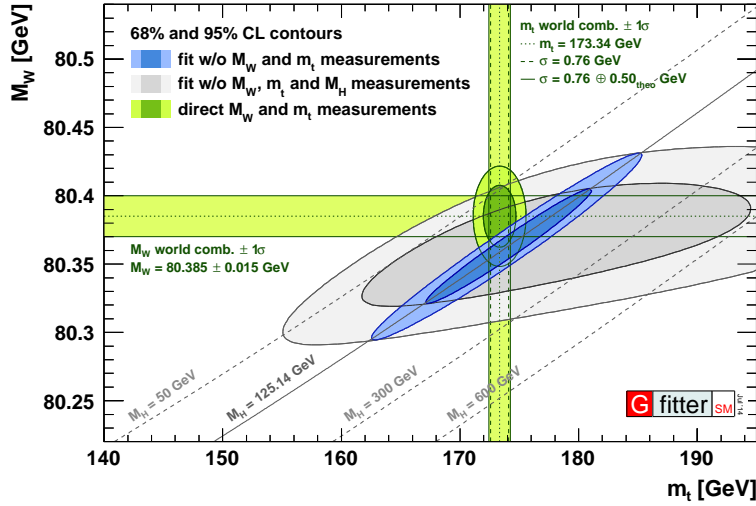


Figure 3.4: Contours of 68% and 95% confidence level obtained from scans of fits with fixed variable pairs M_W vs. m_t . The narrower blue and larger grey allowed regions are the results of the fit including and excluding the M_H measurements, respectively. The horizontal bands indicate the 1σ regions of the M_W and m_t measurements (world averages).

Using the SM framework, the W -boson mass and other observable quantities (the effective weak mixing angle $-\sin^2 \theta_{eff}$, the widths of the electroweak bosons, the strong coupling $-\alpha_s$, the branching ratio of the Z -boson into bottom quarks-...) can be calculated and used to evaluate the compatible values of the parameters within the SM (mass of the electroweak bosons, mass of the Higgs boson, mass of the top-quark, etc...). An example of this is shown in Fig. 3.4. The fit shows the compatibility of the measured Higgs, W and top-quark masses within the SM. This test of the validity of the SM depends strongly in the precision of the measurement of these masses. Measuring the top-quark mass with precision is crucial to perform these comparisons.

These quantities can be also calculated for different models (SM, the minimal

supersymmetric model MSSM,...). This is done in Ref. [62, 63] (including two-loop corrections for the precision observables [64, 65, 66, 67]) where M_W was predicted for different supersymmetric models and for the SM as a function of the M_H and m_t . The masses of the Higgs and W bosons can be measured with a high precision, therefore high accuracy top-quark mass measurements are crucial. The result of these calculations are shown in Figure 3.5, including the latest M_H measurements. With present accuracy the predictions of the SM and the MSSM are compatible with the measured values but the prospects to the increase of precision in the top-quark mass measurements may do one of the theories incompatible with the measurements.

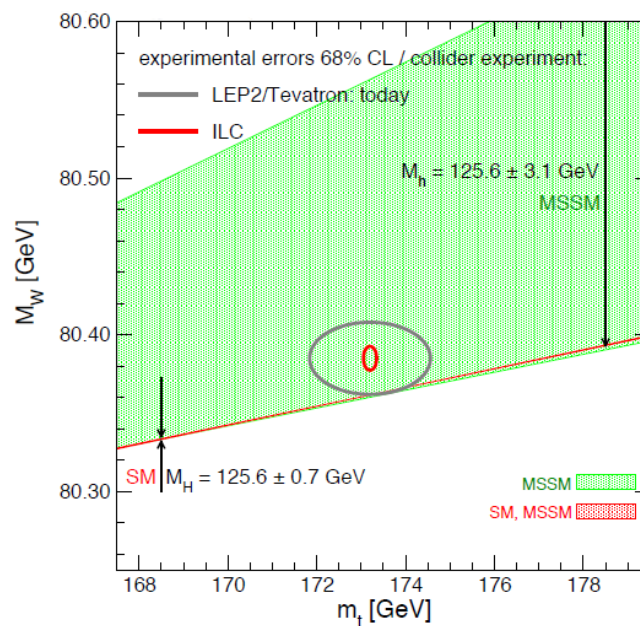


Figure 3.5: Prediction for M_W in the minimal supersymmetric standard model (MSSM) and the SM as a function of m_t in comparison with the present experimental results for M_W and m_t and the prospective accuracies (using the current central values) at the Tevatron. The allowed region in the MSSM, corresponding to the light-shaded (green) results from varying the SUSY parameters independently of each other in a random parameter scan. The allowed region in the SM, corresponding to the medium-shaded (red) results from varying the mass of the SM Higgs boson in the interval defined by the measured value $M_H = 125.6 \pm 0.7$ GeV. Figure produced using References Ref. [62, 63] and updated to the experimental results up to June 2014.

The study of the stability of the Higgs potential is also related to the measurement of the top-quark mass: loop QCD and Yukawa corrections to the relation between the quartic coupling (λ) and the Higgs mass are also dependent on M_W and m_t [68, 69, 70, 71]. The condition of absolute stability of the electroweak vacuum, $\lambda(\Lambda_{Planck}) \geq 0$, when the SM is extrapolated up to the Planck scale Λ_{Planck} can be calculated at

NNLO [71] and yields:

$$M_H > 129.6 \text{ GeV} + 2.0 \left(m_t^{\text{pole}} - 173.34 \text{ GeV} \right) - 0.5 \text{ GeV} \frac{\alpha_s(M_Z) - 0.1184}{0.0007} \pm 0.3 \text{ GeV} \quad (3.7)$$

where $\pm 0.3 \text{ GeV}$ is an estimate of the unknown higher order terms. Note that the “only” assumption made in this calculations is that there is no new physics until the Λ_{Planck} .

The stability condition dependence with the top-quark and Higgs masses taken from Ref. [70] is shown in Fig. 3.6. In the first figure two different top-quark mass measurements are used as input: the first one is the value of the kinematic m_t measured at the Tevatron, $m_t = 173.2 \pm 0.9 \text{ GeV}$, for which the vacuum stability requires indeed the Higgs boson to be $M_H \geq 129 \pm 1 \text{ GeV}$. However, this value of m_t is not unambiguously associated to any mass scheme and the theoretical uncertainty of this measurement is not fully understood. The second top-quark mass value used as input is the measurement of the top-quark pole mass extracted from the cross section measurement, $m_t^{\text{pole}} = 173.3 \pm 2.8 [70]$, for which the vacuum stability constraint becomes $M_H \geq 129.8 \pm 5.6 \text{ GeV}$. Therefore, very precise measurements of the Higgs and top-quark masses are needed to study the electroweak vacuum stability. The meta stability region is defined in the $M_H - m_t^{\text{pole}}$ plane for which the lifetime of the electroweak vacuum is longer than the age of the Universe.

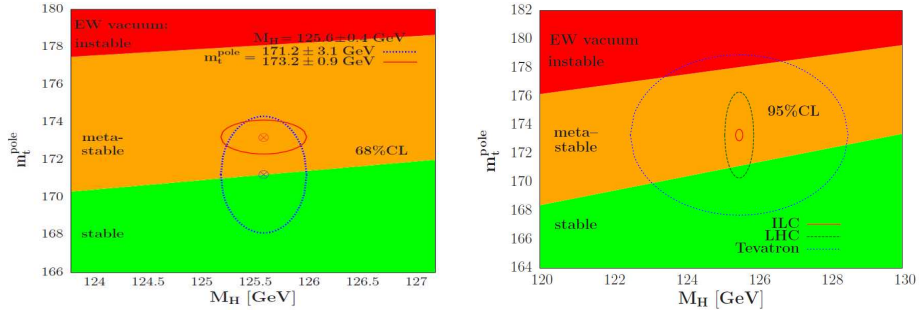


Figure 3.6: Figure from Ref. [70]. The ellipses in the $[M_H, m_t^{\text{pole}}]$ plane with the inputs $M_H = 125.6 \pm 0.4 \text{ GeV}$ and $\alpha_s = 0.1187$ are confronted with the areas in which the SM vacuum is absolutely stable, metastable and unstable up to the Planck scale. Left: the 1σ ellipse when m_t^{pole} is identified with the one measured at the Tevatron and with the mass $m_t = 171.2 \pm 3.1 \text{ GeV}$ extracted for the $t\bar{t}$ production cross section [72] is added to the 1σ ellipse when m_t^{pole} is identified with the Tevatron kinematical measurement. Right: the 1σ ellipses for the latest top-quark pole mass measurement in Tevatron and the expectations for LHC and ILC.

3.2 Current top-quark mass measurements

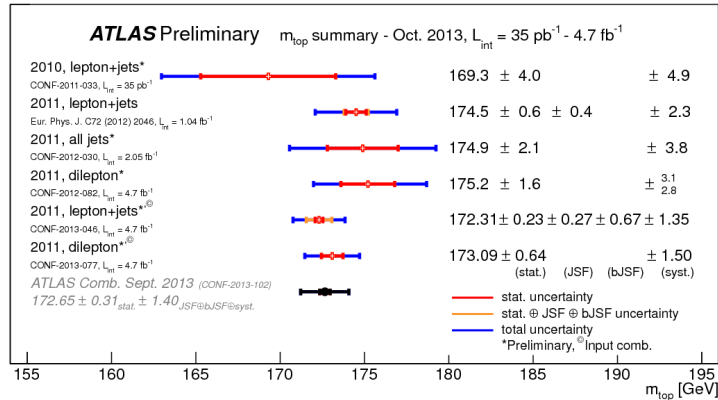
The top-quark mass values quoted in the Particle Data Group (PDG [25], see Figure 3.1) are: $M_t = 173.21 \pm 0.51 \pm 0.71$ GeV, $\overline{m}_t(m_t) = 160^{+5}_{-4}$ GeV and $m_t^{\text{pole}} = 176.7^{+4.0}_{-3.4}$ GeV. The first mass is a combination of direct measurements done by the Tevatron and the LHC. The second and third one correspond to the top-quark $\overline{\text{MS}}$ and pole mass scheme extracted from the total $t\bar{t}$ cross section. The two different approaches: direct measurements and top-quark mass extraction from cross section measurements are presented in the following subsections.

3.2.1 Direct measurements

The summary of latest results produced by the ATLAS and CMS collaborations for the direct measurements are presented in Figure 3.7. Combinations of the results obtained by different experiments are also quoted. To obtain most of the mentioned results, the mass is reconstructed from a kinematic fit of the decay products to a $t\bar{t}$ hypothesis. This is the case, for example, of the ATLAS most precise measurement which is based in a three-dimensional technique [73] that measures at the same time the kinematic top-quark mass, the hadronic W boson mass and the R_{lb} quantity defined as the ratio between the average transverse momentum of the b -tagged jets (jets identified as generated by a b -quark) and the average transverse momentum of the two jets of the W -boson hadronic decay. This measurement is performed for $t\bar{t}$ events decaying semileptonically. Measuring the W boson mass and the R_{lb} , the dependence on the uncertainties related to the jet energy calibration are largely reduced in comparison with other methods. The measured top-quark mass is $m_t = 172.31 \pm 1.35$ GeV. The CMS most precise measurement [74] is performed in a similar way, but implementing a two dimensional fit to the reconstructed top-quark and W boson masses. The result in this case is $m_t = 172.04 \pm 0.78$ GeV.

3.2.2 Top-quark mass extraction from inclusive cross section measurements

The top-quark mass is also inferred from its dependence in the inclusive $t\bar{t}$ cross section. The most precise top-quark mass determination from the measurement of cross sections is performed in Ref. [75] by comparing the measured cross section with QCD calculations at next-to-next-to-leading order (NNLO). Moreover, in this work, it has been proved that the measured cross section does not depend on the top-quark mass used in the Monte Carlo for the acceptance and background corrections. The measured top-quark mass is $m_t^{\text{pole}} = 172.9^{+2.5}_{-2.6}$ GeV.



CMS Preliminary

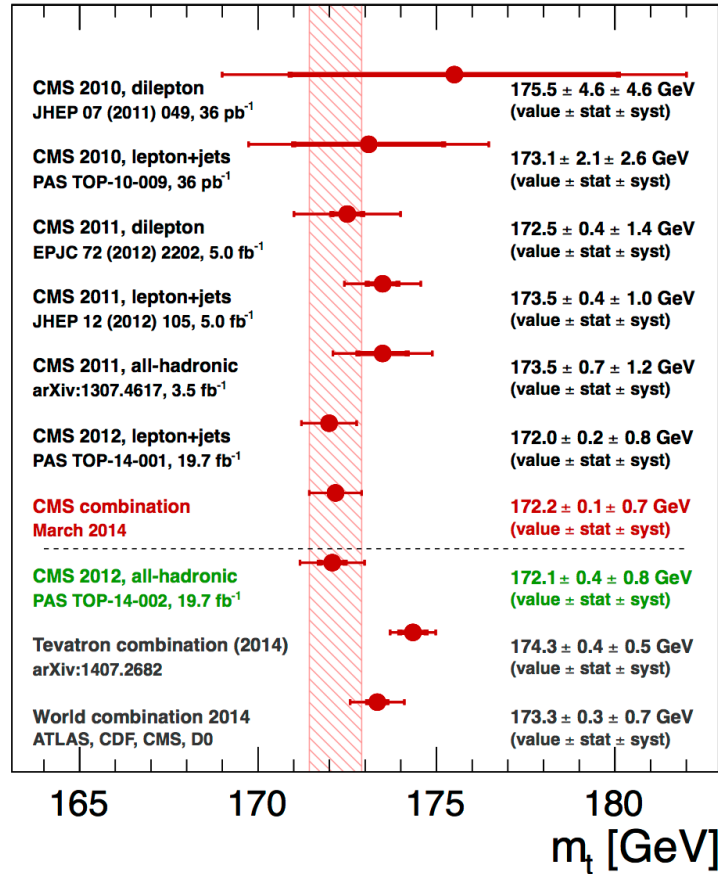


Figure 3.7: Upper figure: summary of the ATLAS direct m_t measurements. The results are compared with the 2013 ATLAS m_t combination. The JSF, bJSF contributions are statistical in nature and apply to analysis performing in-situ (top quark pair base) jet energy calibration procedures. Updated to September 2014. Lowermost figure: summary of direct top-quark mass measurements by CMS. The combination of CMS measurements is presented and compared with the combination of Tevatron measurements and with the world combination. Updated to July 2014.

3.3 Precise top-quark mass determination methods

As stated at the beginning of Section 3.1 the quark masses are not observables and they have to be studied as effective couplings of the underlying theory similarly to α_s : their values should be extracted from the measurement of hadronic observables which depend on such couplings, i.e. extract the α_s from the $\sigma_{i\bar{i}}$ measurement.

Most precise top-quark mass measurements at the moment are based on the direct determination from the kinematic reconstruction of the invariant mass of their decay products. In this case the top quark is studied in the same way as the free particles are, although the top-quark does not exist as a free particle (the top-quark is a color triplet) and this kinematic mass does not correspond to a well-defined renormalization scheme, leading to an uncertainty in its interpretation (the kinematic mass is reconstructed using non colored final state objects). In this case, the measured mass corresponds to the mass of the Monte Carlo used in the simulation, with a theoretical uncertainty Δm_t^{theory} :

$$m_t^{\text{pole}} = m_t^{MC} + \Delta m_t^{theory} \quad (3.8)$$

which has not been unambiguously calculated although it is estimated to be of the order of $\Delta m_t^{theory} \sim O(1)$ GeV (see, for example, references [5] and [6]).

As it can be followed from the discussion in the section above, and from the Figures 3.4, 3.5 and 3.6, a precise measurement of a well defined top-quark mass is crucial to understand the SM validity and to explore new theories. For that, a *proper* observable has to be defined, measured and, finally, compared with theoretical calculations. The basic requirements needed to define such an observable can be summarized in the following points:

- The observable \hat{O} should show a good sensitivity on the parameter to be measured (in this case the mass): $\Delta \hat{O} / \hat{O} \leftrightarrow \Delta m_t / m_t$;
- the observable has to be well defined (IR-safe) using a well defined mass scheme;
- it has to be theoretically calculable with small theoretical uncertainties from non-perturbative corrections;
- and, finally, it has to be experimentally accessible.

The most common mass schemes used in top-quark physics related calculations are the $\overline{\text{MS}}$ scheme and the pole mass scheme (see Section 2.1.1.1) The physics does not depend on the choice of the top-quark mass renormalization scheme even though it is known that the definition of the top-quark pole mass is affected by non perturbative QCD corrections which have been estimated to be of the order of Λ_{QCD} [76]. Moreover, in calculations at any fixed order in perturbation theory, a remaining residual dependence on the renormalization scale appears. In the $\overline{\text{MS}}$ scheme the μ_R dependence of the mass can be used to absorb certain logarithmically enhanced corrections and to resum them to all orders that lead to improvement in some calculations. This

happens, for example, in the calculation of the inclusive $t\bar{t}$ cross section which shows better convergence when the $\overline{\text{MS}}$ scheme is chosen.

An example of a QCD observable that can be used to determine the top-quark mass is the inclusive $t\bar{t}$ cross section. The extraction of the top-quark mass from its dependence in top-quark pair production is done in an unambiguously defined mass scheme. However, this observable show larger uncertainties on the mass determination as a consequence of the weak sensitivity of the cross section on the top-quark mass: $\Delta\sigma_{t\bar{t}}/\sigma_{t\bar{t}} \sim 4\%\Delta m/m$ which means that with an accuracy of 4% on the cross section measurement or the cross section calculation the determination of the mass accurate to $\sim 1\%$ ($\sim 1,7$ GeV).

Given the physical relevance of top-quark mass measurements it is important to employ alternative methods with similar or even better accuracy than the methods mentioned above. In the following sections we will present a novel method where the pole top-quark mass is extracted from a measurement of the $t\bar{t} + 1$ -jet differential cross section. This observable shares the rigorous interpretation of the mass extracted from the inclusive $t\bar{t}$ cross section, but its sensitivity is enhanced when looking at certain phase space regions where the mass dependence is not diluted. This method has been applied to real data taken by the ATLAS detector. The details of the experimental procedure and the results can be found in Ref. [12] and, more extensively, in Chapter 5.

3.4 Top-quark mass measurement from jet rates

In this chapter, a new method to measure the top-quark mass from the measurement of jet rates at LHC is proposed. The dependence of QCD radiation processes on the mass of the emitting quark is exploited. This can be seen, for example, in $e^+e^- \rightarrow Z^0 \rightarrow b\bar{b}g$ topologies which are sensitive to the b -quark mass [77, 78, 79]. This sensitivity was exploited to determine the b -quark mass and the first measurement of its running, $\bar{m}_b(M_Z)$ [80]. Two examples of leading order Feynman diagrams for this kind of processes can be seen in Figure 3.8. The mass dependence can be qualitatively described as:

$$\sigma_{q\bar{q}g} \propto A(\alpha_s, \sqrt{s}) + B(\alpha_s, \sqrt{s}, m_q) \frac{m_q^2}{s} + \dots \quad (3.9)$$

where A, B, \dots can be calculated using perturbation theory. The emission of gluons does not only depend on the α_s value but also on the mass of the emitting quark: apart of reducing the available phase space for the gluon emission, it has the effect of reducing the QCD radiation since in general the gluon emission from quarks get suppressed for heavier quarks. It is important to notice that in lepton-lepton collisions the interaction energy (\sqrt{s}) is fixed.

The method present in this chapter is based in similar measurements for $t\bar{t} + 1$ -jet final states produced in pp collisions at the LHC. It exploits the fact that the jet rates can be measured at different energies of interaction since at the LHC the energy of the hard interaction is not fixed as it depends on the distribution of the energy

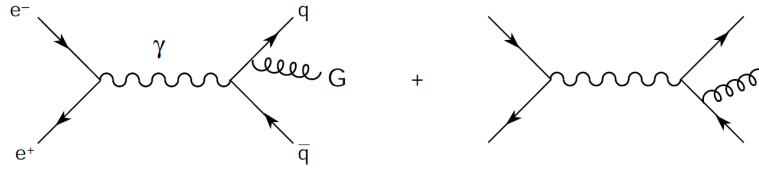


Figure 3.8: Feynman diagrams for the real gluon emission corrections to $e^+e^- \rightarrow q\bar{q}$ which correspond to the Born (LO) Feynman diagrams of $e^+e^- \rightarrow q\bar{q}g$

among the proton constituents. This allows to perform a scan of different regions of the phase space to find a region where the mass dependence would be enhanced through threshold effects.

In the next paragraphs the main features of the predictions at NLO for $t\bar{t} + 1$ -jet topologies are presented. The $t\bar{t} + 1$ -jet calculations fulfill the basic requirements needed to make good predictions: they are available at NLO and the loop-corrections are small; the uncertainties associated to uncalculated higher orders are small; the top-quark mass scheme is defined unambiguously. Moreover a large rate of $t\bar{t}$ events contains a hard- p_T extra jet ($\sim 30\%$ - depending of the required minimum value required for the p_T).

The study of this new observable to measure the top-quark mass together with the calculations of $t\bar{t} + 1$ -jet topologies including NLO QCD corrections for the LHC collider for 7 TeV collisions were presented in Ref. [11].

3.4.1 Next-to-leading order calculations of $t\bar{t} + 1$ -jet topologies

The calculations presented here and in Ref. [11] are based on the previous works of Refs. [8, 9] where predictions for the Tevatron collider and the LHC collider working at 14 TeV were calculated. A representative set of Feynman diagrams used for the $t\bar{t} + 1$ -jet cross section calculation at NLO can be seen in Figure 3.11 and Figure 3.10. The studies presented in the references mentioned above show that the NLO QCD corrections lead to a significant reduction of the scale (renormalization/factorization) uncertainty compared with the LO predictions and that the calculations show an apparent convergence of the perturbative expansion. Moreover, the one-loop corrections change the $t\bar{t} + 1$ -jet cross section only in 10% range (depending on the p_T requirement for the extra jet).

The theoretical calculations performed in Ref. [11] include NLO corrections and use the pole mass scheme. Other schemes for the top-quark mass could have been chosen, such as for instance the \overline{MS} mass.

There is no principle telling us what is the most appropriate scale that should be used in the calculations. The scale is, naively, chosen to avoid all the large logarithmically divergences. In the case of $t\bar{t}$ production in hadron colliders, the usual choice is related to the m_t^{pole} . For the case of $t\bar{t} + 1$ -jet calculations, as it is shown in Fig. 3.9, the cross section calculation evaluated at NLO presents a *plateau* around $\mu = m_t^{\text{pole}}$ which motivates to use it to calculate the central value of the cross section. The same proce-

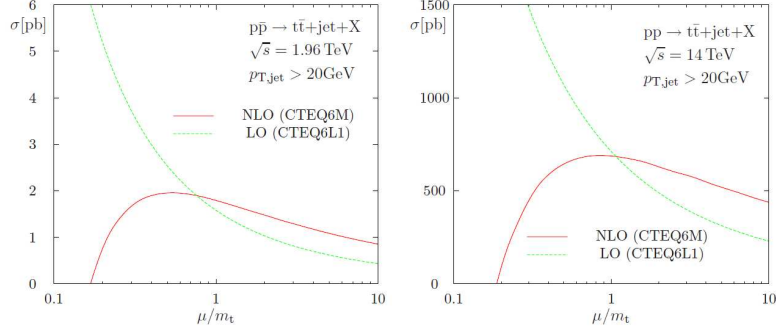


Figure 3.9: Scale dependence at LO (green) and NLO (red). The first plot shows the cross section for $t\bar{t} + 1\text{-jet}$ at the Tevatron, and the second the same for the LHC (14 TeV collisions). See Ref. [81] for more detail.

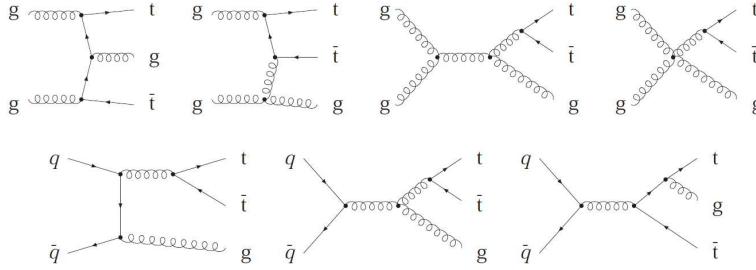


Figure 3.10: Representative sets of LO diagrams for gg fusion and $q\bar{q}$ annihilation in hadronic $t\bar{t} + 1\text{-jet}$ production. Figure taken from Ref. [9].

ture is usually followed for $t\bar{t}$ production calculations. Therefore, the renormalization (μ_R) and factorization (μ_F) scales have been set to $\mu = \mu_R = \mu_F = m_t^{\text{pole}}$.

The theoretical uncertainty due to the missing higher order terms is evaluated following the usual prescription of varying the renormalization and factorization scales up and down by a factor of two with respect to the central value, that is $m_t^{\text{pole}}/2 \leq \mu \leq 2m_t^{\text{pole}}$. The variation of both scales independently (avoiding the extremal combinations where μ_R/μ_F is larger than 2 or smaller than 1/2) introduce remarkable small variations (typically below 10%) according to studies performed in Ref. [10] for the $t\bar{t} + 1\text{-jet}$ process at NLO.

In the study of Ref. [11] the top quarks enter the analysis as stable particles and the extra jet is defined by merging the additional partons using the anti- k_t jet reconstruction algorithm [82, 83]. The radius parameter R of the anti- k_t jet reconstruction algorithm was set to 0.4. To render the cross section infrared safe the jet is required to have a minimum transverse momentum of 50 GeV and a pseudorapidity $|\eta| < 2.5$. These values are introduced ad-hoc and are considered acceptable to evaluate the potential of the method and to guarantee the stability of the calculation. In fact, the calculation is stable and shows good convergence for transverse momentum above 20 GeV. No further optimization studies were pursued in this respect.

The NLO calculation assumes the top quarks on-shell and considers that the pos-

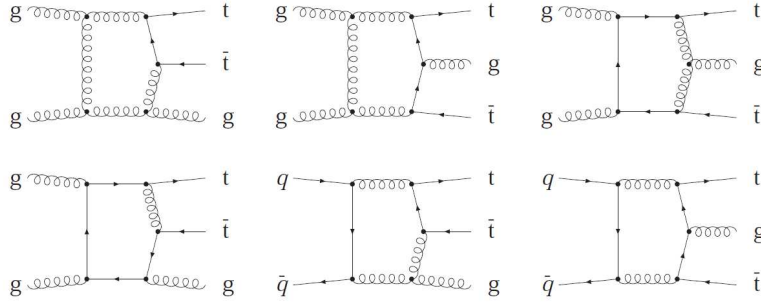


Figure 3.11: Representative sets of pentagon diagrams (virtual corrections) for gg fusion and $q\bar{q}$ annihilation in hadronic $t\bar{t} + 1$ -jet production at NLO QCD. Figure from Ref. [9]

m_t^{pole} [GeV]	$\sigma_{t\bar{t}+1\text{-jet}}$ [pb]	
	$p_T(\text{jet}) > 50 \text{ GeV}, \eta(\text{jet}) < 2.5$	
	LO	NLO
160	66.727(5)	60.04(8)
165	57.615(4)	52.25(9)
170	49.910(3) ⁺³⁰ ₋₁₇	45.45(6) ⁺¹ ₋₆
172.5	46.508(3) ⁺²⁸ ₋₁₅	42.37(6) ⁺¹ ₋₆
175	45.372(3)	39.46(6)
180	37.800(2)	34.73(5)

Table 3.1: The $t\bar{t} + 1\text{-jet} + X$ cross section using LO and NLO calculations [8, 9] for proton-proton collisions at 7 TeV and for different m_t^{pole} values. Jets are defined using the anti-kt algorithm [82] with $R=0.4$ as implemented in the FASTJET package [83]. The additional jet is required to have $p_T > 50$ GeV and $|\eta| < 2.5$. The uncertainty due to the limited statistics of the numerical calculation is indicated in parenthesis affecting the last digit. The scale uncertainty is also shown for some top-quark mass values. The CTEQ6.6 [84] (CT09MC1 [85]) PDF set has been used to obtain the NLO (LO) results. The subscript denotes the shift of the cross section for $\mu = 2m_t^{\text{pole}}$ and, likewise, the superscript for $\mu = m_t^{\text{pole}}/2$. Table from Ref. [11]

sible effects due to the radiation from top-quark decays and virtual corrections in the decay are small with respect to the overall theoretical error. As a matter of fact, QCD corrections in the decay do not affect the mass renormalization of the top-quark in the order which is being worked out, as this is purely determined from the QCD self energy corrections of the top propagator (included in the calculation). Furthermore recent calculations in Ref. [86, 87] have computed NLO-QCD corrections to the total top cross section assuming the top quarks off-shell and have found that for most of inclusive enough quantities the results in the on-shell approximation are reliable and off-shell effects turn out to be very small.

The cross sections evaluated for pp collisions at 7 TeV are given in Tab. 3.1. The default PDF set used is the CTEQ6.6 [84] with its correspondent $\alpha_s(M_z) = 0.118$ value. Both, PDF and α_s , are used consistently to evaluate the LO contributions

m_t^{pole} [GeV]	$\sigma_{t\bar{t}+1\text{-jet}}$ (pb) $p_T(\text{jet}) > 25 \text{ GeV}, \eta(\text{jet}) < 2.5$	
	LO	NLO
170	$91.827(8)_{-31}^{+53}$	$77.7(1)_{-9}^{-1}$
172.5	$85.39(1)_{-29}^{+50}$	$72.43(6)_{-9}^{-2}$

Table 3.2: Similar to Tab. 3.1 but for a p_T cut of 25 GeV in difference to 50 GeV used in Tab. 3.1. Table from Ref. [11]

entering the NLO predictions. This PDF set does not include a LO parton distribution function. Instead, the CT09MC1¹ [85] has been used (and its correspondent α_s value) for the LO calculations. For all the masses, negative corrections of about 10% have been found. The scale uncertainty is significantly reduced when comparing NLO and LO calculations. For completeness, the same calculations have been performed with a softer requirement for the p_T of the additional jet. The results, for a p_T cut of 25 GeV instead of 50 GeV are shown in Tab. 3.2 for two top-quark mass values. In this case, the NLO terms introduce a negative correction of about 17%.

The uncertainties originating from the PDFs have been estimated by comparing the results obtained with two different PDF sets: the CTEQ6.6 and the MSTW2008nlo90cl [41]. For a top-quark mass of $m_t^{\text{pole}} = 170$ GeV a difference of about 10 percent between both predictions:

$$\sigma_{t\bar{t}+1\text{-jet}}^{\text{NLO, MSTW08}} = 49.21 \text{ pb}. \quad (3.10)$$

These predictions have been performed with fixed-order calculations. The matching of these NLO calculations with parton shower algorithms [10, 88] have been used to simulate a more realistic scenario, closer to what is observed in the experiment. The $t\bar{t} + 1\text{-jet}$ cross section calculation have been repeated with two different calculations performed using POWHEG and matched with PYTHIA8.150 -NLO+PS-. The results are shown in Tab. 3.3 for $m_t^{\text{pole}} = 170$ GeV. In this table, two different POWHEG calculations are shown: the inclusive $t\bar{t}$ @NLO+PS and the $t\bar{t} + 1\text{-jet}$ @NLO+PS. In the inclusive $t\bar{t}$ production, the additional jet is included in NLO accuracy through the real corrections. The addition of the parton shower to this calculation offers a reasonably good description of $t\bar{t} + 1\text{-jet}$ topologies. Tab. 3.3 shows that the results obtained with both calculations ($t\bar{t}$ and $t\bar{t} + 1\text{-jet}$) are in perfect agreement with the fixed order calculations (Tables 3.1 and 3.2) when the parton shower is added. For completeness, the predicted cross section before the addition of the parton shower is included in the table.

To further investigate the reliability of the theoretical predictions, a set of differential distributions obtained within different approaches has been compared. This is shown in Fig. 3.12. Distributions obtained with the same NLO calculations implemented in POWHEG [10] and that includes the parton shower correction performed by PYTHIA8 (NLO+PS accuracy) with those results obtained in the fixed order parton

¹The choice of this PDF set was recommended by the CTEQ collaboration in a private communication with Pavel Nadolsky

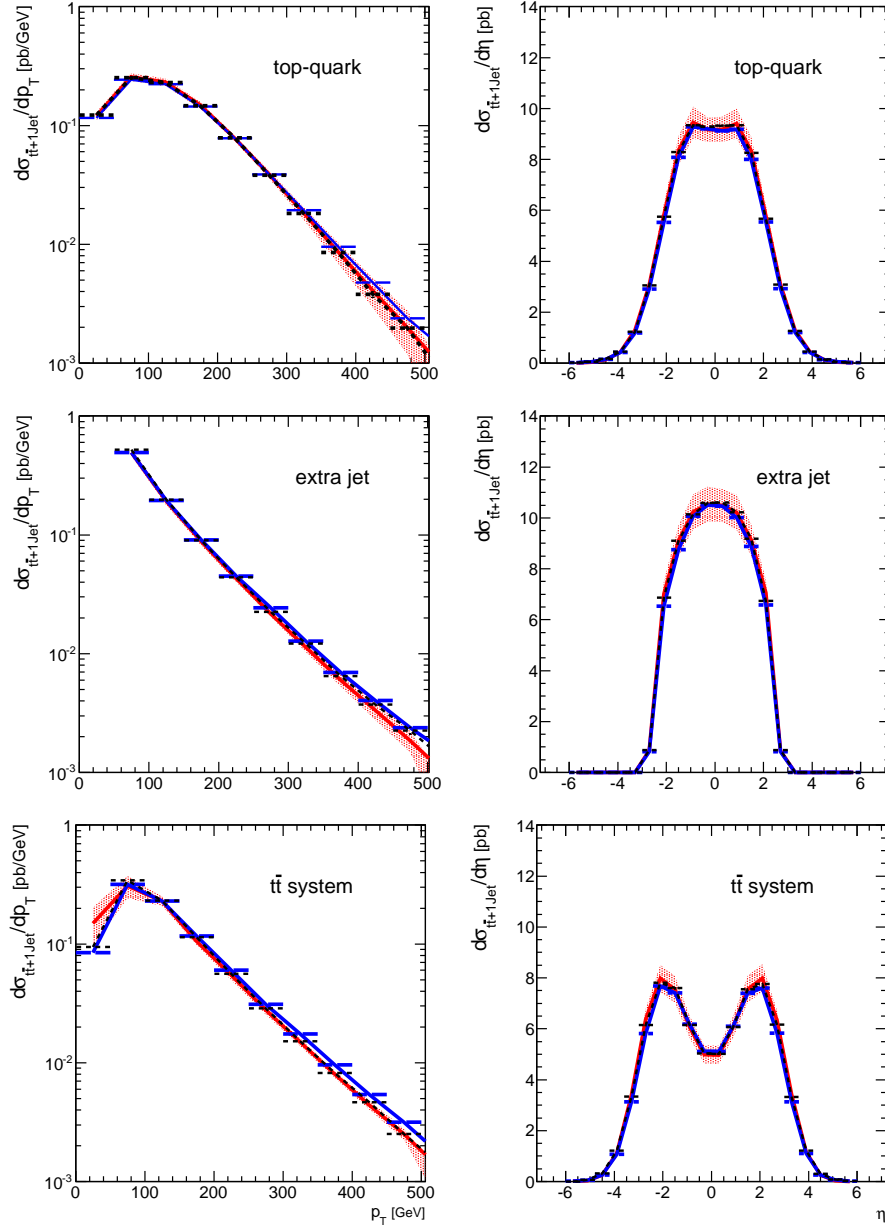


Figure 3.12: Comparison of different theoretical approaches to describe the $t\bar{t} + 1$ -jet production applied to various p_T and η distributions. The red band corresponds to the $t\bar{t} + 1$ -jet NLO at fixed order including the scale uncertainty. The continuous-blue and dotted-black line show the results obtained using POWHEG with $t\bar{t}$ and $t\bar{t} + 1$ -jet NLO calculations, respectively, and matched with the PYTHIA8 parton shower. Figures from Ref. [11].

$m_t^{\text{pole}} = 170 \text{ GeV}$		
	$\sigma_{t\bar{t}+1\text{-jet}} [\text{pb}]$	
$t\bar{t}$	without additional PS	50.42(6)
NLO	+PS by PYTHIA8	45.61(8)
$t\bar{t} + 1\text{-jet}$	without additional PS	48.8(2)
NLO	+PS by PYTHIA8	45.1(1)
$m_t^{\text{pole}} = 172.5 \text{ GeV}$		
	$\sigma_{t\bar{t}+1\text{-jet}} [\text{pb}]$	
$t\bar{t}$	without additional PS	47.2(1)
NLO	+PS by PYTHIA8	43.2(5)
$t\bar{t} + 1\text{-jet}$	without additional PS	44.9(5)
NLO	+PS by PYTHIA8	43.0(5)

Table 3.3: The $t\bar{t} + 1\text{-jet} + X$ cross section for proton-proton collisions at 7 TeV obtained with POWHEG with and without a PYTHIA8 parton shower matching for $m_t^{\text{pole}} = 170, 172.5 \text{ GeV}$. The setup is the same as in Tab. 3.1. Table from Ref. [11]

level calculation (NLO accuracy) are compared. In general, a good agreement for all the distributions is observed. Similar studies have been performed in Ref. [10] where a broader study of phenomenological studies for LHC and Tevatron are presented.

Only at large transverse momentum minor differences are observed where the $t\bar{t}$ @NLO+PS slightly disagrees with the $t\bar{t} + 1\text{-jet}$ @NLO at fixed order and @NLO+PS since the hard emission in $t\bar{t}$ @NLO+PS is only treated at LO not including double real emission processes: the additional jet activity beyond this first emissions is due to the parton shower which prefers soft and collinear emissions. In the $t\bar{t} + 1\text{-jet}$ NLO and NLO+PS, the second real emission is already included in the hard matrix element. This second real emission may cluster with the first emission in a jet or may cluster in a second jet, contributing to reduce the transverse momentum at large p_T . Moreover, in this distribution, the value of α_s plays a role in the spectrum of the p_T since the second jet (in the $t\bar{t}$ @NLO+PS prediction) is entirely generated by the shower that typically has a $\alpha_s(p_T)$ factor associated to the emission. Instead, in the $t\bar{t} + 1\text{-jet}$ NLO and NLO+PS predictions, the second parton emission is computed in the hard matrix element with a fixed choice of the scale $\mu_r = m_t$ that results in a larger α_s value and thus an harder spectrum, for $p_T > m_t$. Some differences in the $p_T^{t\bar{t}}$ spectrum between the fixed-order calculation and the two NLO+PS implementations are observed for low values. This is expected and due to the fact that the parton shower approach resums logarithmically enhanced corrections to all orders. This effect does not appear in the p_T spectrum of the extra jet since a strong cut in the p_T has been required.

3.4.2 Theoretical definition and study of the \mathcal{R} observable

The theoretical description of the $t\bar{t} + 1\text{-jet}$ process at NLO accuracy in QCD is well under control, with small corrections and with small uncertainties associated to uncalculated higher orders. Moreover, these topologies are present in about $\sim 30\%$ of the inclusive $t\bar{t}$ events.

The sensitivity on the top-quark mass for the 'inclusive' $t\bar{t} + 1\text{-jet}$ cross section is similar to what has been observed for the inclusive top-quark pair production:

$$\frac{\Delta\sigma_{t\bar{t}+1\text{-jet}}}{\sigma_{t\bar{t}+1\text{-jet}}} \approx -5 \frac{\Delta m_t^{\text{pole}}}{m_t^{\text{pole}}}, \quad (3.11)$$

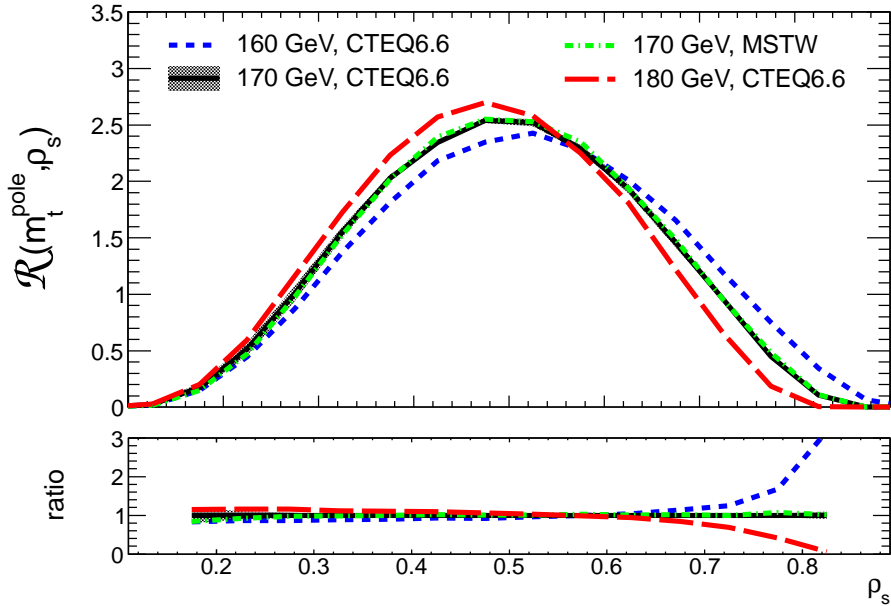


Figure 3.13: $\mathcal{R}(m_t^{\text{pole}}, \rho_s)$ calculated at NLO accuracy for different masses $m_t^{\text{pole}} = 160, 170$ and 180 GeV. For $m_t^{\text{pole}} = 170$ GeV the scale and PDF uncertainties evaluated as discussed in the text are shown. The ratio with respect to the result for $m_t^{\text{pole}} = 170$ GeV is shown in the lower plot. Figure from Ref. [11].

Therefore a measurement of the 'inclusive' $t\bar{t} + 1\text{-jet}$ cross section would not lead to any improvement compared with the methods that extract the top-quark mass from the measurement of the $t\bar{t}$ cross section. For that, the study of normalized differential distributions is proposed: due to the normalization many theoretical and experimental uncertainties cancel between the numerator and the denominator; looking into differential distributions allows to exploit specific regions of the phase space where the top-quark mass sensitivity is enhanced. For that the \mathcal{R} distribution is defined as the normalized $t\bar{t} + 1\text{-jet}$ cross section in pp collisions with respect to the inverse of the

invariant mass $\sqrt{s_{t\bar{t}j}}$ of the $t\bar{t} + 1$ -jet system:

$$\mathcal{R}(m_t^{\text{pole}}, \rho_s) = \frac{1}{\sigma_{t\bar{t}+1\text{-jet}}} \frac{d\sigma_{t\bar{t}+1\text{-jet}}}{d\rho_s}(m_t^{\text{pole}}, \rho_s), \quad (3.12)$$

where ρ_s is defined as

$$\rho_s = \frac{2m_0}{\sqrt{s_{t\bar{t}j}}}. \quad (3.13)$$

with m_0 an arbitrary constant of the order of the top-quark mass ($m_0 = 170$ GeV from now on).

Hereafter in the text the expression \mathcal{R} will be used to refer to the observable and, unless it would be explicitly specified another value, a $p_T > 50$ GeV is required to define the \mathcal{R} observable.

The behavior and main features of \mathcal{R} are shown in Fig. 3.13 where the \mathcal{R} distribution evaluated at fixed NLO is shown for three different masses, $m_t^{\text{pole}} = 160, 170$ and 180 GeV. For the central mass, $m_t^{\text{pole}} = 170$ GeV, the scale uncertainties have been evaluated, symmetrized and included in the figure (the black band). Furthermore, two different PDFs sets have been used as input for the calculation (CTEQ6.6 and MSTW2008NLO90cl). For large values of ρ_s (corresponding to the smallest values of $\sqrt{s_{t\bar{t}j}}$) the production of heavier top-quark masses is suppressed compared to lighter masses. This region is where the sensitivity to the mass is largest. As the curves are normalized to unit area the curves cross. This happens around ρ_s slightly below $\rho_s \sim 0.6$. In this interval the distribution loses sensitivity to the top-quark mass. For large energies $\sqrt{s_{t\bar{t}j}}$ ($\rho_s \rightarrow 0$) some sensitivity still remains but the mass dependence becomes small.

To quantify the sensitivity to the top quark mass the following sensitivity, \mathcal{S} , is defined:

$$\mathcal{S}(\rho_s) = \sum_{\Delta=\pm 5-10 \text{ GeV}} \frac{|\mathcal{R}(170 \text{ GeV}, \rho_s) - \mathcal{R}(170 \text{ GeV} + \Delta, \rho_s)|}{2|\Delta|\mathcal{R}(170 \text{ GeV}, \rho_s)}. \quad (3.14)$$

The result for \mathcal{S} is shown in Fig. 3.14 and compared with the equivalent \mathcal{S} defined for $t\bar{t}$ events (without the additional jet, where the definition $\rho = 2m_0/\sqrt{s_{t\bar{t}}}$ is used). At the y -axis drawn at the right side of the figure, the $m_t^{\text{pole}} \times \mathcal{S}$ is shown which is the proportionality factor relating the relative change in the top-quark mass to the relative change in \mathcal{R} :

$$\left| \frac{\Delta \mathcal{R}}{\mathcal{R}} \right| \approx \left(m_t^{\text{pole}} \mathcal{S} \right) \times \left| \frac{\Delta m_t^{\text{pole}}}{m_t^{\text{pole}}} \right|. \quad (3.15)$$

As can be seen in Fig. 3.14 values of $m_t^{\text{pole}} \times \mathcal{S}$ up to 25 are reached around ρ

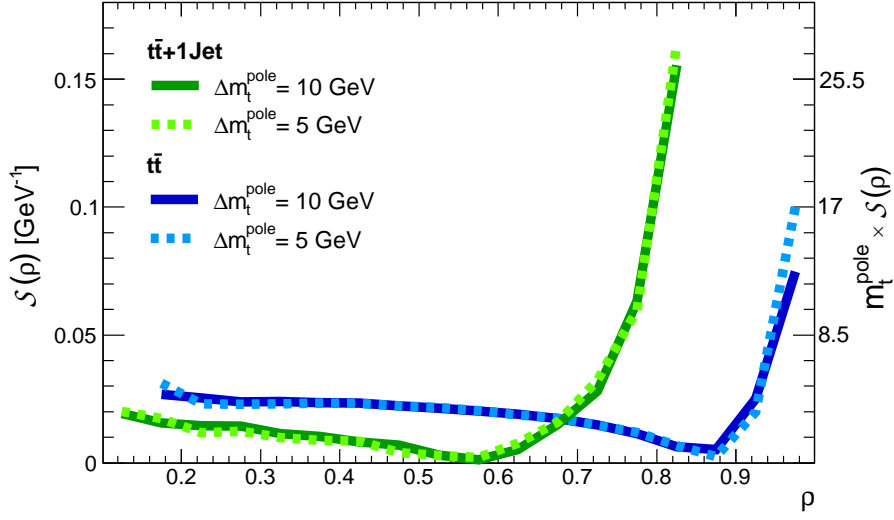


Figure 3.14: The sensitivity $\mathcal{S}(\rho_s)$ of \mathcal{R} with respect to the top-quark mass as defined in Eq. (3.14). Figure from Ref. [11].

equal 0.8. In other words a one per cent change of the mass translates into a 25 per cent change of the observable \mathcal{R} in this region. The observable is thus more sensitive than the inclusive cross section ($\frac{\Delta\sigma_{t\bar{t}}}{\sigma_{t\bar{t}}} \approx -4 \times \frac{\Delta m_t^{\text{pole}}}{m_t^{\text{pole}}}$). However small bin sizes are needed to fully profit from this fact. Comparing with the $t\bar{t}$ case, only in the extreme threshold region a similar sensitivity—though lower—can be reached very near of the threshold region. In this region, beyond perturbative corrections are required to resum threshold effects and soft gluon emission. Moreover, this ρ region of the phase space corresponds to a small window of the $s_{t\bar{t}}$ phase space: $\Delta\rho = (1.0 - 0.9) \rightarrow \sim 40$ GeV which is ~ 5 times smaller than the high sensitivity region for \mathcal{R} . The sum of all these arguments indicate that the \mathcal{R} observable using $t\bar{t} + 1$ -jet events is better suited to measure the top-quark mass than its equivalent distribution in $t\bar{t}$ final states.

Note that the evaluation of the sensitivity relies on the assumption of a nearly linear top-quark mass dependence. To cross check this assumption two different step sizes in Eq. (3.14) (5 and 10 GeV) are used in Fig. 3.14.

The differences between the various theoretical calculations including leading order (LO) versus next-to-leading order (NLO) and the effect of adding the parton shower was also investigated in Ref. [11] and more extensively here.

The size of the NLO corrections has been studied by comparing fixed order calculations. As it has been discussed before, the NLO corrections to the $t\bar{t} + 1$ -jet cross section are small, moreover, they become smaller when increasing the p_T requirement of the additional jet. This is shown in Tables 3.1 and 3.2. For $p_T \geq 25$ GeV, the NLO corrections are $\sim 17\%$, while for $p_T \geq 50$ GeV this factor reduces to $\sim 9\%$. A similar study has been performed but using as target the \mathcal{R} distribution instead of the 'inclusive' $t\bar{t} + 1$ -jet cross section. The difference in the value of the top-quark pole mass needed by a LO calculation to reproduce the NLO distribution is calculated. This

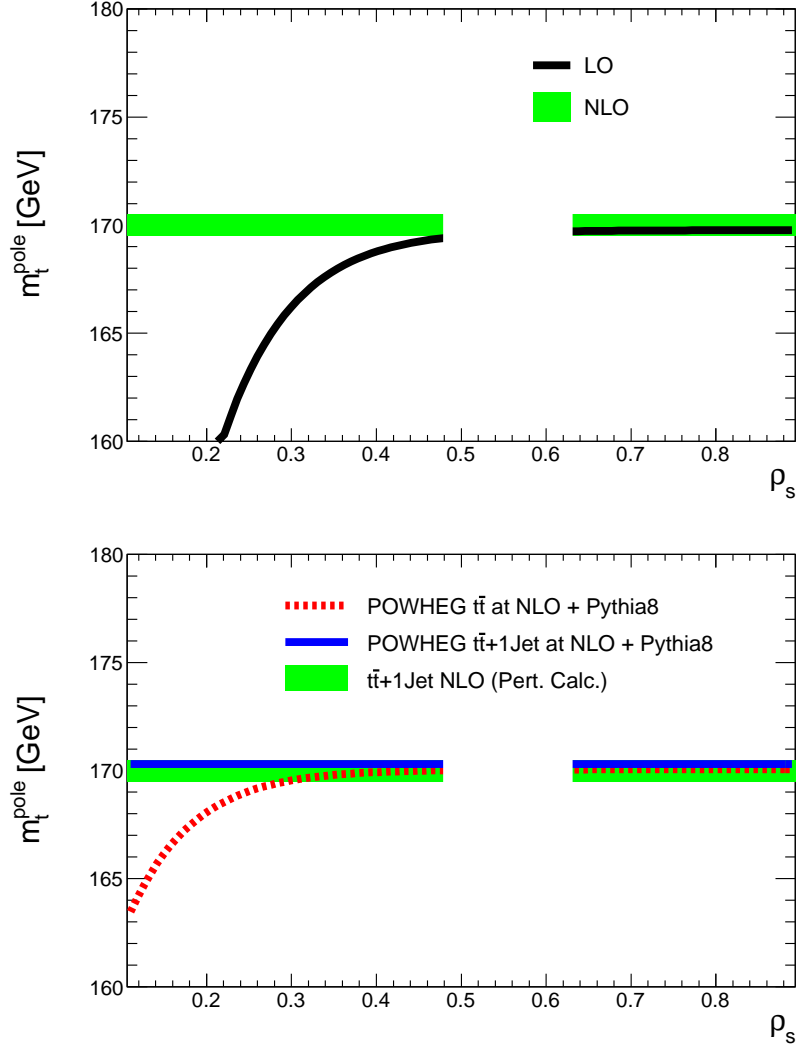


Figure 3.15: Uppermost plot: the top-quark mass m_t^{pole} as obtained from a $t\bar{t} + 1\text{-jet}$ @LO calculation fit to \mathcal{R} calculated in NLO accuracy (black line). Lowermost plot: the top-quark mass m_t^{pole} as obtained from a $t\bar{t}$ @NLO+PS and $t\bar{t} + 1\text{-jet}$ @NLO+PS fit to \mathcal{R} calculated in NLO accuracy (dashed-red and blue lines correspondingly). In both figures, the input value of $m_t^{\text{pole}} = 170 \text{ GeV}$ together with a variation of $\pm 0.5 \text{ GeV}$ is shown as green band. Figures from Ref. [11]

is shown in Fig. 3.15 where the dependence of \mathcal{R} with respect to the top-quark mass was calculated by constructing a grid with fixed values for m_t^{pole} (160 GeV, 170 GeV and 180 GeV) and assuming a linear dependence between them. Using this grid a fit to the reference \mathcal{R} distribution ($t\bar{t} + 1\text{-jet}$ @NLO calculation with $m_t^{\text{pole}} = 170 \text{ GeV}$) is performed. It is found that using the LO calculation as our theoretical prediction, we would measure a lower ($\sim 0.5 \text{ GeV}$) top-quark pole mass in the most sensitive region.

The effect of adding the parton shower was studied in a similar way, by doing

a fit to the reference \mathcal{R} distribution but using two different calculations as underlying theory ($t\bar{t} + 1\text{-jet}$ @LO+PS versus $t\bar{t} + 1\text{-jet}$ @NLO+PS). That was done using the calculations detailed in section 3.4.1 (POWHEG matched with PYTHIA8). A difference of ~ 0.3 GeV was computed when comparing $t\bar{t} + 1\text{-jet}$ @NLO versus $t\bar{t} + 1\text{-jet}$ @NLO+PS to estimate the impact of incorporating the parton shower in the description. This difference is contained by the band that form the scale uncertainty which was estimated to be of ~ 0.6 GeV in the most sensitive interval of p_s . In this context the predictions of $t\bar{t}$ @NLO and $t\bar{t} + 1\text{-jet}$ @LO were considered equivalent as the hard emission in $t\bar{t}$ @NLO is only treated at LO.

New studies have been performed after the publication of Ref. [11]. In this studies three different calculations of the \mathcal{R} observable are compared, all three including the parton shower. In this case the reference \mathcal{R} -distribution is computed using the $t\bar{t} + 1\text{-jet}$ @NLO+PS calculation and $m_t^{\text{pole}} = 170$ GeV. Three different calculations, for five masses from $m_t^{\text{pole}} = 170$ to $m_t^{\text{pole}} = 180$ GeV separated by intervals of $\Delta m_t^{\text{pole}} = 2.5$ GeV, were used to define the grid to fit to the mentioned reference \mathcal{R} distribution. Furthermore, three different choices of the p_T requirement for the additional jet are used. These calculations are the $t\bar{t} + 1\text{-jet}$ @NLO+PS itself and $t\bar{t}$ @NLO+PS with two different choices for the renormalization/factorization scales: the default fixed scale $\mu = m_t$ that we were using and a dynamic scale $\mu = \sqrt{m_t^2 + p_{T,t}^2}$. The latter is used in ATLAS MC simulations. The results are presented in Fig. 3.16. A lower mass value is needed in the $t\bar{t}$ @NLO+PS calculation to reproduce the distribution from the $t\bar{t} + 1\text{-jet}$ @NLO+PS calculation. This difference is smaller as the p_T cut on the extra jet increases. Finally, the difference is reduced when employing a dynamical scale in the $t\bar{t}$ @NLO+PS calculation.

3.5 Conclusions

High precision top-quark mass measurements are fundamental not only by its importance as fundamental parameter but to test the validity of the SM. The most precise methods are based on the direct determination from the kinematic reconstruction of the invariant mass of top-quark decay products reach precisions of $\Delta m_t^{\text{pole}} \sim 1$ GeV which are very similar to the uncertainty which is associated to its interpretation. Furthermore, new observables are needed to measure the top-quark mass with high experimental and theoretical precision.

A new observable is proposed, called \mathcal{R} , based on the measurement of the normalized and differential $t\bar{t} + 1\text{-jet}$ cross section. The \mathcal{R} observable is thus found to fulfill the following requirements:

- it is infrared safe;
- the NLO corrections with respect to the LO calculation are relatively small;
- it has a good sensitivity on the mass as shown in Fig. 3.14 for LHC 7 TeV conditions;

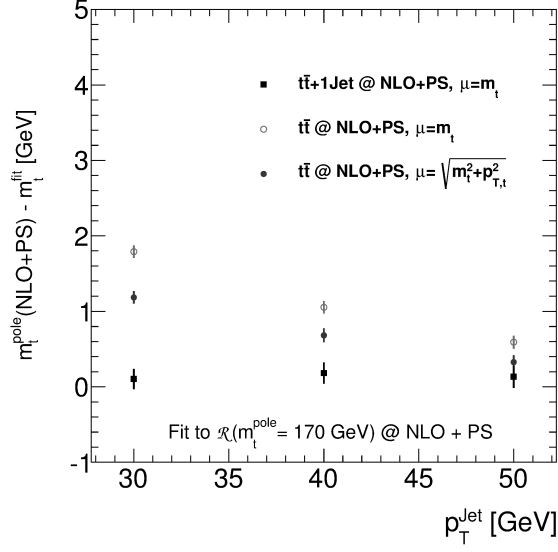


Figure 3.16: Difference of the extracted mass values obtained when fitting the \mathcal{R} -distribution by the three theoretical approaches discussed in the text. This difference is expressed as a function of the minimum p_T required for the extra jet. The reference calculation corresponds to $t\bar{t} + 1\text{-jet}$ @NLO+PS and the value for m_t^{pole} is 170 GeV. The black square points display this difference for the $t\bar{t} + 1\text{-jet}$ @NLO +PS -the reference distribution-; the red open circles show it for the $t\bar{t}$ @NLO+PS when using a fixed scale $\mu = m_t$ and the blue points when the scale is dynamic $\mu = \sqrt{m_t^2 + p_{T,t}^2}$. The error bars include the statistical and systematic uncertainties of the fit procedure as described in Chapter 5.

- the theoretical errors are reasonably small, i.e., dependence on Parton Density Function (PDF) and the renormalization and factorization scales;

A study of the experimental viability using public Monte Carlo tools was presented in Ref. [11] showing that the impact on the top-quark mass measurement would be $\Delta m_t^{\text{pole}} \sim 1$ GeV. This estimation is not presented in this thesis since a more complete study that includes the m_t^{pole} determination from the \mathcal{R} distribution measured using real data taken by the ATLAS experiment at LHC is presented in Chapter 5.

4

The ATLAS detector at the Large Hadron Collider (LHC)

The Large Hadron Collider (LHC) is the largest particle collider in the world. It collides protons and ions at unprecedented energies of several TeV. It is placed in Geneva (Switzerland) and it includes seven experiments studying the produced collisions. One of them is the ATLAS (A Toroidal Large ApparatuS) detector, which is a general purpose experiment designed to discover the Higgs, study top-quark physics and other SM physics related studies and to perform searches of new physics beyond the Standard Model.

In this chapter, the experimental apparatus used in this analysis is presented. First, in Section 4.1 a brief description of the LHC, is done including a short overview of the main detectors placed in the trajectory of the beams LHC and a short description of the Worldwide LHC Computing Grid (WLCG). Finally, in Section 4.2 the ATLAS detector is presented since the analysis presented in this thesis is based on the data collected by this experiment during the year 2011.

4.1 Large Hadron Collider

The LHC is a particle accelerator which operates at CERN (European Laboratory for Particle Physics) and collides protons (or Pb ions) at high energy. It is built in the former tunnel of the LEP (Large Electron Positron) collider: a 27 km circumference tunnel situated about 100 m underground between Switzerland and France(see Figure 4.1). The LEP was to collide fundamental fermions (electrons and positrons) reaching energies of $\sqrt{s} = 209$ GeV in the year 2000. The LHC collides protons at unprecedented center-of-mass energies (7 TeV during 2011 and 8 TeV during 2012) reaching integrated luminosities of 4.6 fb^{-1} and 20.3 fb^{-1} (during the 2011 and 2012

respectively)¹

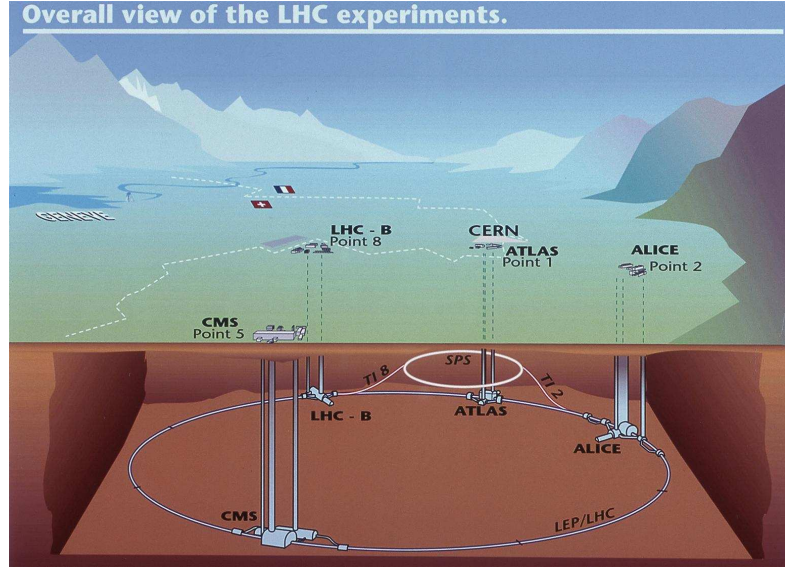


Figure 4.1: Representation of the LHC ring with the main detectors and all its services. Figure from the CERN public webpages [90].

To bend the several TeV proton (or Pb ions) beams around the circumference of 27 km a set of 1232 superconducting dipole magnets are used in the LHC ring. These magnets use twin bore magnets formed by two sets of coils and beam channels within the same mechanic structure and cryostat, since the two beams are composed by hadrons with the same electrical charge. To obtain the required accelerating power the coils are made of niobidium-titanium (NbTi) which allows to reach the superconductivity regime when they are cooled down with super-fluid Helium to 1.9 K. Besides the dipoles, a large number of quadrupolar (392) magnets for beam focusing and beam corrections and sextupole, octupole and decapole magnets for compensating the systematic non-linearities are needed. Besides the LHC magnets, all the CERN accelerator complex is needed to produce, accelerate and contain the particles in the final beams. This is shown in Fig. 4.2. The accelerator complex at CERN is a succession of machines that accelerate particles to increasingly higher energies. Each machine boosts the energy of a beam of particles, before injecting the beam into the next machine in the sequence. In the LHC, the last element in this chain, particle

¹The luminosity \mathcal{L} is an accelerator parameter that measures the number of interactions per cross section and time. Assuming a Gaussian transverse particle bunch profile, the \mathcal{L} is defined as:

$$\mathcal{L} = \frac{1}{4\pi} \frac{N_1 N_2}{\sigma_x \sigma_y} f N_b$$

where $N_{1,2}$ are the number of particles in the two (1,2) colliding beams respectively, f is the bunch crossing frequency, N_b is the number of bunches and $\sigma_{x,y}$ are the Gaussian widths in the horizontal and vertical plane of the bunch respectively. The integrated luminosity corresponds to the \mathcal{L} integrated over a period of time. The numbers quoted in the text correspond to the integrated luminosity recorded by ATLAS considering only the good quality data [89].

beams are accelerated up to the desired energy.

In the LHC ring, seven detectors are placed at different LHC collision points. They are introduced in the next section.

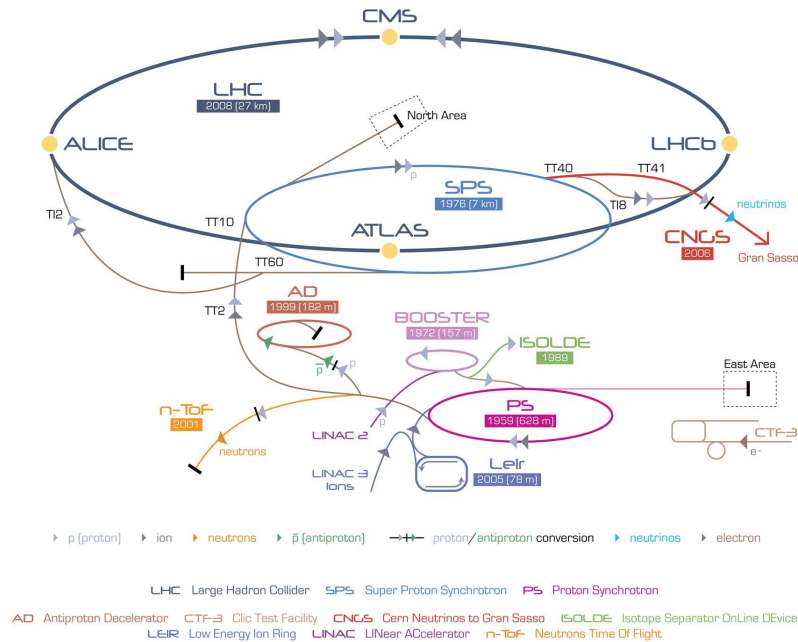


Figure 4.2: The accelerator complex at CERN. Figure from the CERN public web-pages [90].

4.1.1 The LHC experiments

The LHC has seven experiments [91] that use detectors to study the myriad of particles produced in the collisions. The biggest four detectors, Fig. 4.3, sit underground in huge caverns in the LHC. They are:

- Compact Muon Solenoid (CMS) [92]:** It is a general purpose experiment for high luminosity designed and built to have a high performance for SM model precision measurements as well as for the SM Higgs searches and BSM searches. It has a high performance system to detect and measure muons, a high resolution method to detect and measure electrons and photons (an electromagnetic calorimeter), a high quality central tracking system to give accurate momentum measurements, and a "hermetical" hadron calorimeter, designed to entirely surround the collision and prevent particles from escaping without detection. It is the heaviest detector at LHC (125000 tons) and it can generate a magnetic field up to 4 T.
- ATLAS [93]:** It is the other general purpose experiment for high luminosity. It has the same discovery potential as CMS although the hardware and software

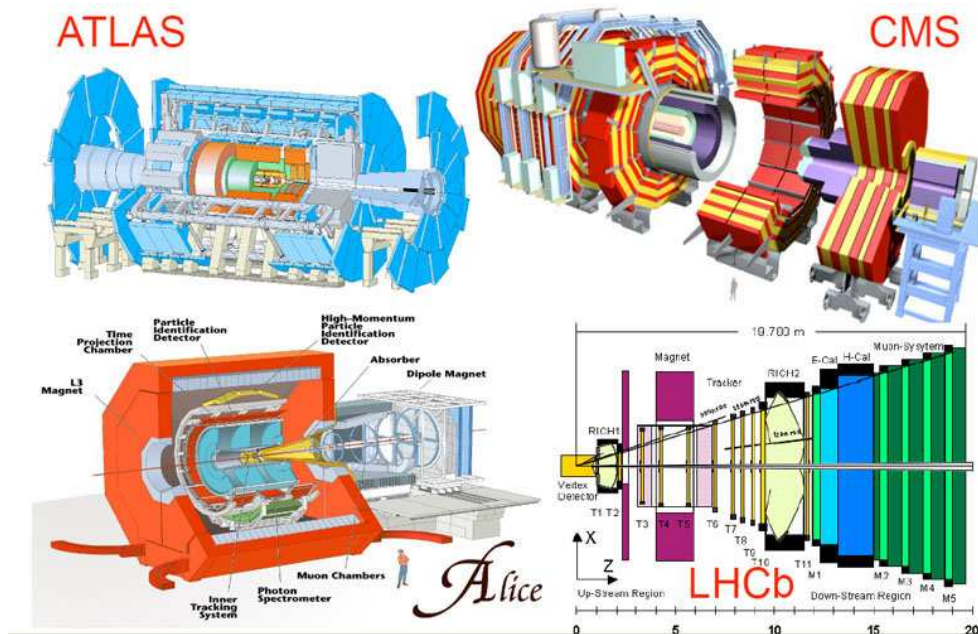


Figure 4.3: The biggest LHC experiments. From left to right and from up to down: CMS, ATLAS, ALICE and LHCb. Figure from the CERN public webpages [90].

are different. Is the largest experiment built at CERN with a volume of $44 \times 25 \text{ m}^2$ and a weight of 7000 tons. It has two magnets: a toroid which generates up to 6 T/m for the muon spectrometer (the most external part of the detector) and a 2 T solenoid for the inner detector.

- **A Large Ion Collider Experiment (ALICE)** [94]: This experiment is focused on the study of the quark-gluon plasma, a state of matter composed by asymptotically free quarks and gluons, produced when the LHC is colliding ions (Pb-Pb) at high energy.
- **Large Hadron Collider beauty (LHCb)** [95]: It is specialized in the physics of the b -quark, specifically in the measurement of \mathcal{CP} violation in the interactions of b -hadrons that can help to explain the matter-antimatter asymmetry of the Universe. This experiment was designed to work with low luminosity conditions. The detector is able to perform measurements in the forward region since the LHCb detector is a single arm forward spectrometer with a polar angular coverage from 10 to 300 milliradians ($mrad$) in the horizontal and 250 $mrad$ in the vertical plane.

The other three experiments are smaller and share cavern or interaction point with any of the four bigger experiments:

- **Large Hadron Collider forward (LHCf)** [96]: It is a special purpose experiment designed to study neutral pions produced in the forward region of the collisions.

It shares cavern with ATLAS and it consists on two detectors placed at 140 m on either side of the ATLAS intersection point.

- **TOTAL Elastic and diffractive cross section Measurement (TOTEM) [97]:** It shares intersection point with the Compact Muon Solenoid. The detector aims at measurement of total cross section, elastic scattering, and diffractive processes.
- **Monopole and Exotics Detector at the LHC (MOEDAL) [98]:** It is deployed around the same intersection region as the LHCb detector and its prime motivation is the direct search for the magnetic monopole (a hypothetical particle with a magnetic charge).

4.1.2 The Worldwide LHC Computing Grid (WLCG)

The Worldwide LHC Grid Computing Grid (WLCG) is a global collaboration that consists of more of 170 computing centers in 40 countries, linking national and international grid infrastructures. The computing model was born with the aim of building and maintaining a computing infrastructure able to deal with the huge amount of data that the LHC produces. This computing model is based on Grid technologies. Thus, the WLCG provides a global computing resources to store, distribute and analyze the $\sim 30 Pb$ (petabytes) generated by the LHC. The WLCG is able not only to deal with the huge amount of data, but it has also to provide access to these data to a large number of scientists (~ 6000) spread over the world to perform their analysis almost simultaneously.

The WLCG is split in three different Grid projects: the LHCComputing Grid (LCG) in Europe, the NorduGrid/ARC also in Europe but only involving the Nordic countries and Open Science Grid (OSG) in the US.

The LHC distributed computing model is hierarchical based on sites called Tiers. The first one, based at CERN, is the Tier0 center. In this center, the LHC data is recorded as a primary backup and processed. After this processing, the data are distributed to the Tier1 centers. There are 11 Tier1 sites worldwide and each one defines a cloud. The Tier1 centers make the data available to their Tier2 centers (140 around the world). The Tier2 centers consist in one or several computing facilities that allow to store the data and that have the adequate computing power for specific analyses. The access to these facilities is made, by the physicists, by their closest Tier3 computing resources, which use the local resources of their investigation centers. In this way, the jobs sent by the physicists to perform any analysis would run where the data is stored, avoiding long data transmission.

4.2 The ATLAS detector

The ATLAS experiment [93] is a multi-purpose particle physics detector with forward-backward symmetric cylindrical geometry (4π coverage). It consist in layers of sub-detectors, being 44 m long and 25 m high. See Fig. 4.4.

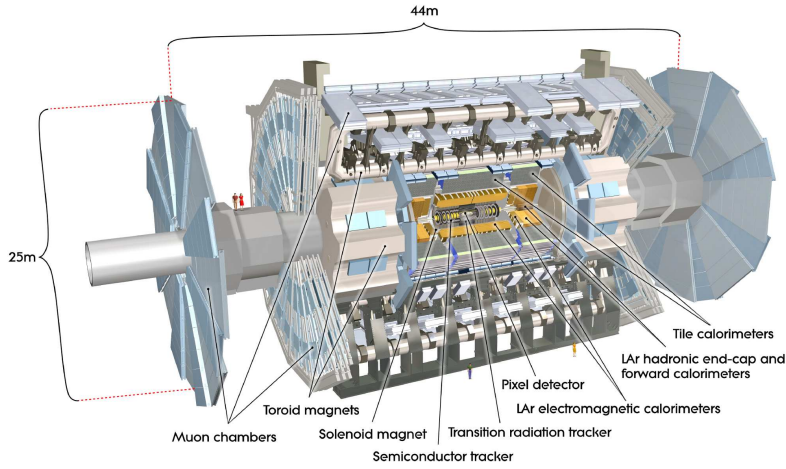


Figure 4.4: The ATLAS detector with all its sub-detectors labeled. For a scale reference, few human figures are included in the picture. Figure from the ATLAS public web-pages [99].

The closest system to the beam pipe is the inner tracking detector (ID) which consists of a silicon pixel detector, a silicon microstrip detector (SCT), and a straw-tube transition radiation tracker (TRT). The ID is surrounded by a thin superconducting solenoid which provides a 2 T magnetic field. Outside the solenoid, a high granularity liquid-argon (LAr) sampling electromagnetic calorimetry is placed. The electromagnetic calorimeter is divided into a central barrel (pseudorapidity ¹ $|\eta| < 1.475$) and end-cap regions on either end of the detector ($1.375 < |\eta| < 2.5$ for the outer wheel and $2.5 < |\eta| < 3.2$ for the inner wheel). The ID is presented in Section 4.2.1.

Surrounding the latter, is the hadronic calorimeter: an iron-scintillator/tile calorimeter that gives hadronic coverage in the central rapidity range ($|\eta| < 1.7$) and a liquid Argon (LAr) hadronic end-cap calorimeter that provides coverage over $1.5 < |\eta| < 3.2$. The forward regions ($3.2 < |\eta| < 4.9$) are instrumented with LAr calorimeters for both electromagnetic and hadronic measurements. Their characteristics are explained in Section 4.2.2.

The last sub-detector is the muon spectrometer (MS) which surrounds the calorimeters and consists of three large air-core superconducting magnets providing a toroidal field, each with eight coils, a system of precision tracking chambers, and fast detectors for triggering. The MS covers the $|\eta| < 2.5$ range. It is presented in Section 4.2.3.

The high design luminosity of the LHC ($10^{34} \text{ cm}^{-2}\text{s}^{-1}$) will lead to interaction rates of $\sim 1 \text{ GHz}$. Most of them are due to minimum bias events with limited interest. Since data storage technology limits the amount of data that can be stored, a decision

¹ATLAS uses a right-handed coordinate system with its origin at the nominal interaction point (IP) in the center of the detector and the z -axis along the beam pipe. The x -axis points from the IP to the center of the LHC ring, and the y -axis points upward. Cylindrical coordinates (r, ϕ) are used in the transverse plane, being the azimuthal angle around the beam pipe. The pseudorapidity is defined in terms of the polar angle θ as $\eta = -\ln[\tan(\theta/2)]$. Transverse momentum and energy are defined as $p_T = p \sin \theta$ and $E_T = E \sin \theta$, respectively.

making system, called trigger system, is needed. Their main features are presented in Section 4.2.4.

4.2.1 The Inner Detector

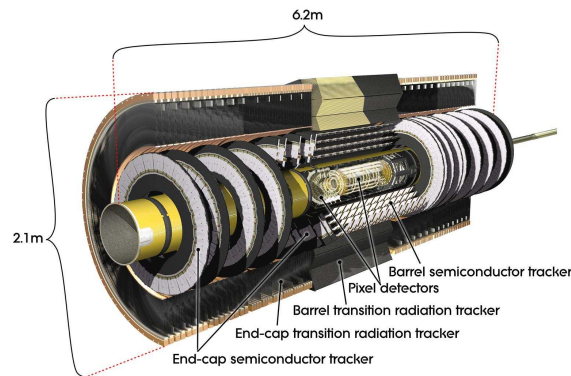


Figure 4.5: Schematic view of the ATLAS Inner Detector. The different systems are shown: the pixel detector with its three barrel layers and its three end-cap discs; the semiconductor tracker with its four barrel layers and its nine end-cap discs; and the transition radiation tracker with its three barrel layers and its two end-cap wheels on each side. Figure from the ATLAS public webpages [99].

The Inner Detector (Fig. 4.5) is the ATLAS tracker system[100]. The ID is built in the closest region to the beam pipe and the interaction point to be able to perform the pattern recognition, momentum and vertex measurement together with lepton identification, specially for electrons. To bend the trajectory of the charged particles crossing the ID to measure their charge and momentum, it is surrounded by a thin superconducting solenoid which provides the 2 T axial magnetic field. Thanks to the three subsystems that forms the ID, the ID detector covers a region of $|\eta| < 2.5$.

The most inner subsystem is the Pixel sub-detector which is based in silicon technology and occupies the radii between 5 and 15 cm from the interaction point to achieve high precision measurements as close as possible to the interaction point. It consists of three cylindrical barrel layers (at average radii of 5.05 cm, 8.85 cm and 12.25 cm) and three discs on each side of the central barrel (at 49.5 cm, 58.0 cm and 65.0 cm from the center of the ATLAS coordinates system). With a size of $50 \times 400 \mu\text{m}^2$ the pixels obtain an intrinsic resolution of $10 \mu\text{m}$ in the transverse direction with a direct 2D readout. Moreover, with 80.4 million channels a high granularity is obtained.

The semiconductor tracker (SCT) is a silicon microstrip based detector located just after the Pixel detector. It has its modules arranged on four barrels and nine end-cap discs on each side. It provides four precise space points in the intermediate radii (from 30 to 56 cm) of the inner detector and covering a distance along of the beam of 80 cm in both directions by the barrels and 190 cm more in both directions by the end-caps. The four cylindrical barrels cover the $|\eta| < 1.4$ range whereas the two end-

caps with nine wheels each extend the acceptance to $|\eta| < 2.5$. The modules of the four layer of the barrels are back-to-back silicon microstrip detectors with a relative 40 mrad stereo angle. Both measurements are combined to allow the determination of a 2D space point with a resolution of $17\mu\text{m}$ in $r\phi$. The achieved resolution in the beam direction is $580\mu\text{m}$. The SCT is composed by 61 m^2 of silicon sensors (4088 modules divided in 2112 in the barrel and 1976 in the end-caps) with 6.3 million channels.

The Transition Radiation Tracker occupies the outermost region in the ID. It consists of about 300.000 gaseous straw tubes arranged in a barrel and two end-caps on each side of this barrel. It detects the charged particle thanks to the transition radiation¹ which is produced when a relativistic particle traverses an inhomogeneous medium. Electron/hadron discrimination is possible for momenta larger than $\sim 1\text{ GeV}$. The TRT has 176 modules, 73 layers in 3 rings in the barrel region and 2×160 straw planes in 40 four-plane assembly units in the end-cap regions. The straws are filled by a mixture of $Xe/CF_4/CO_2$ (70%/20%/10%) gases that measures the passage of the charged particles through ionization of the gas and the transition radiation X -rays that are absorbed by the gas molecules. Multiple polyethylene foils acts as radiator. An intrinsic resolution of $130\mu\text{m}$ per straw is achieved (in the perpendicular direction to the wire). The TRT provides on average, in the barrel region, 36 hits for tracks coming from the interaction point.

The track parameters resolution achieved with the ID are summarized in Tab. 4.1.

Table 4.1: Track parameter resolutions for the ID. The ϕ_0 is the azimuthal angle, the $\cot\theta$ is the cotangent of the polar angle and the p_T is the transverse momentum. The d_0 and the z_0 are the transverse and longitudinal impact parameters respectively. The transverse momentum p_T is given in GeV.

Track Parameter	Resolution dependence
Azimuthal angle	$\sigma(\phi_0) \simeq 0.075 \oplus \frac{18}{p_T \sqrt{\sin\theta}}$ (mrad)
Polar angle	$\sigma(\cot\theta) \simeq 0.70 \cdot 10^{-3} \oplus \frac{20 \cdot 10^{-3}}{p_T \sqrt{\sin\theta^3}}$
Inverse transverse momentum	$\sigma(1/p_T) \simeq 0.36 p_T \oplus \frac{13}{\sqrt{\sin\theta}}$ (TeV^{-1})
Transverse impact parameter	$\sigma(d_0) \simeq 11 \oplus \frac{73}{p_T \sqrt{\sin\theta}}$ (μm)
Longitudinal impact parameter	$\sigma(z_0) \simeq 87 \oplus \frac{115}{p_T \sqrt{\sin\theta^3}}$ (μm)

4.2.2 The Calorimetry System

The ATLAS calorimeters, Fig. 4.6, are built outside the ID solenoid. They are to measure the energy and direction ($\theta - \phi$) of all particle and jets produced in the collision. The energy measurement of the calorimeters is based on the formation of

¹The transition radiation is emitted in the X -ray regime, i.e. between 10 and 30 keV, and in the forward direction

a cascade of particles (so-called shower) due to electromagnetic bremsstrahlung and pion decays.

The first calorimeter, just outside the ID solenoid, is the electromagnetic calorimeter (ECAL), which uses liquid argon as an ionization medium with the lead absorbers arranged in an accordion geometry. It is surrounded by cryostat to reach the very low temperatures needed to be operative. The ECAL is also known as the LAr calorimeter. With this kind of geometry, the ECAL, provides a total ϕ coverage without azimuthal cracks. The thickness of the lead absorbers has been optimized as a function of η to have a good performance in terms of energy and position resolution of electrons and photons. The ECAL covers up to $|\eta| < 3.2$. The ECAL has an energy resolution of:

$$\frac{\sigma_E}{E} = \frac{11.5\%}{\sqrt{E}} \oplus 0.5\% \quad (E \text{ in GeV})$$

The Hadronic Calorimeter (HCAL) surrounds the ECAL. The HCAL is to measure hadronic jets within $|\eta| < 4.9$. To measure the energy depositions, it uses a sampling technique with plastic scintillator plates called tiles embedded in iron absorbers for the hadronic barrel calorimeter (called TileCal). The TileCAL is separated into a large central barrel and two smaller extended barrels. The end-caps use LAr technology matching the outer $|\eta|$ limits of end-cap electromagnetic calorimeters. They can measure both kind of showers: hadronic and electromagnetic. The HCAL has an resolution of:

$$\frac{\sigma_E}{E} = \frac{50\%}{\sqrt{E}} \oplus 3\% \quad (E \text{ in GeV})$$

The total calorimeter system hermetically covers a large geometrical acceptance. Therefore the presence in the event of neutrinos or other particles that interact very weakly can be inferred from the measurement of the unbalanced transverse energy, called transverse missing energy, E_T^{miss} .

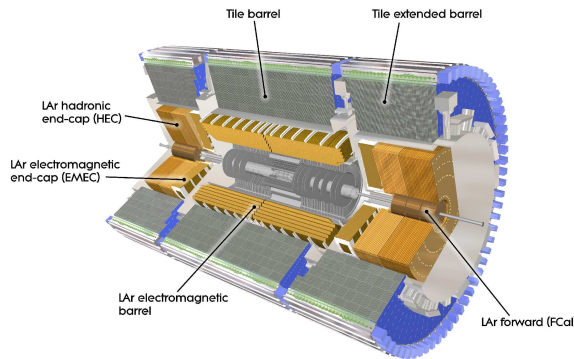


Figure 4.6: Schematic view of the ATLAS calorimeters with its sub-detectors labeled. Figure from the ATLAS public webpages [99].

4.2.3 The Muon System

Muons do not feel the strong interactions and are relatively heavy particles therefore the dominant energy loss mechanism is the ionization. Therefore, the muons traverse the whole ATLAS detector (ID and calorimeters) with very low interaction. The muon spectrometer (MS), Fig. 4.7, surrounds the calorimeters and defines the overall dimensions of the ATLAS detector. The MS provides efficient identification ($> 90\%$) of muons with $p_T > 6$ GeV and $|\eta| < 2.7$. It consists in four technologies. Two of them provide the tracking information by high precision momentum measurement of the muons. They are the Monitored Drift Tubes (MDT) and the Cathode Strip Chambers (CSC). The two other technologies are used for triggering with timing resolution of the order of $1.5 - 4$ ns and bunch crossing identification. They are the Resistive Plate Chambers (RPC) and the Thin Gap Chambers (TGC). The resolution in the transverse momentum is $\frac{\sigma_{p_T}}{p_T} \leq 10^{-4}$ for $p_T > 300$ GeV and a few per cent for lower transverse momentum. This limitation is due to Multiple Coulomb Scattering (MCS) effects in the magnet and detector structures, and by energy loss fluctuations in the calorimeters.

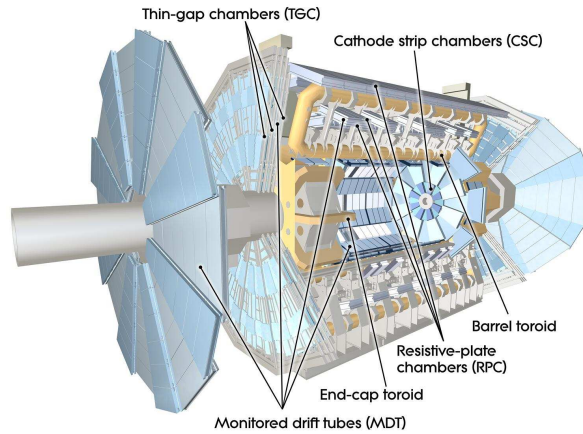


Figure 4.7: Schematic view of the ATLAS Muon Spectrometer with its subsystems labeled. Figure from the ATLAS public webpages [99].

The large volume of the MS needs of a strong bending power within a light and open structure. This is obtained by an air-core toroid. The MCS are minimized and excellent muon momentum resolution is achieved in the three layer of the MDT (with precisions of $\sim 50 \mu\text{m}$ in the muon position). The magnetic system consists in one barrel toroid magnet that has 25 m long with an inner bore of 9.4 m and an outer diameter of 20.1 m and two inserted end-cap magnets with a length of 5.0 m and inner bore of 1.65 m and an outer diameter of 10.7 m. Eight flat coils assembled radially and symmetrically around the beam conform the barrel toroid which provides bending powers of 3 Tm in the barrel and 6 Tm in the end-caps. The end-cap toroids provide radial overlap and optimize the bending power in the transition region by being rotated in azimuth by an angle of 22.5° with respect to the barrel coils.

4.2.4 The Trigger System

The trigger system is needed to store the information obtained by the different subdetectors for the interesting physics events, while it reduces the number of minimum bias events to be stored. The trigger system is divided in three different levels, called LVL1 (first level), LVL2 (second level) and the event filter. A schematic view of them is shown in Figure 4.8. The LVL1 make use of a subset of the calorimeter and muon detectors. It acts before the data is collected by the readout drivers (RODs). If relative high transverse momentum objects are detected in the mentioned detectors, the LVL1 triggers. It reduces the amount of data to $\sim 100 \text{ kHz}$. The LVL2 uses the full granularity from all subdetectors, including the inner detector, but considering reduced regions of interest defined by the LVL1 trigger. The events are processed using processor farms looking for interesting objects: high p_T leptons, jets or photons, a single jet with very high p_T , large amounts of transverse missing energy, etc,. The final stage is the event filter. Before this stage, the event was reduced to $\sim 1 - 2 \text{ kHz}$. At this point the data calibrations are available and the event rate is reduced to $\sim 200 \text{ Hz}$.

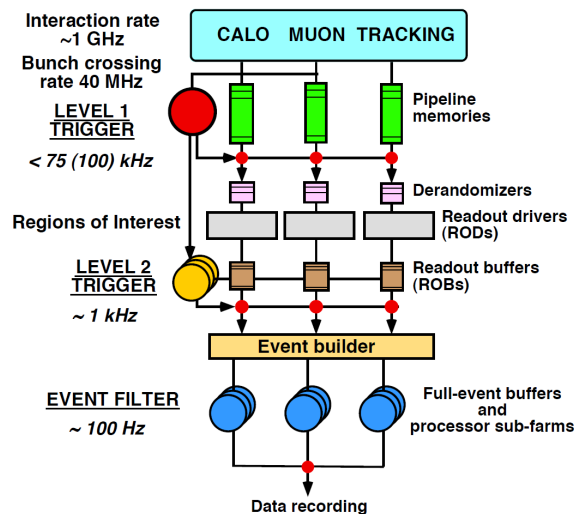


Figure 4.8: Schematic view of the ATLAS trigger levels. Figure from the ATLAS public webpages [99].

Reconstruction of $t\bar{t}$ +1-jet events using the ATLAS detector

The measurement of the \mathcal{R} distribution and therefore the extraction of m_t^{pole} is based in the reconstruction of $t\bar{t}$ + 1-jet topologies. The reconstruction of $t\bar{t}$ + 1-jet events using the ATLAS detector is presented in this chapter. For that, the data collected by the ATLAS detector for pp collisions at a center-of-energy of 7 TeV is used. The data sample was recorded during 2011 and the total integrated luminosity of the data set is 4.6 fb^{-1} with an uncertainty of 1.8% [89].

The experimental signature for $t\bar{t}$ + 1-jet events is discussed in Section 5.1. Then the definition of the different objects used during the kinematical reconstruction of $t\bar{t}$ + 1-jet events (electrons, muons, jets, ...) and the event selection for $t\bar{t}$ + 1-jet events are presented in Section 5.2. The data and Monte Carlo samples used in the analysis are presented Section 5.3. Finally, in Section 5.5, the kinematical algorithm to reconstruct $t\bar{t}$ + 1-jet events is discussed.

5.1 Experimental signature for $t\bar{t}$ +1-jet events

The chosen $t\bar{t}$ decay channel for the analysis presented in this thesis is the semileptonic channel since it presents the best compromise between the efficiency of selection and rejection of backgrounds (see Chapter 3). Identifying the missing E_T as produced by the neutrino and using the W mass as a constraint, the neutrino four momentum can be estimated, if only one neutrino is produced during the $t\bar{t}$ decay.

Usually the events where there is one or more τ lepton coming from the decay of the W bosons are treated in a different way. The experiments use muons or electrons as triggers due to the fact that the τ lepton decays into a neutrino and a W boson which decays again into lepton plus neutrino or into two quarks, generating complicated final state topologies. The presence of an extra neutrino (or two in the case that the τ

decays leptonically) makes the reconstruction of the four momentum of the system more difficult. Therefore, from now on in the text, any reference to the semileptonic (also called lepton+jets or l +jets) channel will be done assuming that the contribution of the τ leptons is not considered.

Thus the expected signature for $t\bar{t}$ + 1-jet events produced in the semileptonic channel (also referred as l +jets or lepton+jets channel) is the following: two jets produced by the two b -quarks, two jets produced by the quarks decayed from the W boson, one high p_T lepton (μ or e), the presence of missing transverse energy associated to the neutrino and at least one jet not associated to the $t\bar{t}$ decay products.

5.2 Object definition and event selection

In this section, the identification and definition of such objects (leptons, jets...) by the ATLAS detector is presented. The basic $t\bar{t}$ + 1-jet event selection is presented at the end of this section.

5.2.1 Object definitions

The object reconstruction and definitions used in this analysis are identical to those in most top physics analysis in ATLAS (see for example the Refs. [101, 102]). The primary vertex is chosen as the vertex with the highest Σp_T^2 for tracks with $p_T > 0.4$ GeV. At least 5 tracks with $p_T > 0.4$ GeV and a lepton candidate must be present in the event to be considered in the analysis.

Candidates for final state objects are reconstructed as follows:

Electrons: are reconstructed in the calorimeter using a cluster-based algorithm. They are selected if they fulfill the *Tight++* definition, which implies stringent selection cuts in calorimeter, tracker and combined information to provide a good separation between electrons and jets (fake electrons). Moreover, they are required to have $p_T > 25$ GeV and $|\eta_{clus}| < 2.47$, where η_{clus} denotes the pseudorapidity of the calorimeter cluster. The clusters placed in the calorimeter transition region ($1.37 < |\eta_{clus}| < 1.52$) are excluded. Additionally, an isolation criterion is applied: transverse energy deposits within $\Delta R = 0.2$ (excluding the cells associated to the electron) are required to be below a certain threshold which is chosen such that the efficiency for electrons selected in $Z \rightarrow ee$ events passing this isolation requirement is 90%. In addition, the sum of the transverse momenta of the tracks within $\Delta R = 0.3$ around the electron direction is restricted to be below certain threshold that depends on the cluster energy and the pseudorapidity. This threshold is also chosen by requiring the 90% of efficiency in the reconstruction of the electrons in $Z \rightarrow ee$ events. The selected electrons must match electron triggers of each data taking period.

Muons: are reconstructed combining the track candidates identified in the muon spectrometer and the inner detector. In this case, $p_T > 20$ GeV and $|\eta_{clus}| < 2.5$ are required. The sum of the calorimeter transverse energy within $\Delta R = 0.2$

is required to be below 4 GeV, and the p_T of all the track within $\Delta R = 0.3$, excluding the muon track, must be below 2.5 GeV. Finally, the selected muon have to match muon triggers of each data taking period.

Jets: are reconstructed from the the energy deposits in the calorimeters that are joint into topological clusters using a three-dimensional algorithm [103]. These clusters are fed into the anti- k_T jet clustering algorithm with a radius parameter $R = 0.4$. Reconstructed jets must have $p_T > 25$ GeV and $|\eta| < 2.5$. Reconstructed jet energies in MC are calibrated from stable particle jets. Residual calibrations, derived using in-situ methods where the jet transverse momentum is compared to that of a reference object (e.g. using γ/Z +jet events), are then applied to data relative to the MC [104]. Reconstructed jets must have $p_T > 25$ GeV and $|\eta| < 2.5$. To suppress the contribution from low- p_T jets originating from pile-up interactions, a jet vertex fraction requirement is applied: jets are required to have at least 75% of the scalar sum of the p_T of tracks associated with the jet to come from tracks associated with the event primary vertex.

b -tagged jets: originated by a b -quark are identified using the MV1 b -tag algorithm. This algorithm is based on a neural network exploiting the long life-time of b -hadrons [105, 106, 107] that results in tracks with large impact parameter with respect to the primary vertex and, also, in secondary and tertiary vertices. The calibration is derived from data including $t\bar{t}$, dependent on the p_T and η . The working point has been set to 70% of efficiency.

Missing transverse energy (E_T^{miss}): is defined as the event momentum imbalance in the transverse plane to the beam axis. This imbalance is associated to the neutrinos that escape the experiment undetected and it is measured as the vector sum over momenta over all the topological clusters in the event that are not associated to the presence of electrons, muons, jets, soft jets and calorimeter cell-out term which accounts for the energy deposits not associated to the previous objects [108].

After selecting the objects, overlap between the object collections is removed using the following criteria: first, muons within $\Delta R = 0.4$ of a selected jet are removed; second, any jet within $\Delta R = 0.2$ of a reconstructed electron is removed; and finally, any electron within $\Delta R = 0.4$ of the remaining jets is removed.

All these objects are corrected through scaling and smearing the nominal values in the Monte Carlo to improve the agreement with the data. The object corrections are implemented during the identification and reconstruction following the recommendations and instructions provided on the TopCommonScales twiki [109]¹.

5.2.2 Basic event selection

Once that all needed objects are identified, the event selection for $t\bar{t} + 1$ -jet events is performed.

¹They are implemented in the TopRootCoreRelease-11-00-08 software package developed by the top-quark group of the ATLAS collaboration.

First requirements are: the presence of a lepton matched with its trigger and with a minimum p_T cut requirement to optimize the efficiency of reconstruction, the presence of at least one primary vertex with enough associated good tracks to reduce the possibility of including pile-up events during the reconstructions. Moreover, bad events due to a bad reconstruction in some regions of the LAr calorimeter are rejected:

1. single lepton trigger, with thresholds at 18 GeV for muons and 20 or 22 GeV for electrons;
2. the selected lepton and the trigger object are required to be matched ($\Delta R < 0.15$);
3. bad events due to noise bursts in the liquid argon calorimeter are rejected;
4. at least one primary vertex with at least five associated good tracks;
5. exactly one good charged lepton with p_T greater than 25 GeV (electron or muon);

Then, two b -tagged jets and at least three other jets are required.

6. at least five good jets;
7. exactly two identified b -quark jets;

The presence of a neutrino is inferred from the presence of the unbalance in transverse energy:

8. the magnitude E_T^{miss} of the missing transverse momentum must be greater than 30 GeV;

Finally, an extra cut in the W -boson transverse mass¹ reconstructed with the missing transverse momentum and the charged lepton, m_T^W , is performed to reduce the contamination of multijet events due to the presence of *fake* leptons:

9. m_T^W must exceed 30 GeV.

5.3 Data sample and event selection

The $t\bar{t}$ + 1-jet events are reconstructed using the data collected by ATLAS during 2011. The data sample includes all data recorded in the 2011 data taking periods with stable beam conditions and all relevant subdetector systems operational.

The simulation of the signal events is performed with NLO calculations of $t\bar{t}$ topologies. The different backgrounds that have been considered are: W/Z +jets topologies, single top production, diboson production and multijet events due to *fake* and non

¹The W -boson transverse mass is defined as $m_T^W = \sqrt{2p_{T,l} p_{T,\nu} [1 - \cos(\phi_l - \phi_\nu)]}$ where l is the selected lepton and ν the neutrino. The neutrino kinematics is given by the E_T^{miss} vector.

prompt leptons. All these processes contain lepton and high multiplicity jet final states. All the backgrounds, except the multijet contribution, are estimated using Monte Carlo simulations (summarized in the following paragraphs). The contribution of the multijet events is estimated using data-driven methods.

All the simulated events are processed with the full ATLAS detector simulation based on Geant4 [110]. The simulation conditions and samples described correspond to the standard prescriptions of the ATLAS top physics group for the analysis performed using the 7 TeV data sets. Further information and links to the sample, the related production tasks, ATLAS MetaData Interface details are available at the top group MC11 campaign Monte Carlo pages [111]. The same offline reconstruction methods are applied to the simulated samples as to the data.

5.3.1 Monte Carlo Simulation

This section describes the details of the Monte Carlo simulation samples used in the analysis. A number of Monte Carlo event generators are used to generate samples of $t\bar{t}$ signal events, as well as other sources of SM background.

In this analysis, several Monte Carlo samples are used for the modeling of $t\bar{t}$ pair production and the main background processes. For the simulation of the $t\bar{t}$ signal, the POWHEG code [48, 112] (POWHEG-hvq, *patch4*) is used to calculate the QCD matrix element at NLO with the CT10 [58] parton distribution function (PDF). The parton shower and the underlying event are added using the PYTHIA [42] (v4.01) generator with the Perugia 2011C tune [113]. The nominal $t\bar{t}$ @NLO+PS sample is produced assuming a top-quark mass of $m_t = 172.5$ GeV. The corresponding cross section is $\sigma_{t\bar{t}} = 177^{+10}_{-11}$ pb, based on next-to-next-to-leading order (NNLO) QCD calculations including the resummation of next-to-next-to-leading logarithmic (NNLL) soft gluon terms with top++ 2.0 [50, 51, 52, 53, 55]. In addition to the nominal sample, five samples are used with different assumptions of the top-quark mass in the range [167.5, 180] GeV in steps of 2.5 GeV.

Single top quark production via electroweak interactions is simulated using POWHEG interfaced with PYTHIA v6.4. The Perugia 2011C Tune is used for s -channel, t -channel and Wt -channel production.

The production of W/Z bosons in association with jets (W +jets or Z +jets) is simulated using the ALPGEN generator [114] (v2.13) with the LO CTEQ6L1 [115] PDF. These calculations are interfaced with HERWIG and JIMMY. The W +jets events containing heavy-flavor quarks (b -quark and c -quarks pairs and single c -quarks) are generated separately using leading-order matrix elements with massive b - and c -quarks. An overlap removal procedure is used to avoid double-counting due to heavy quarks produced by the parton shower. The W +jets heavy flavor composition is estimated using the tag counting method in 1- and 2-jet bins in the pretag and tag samples. The yield for the W +jets process is normalized exploiting the lepton charge asymmetry observed in data [116].

Finally, diboson events (WW , ZZ , WZ) are generated using HERWIG with the MRSTMCa1 PDF [117].

5.3.2 Multijet events

The multijet background is the only background which is estimated using a fully data-driven method. This background is due to the presence of *fake* leptons: the ones that are no prompt nor isolated leptons from W/Z decays. Non-isolated muons are produced, mainly, in the semileptonic decay of B -hadron decays, where the muon passes the isolation requirement. The fake electrons are produced in three main processes: heavy-flavor decay, light-flavor jets that are misidentified as electrons, and photon conversions.

To estimate the rate of such a fake leptons, the data driven Matrix Method discussed in Ref. [118] is used. The method make uses of two control samples that are based on loose and tight lepton isolations definitions. The loose selection requires more relaxed identification criteria and the isolation requirements are removed. According to this method and using measured efficiencies of real and fake leptons, one can express the number of fake leptons passing the tight isolation requirements as:

$$N_{fake}^{tight} = \frac{\epsilon_{fake}}{\epsilon_{real} - \epsilon_{fake}} (N^{loose} \epsilon_{real} - N^{tight}) \quad (5.1)$$

where N^{tight} and N^{real} are the number of events with a tight or loose lepton, respectively, and the ϵ_{real} and ϵ_{fake} are the fractions of real and fake loose leptons which pass the tight selection. The measurement of the electron identification efficiency ϵ_{real} is derived through the tag-and-probe method with a sample of Z decaying to leptons. The ϵ_{fake} are measured in control regions which are dominated by contributions from fake leptons. These control regions pass lower E_T^{miss} and m_T^W requirements or are composed by events with high track impact parameter.

5.4 Event yields after the basic selection

The basic selection described so far identifies 8275 events in the l +jets channel. The yield is compared to the Standard Model prediction in Tab. 5.1 for the l +jets channel. The contributions of several Standard Model processes are presented separately. The systematic uncertainties quoted in the table correspond to a subset of the most important uncertainties considered in this analysis: those on the jet energy scale (JES), initial- and final- state modeling, b -tagging efficiency, Monte Carlo generator and hadronization modeling, for the signal yields; the normalization uncertainties for the $(Z)W$ +jets yields; the normalization, shape and Monte Carlo mass dependence for the single top yields; and the shape and normalization uncertainties for the multi-jet background estimation. A complete description of all systematic uncertainties will be presented in Section 6.6.

For a number of kinematic variables that are important to the event selection the distributions of the data are compared to the Standard Model expectation in Figures from 5.1 to 5.2. The first shows the reconstructed missing transverse energy, the m_T^W and the lepton p_T and η . The second shows the p_T , η and multiplicity for the light-jets (non b -tagged jets) and for the b -tagged jets. The same set of systematic

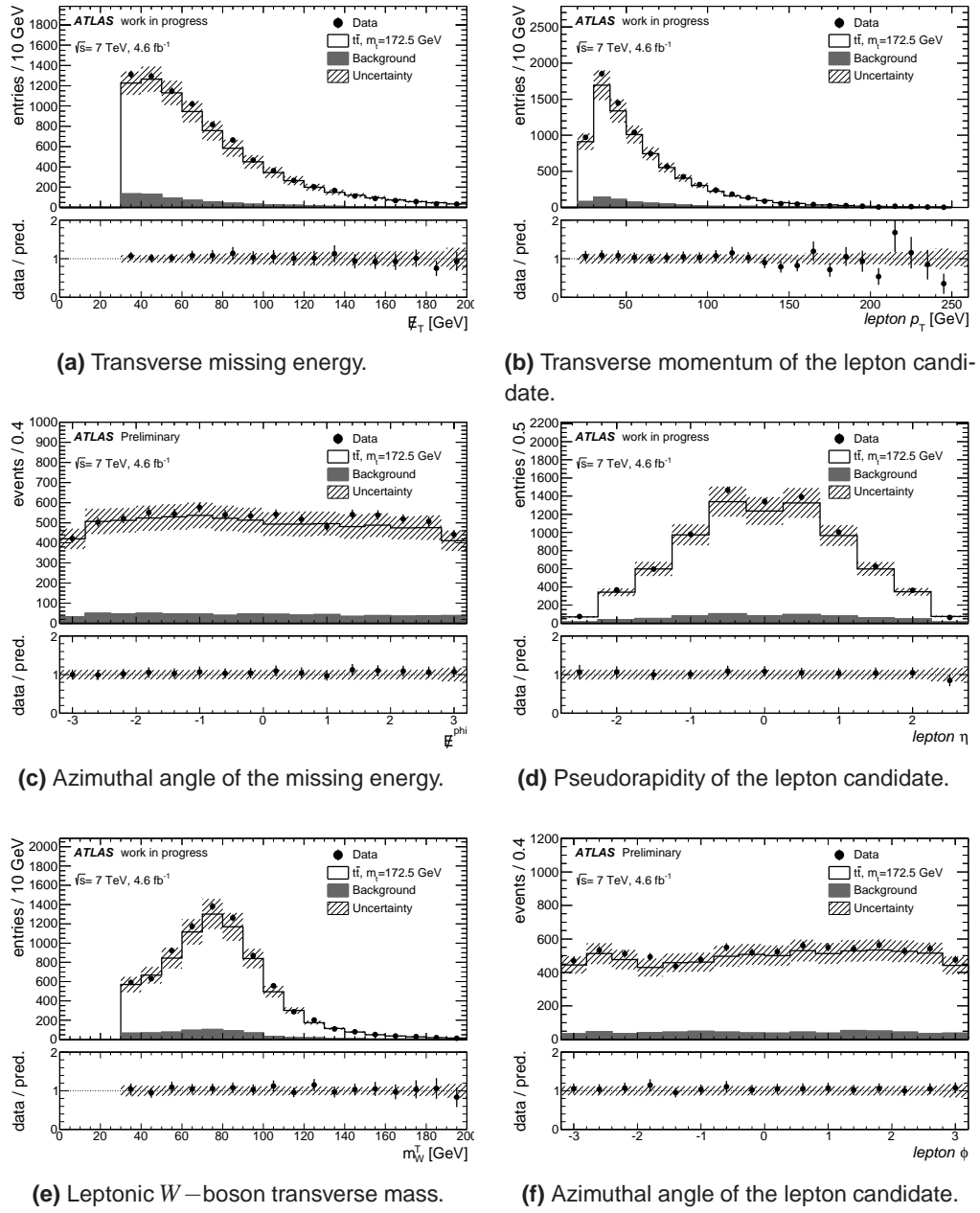


Figure 5.1: The data for different kinematic distributions are compared after the basic selection to the $t\bar{t}$ @NLO+PS calculations (POWHEG+PYTHIA) with an assumed Monte Carlo mass $m_t = 172.5 \text{ GeV}$. Tab. 5.1.

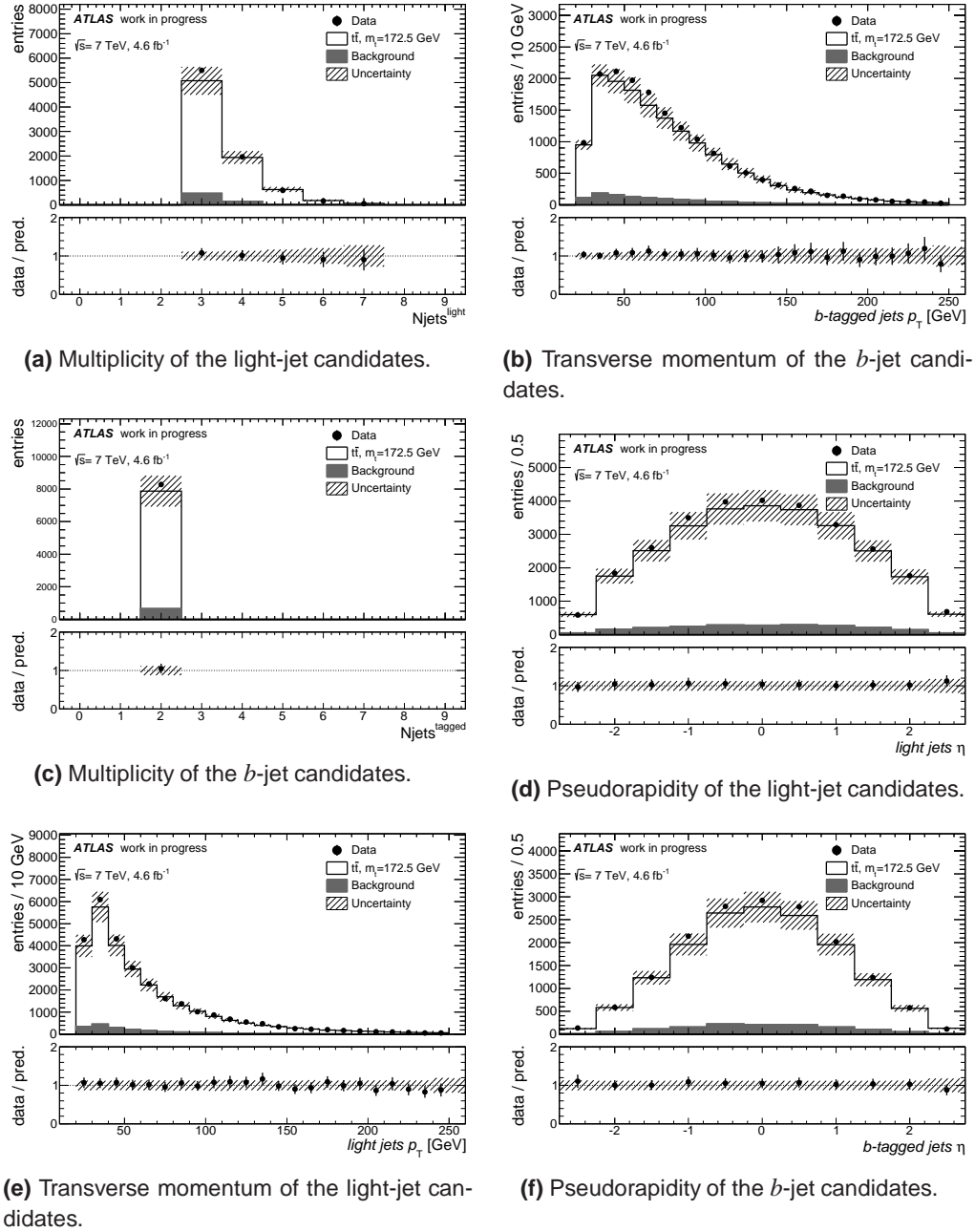


Figure 5.2: Similar to Figure 5.1.

	events	stat	syst
Data	8275	-	-
signal ($t\bar{t}$, $m_t = 172.5$ GeV)	7209 (91.5%)	85	1564
W +jets	206(2.5%)	14	99
Z +jets	35(0.4%)	6	17
Single top	326(3.9%)	18	297
WW, ZZ, WZ	5(0.1%)	2	0
Multi-jet	94(1.1%)	10	55
Total Background	665(8.0%)	26	318
Predicted	7874	89	1596
(data-B) / B	11.4	0.2	3.0

Table 5.1: Event yields after the basic selection. The data yield for the l +jets channel is compared to the Standard Model expectation based on Monte Carlo predictions. The statistical and the systematic uncertainties are separately quoted. Only the largest systematic uncertainties have been accounted (see body text). The relative contribution of each process is reported in percent in parenthesis.

uncertainties evaluated in Tab. 5.1 are shown in the figures. For all kinematic variables good agreement is observed between the data distribution and the template based on Monte Carlo distributions for the signal and major backgrounds.

5.5 Reconstruction of the $t\bar{t}$ +1-jet events

After the basic selection, a kinematical reconstruction of the events is performed to identify the $t\bar{t}$ + 1-jet system. The first step consist in identify the W -boson candidates. Then, the two identified b -tagged jets are associated to the two b -quarks produced in the top-quark decays. The $t\bar{t}$ system is reconstructed from these objects and the extra jet is associated to the one of the remaining jets that has the larger p_T . The kinematic reconstruction of the $t\bar{t}$ + 1-jet events has been studied and optimized using the $t\bar{t}$ POWHEG+PYTHIA Monte Carlo sample with a $m_t = 172.5$ GeV.

5.5.1 Identification of the W bosons candidates

In the l +jets channel, one of the W bosons decays into a charged lepton plus a neutrino and the other into two light quarks that will create two light jets. For both W -bosons, the candidates are reconstructed as follows.

Leptonic W boson candidates The neutrino traverses the detector without leaving a signal. The transverse momentum imbalance (its magnitude is conventionally denoted as E_T^{miss}) of all reconstructed objects is assumed to be entirely due to the transverse momentum carried by the neutrino. The neutrino momentum is reconstructed

by imposing a W –mass constraint on the lepton- E_T^{miss} system:

$$m_W^{\text{leptonic}} = m_{\text{lepton}}^2 + 2(E_{\text{lepton}}E_\nu - p_{\text{lepton}} \cdot p_\nu) \equiv m_W^{\text{PDG}} \quad (5.2)$$

where p_a represents the momentum (p_x, p_y, p_z) of the particle a . Considering the neutrino mass as zero and associating the measured E_T^{miss} with the transverse momentum of the non-detected neutrino, the z –component of the neutrino three momentum (the longitudinal component) is extracted by solving the Eq. (5.2). The $p_{z,\nu}$ solution to this equation is a quadratic equation that yields two real solutions if the discriminant of the quadratic equation is greater than zero. If the discriminant is negative, the magnitude of the missing transverse energy is recalibrated to get a null discriminant.

Hadronic W boson candidates All the light jets that have not been identified as b –quark jets are considered as candidates to be decay products of the hadronic W boson. To reduce the number of possible pairings and to increase the quality of the kinematic reconstruction of the W boson candidate, only the pairs of light jets i, j that pass the following selection criteria are selected:

- $0.9 < \alpha < 1.25$, with α the W mass divided by di-jet mass m_{ij} ($\alpha \equiv m_W^{\text{PDG}}/m_{ij}$);
- $\Delta k_T^{ij} = \min(p_T^i, p_T^j) \cdot \Delta R_{ij} < 90 \text{ GeV}$

where $\Delta R_{ij} = \sqrt{\Delta\phi(i, j)^2 + \Delta\eta(i, j)^2}$.

5.5.2 Reconstruction of the $t\bar{t} + 1$ -jet system

Among all possible leptonic and hadronic- W candidates the best combination is chosen by minimizing the difference between the all possibilities for reconstructed kinematic masses (by considering all possible associations of the two b –jets with the W –boson candidates). For that, the β' variable is defined:

$$\beta' = \frac{m_t^{\text{leptonic}} - m_t^{\text{hadronic}}}{m_t^{\text{leptonic}} + m_t^{\text{hadronic}}} \quad (5.3)$$

where m_t^{leptonic} (m_t^{hadronic}) refers to the reconstructed kinematic mass of the candidate to be the top quark decaying leptonically (hadronically). All possible pairings of W boson candidates and identified b –quark jets are considered, and the one that minimizes the absolute value of the differences of kinematical masses, the β' variable, is selected. Once the objects that compose the $t\bar{t}$ system are chosen, the light jets that make up the hadronic W boson are corrected using the α value.

The additional jet that completes the $t\bar{t} + 1$ -jet system is selected among the remaining jets after all jets that are used to form the top quark candidates are discarded. The discarded jets include the two jets assigned to the hadronic W -boson candidate and two jets identified as b –quark jets. From the remaining jets, the leading- p_T jet is chosen. To classify the event as a $t\bar{t} + 1$ -jet event, a $p_T > 50 \text{ GeV}$ and $|\eta| < 2.5$ are required for the additional jet. Two softer cuts on the p_T of the additional jets,

$p_T > 30, 40$ GeV, have been also considered as a crosscheck. Lower cuts for the extra jet p_T translate into smaller statistical but larger systematic uncertainties for the top-quark mass extraction from the \mathcal{R} -distributions (see Section 6.7 for more a detailed discussion).

Finally, an extra cut to improve the signal-to-background ratio (in about 15%) is applied to the ratio of the reconstructed invariant masses of the leptonic and hadronic top quark candidates:

$$\beta = \frac{m_t^{\text{leptonic}}}{m_t^{\text{hadronic}}} > 0.9 \quad (5.4)$$

The results for the efficiency and signal-to-background ratio are summarized in Tab. 5.2. A cut of $\beta > 0.9$ is finally chosen as a compromise between the reduction of statistics and the improvement of signal-to-background ratio.

Cut	efficiency	(Data-BKG)/BKG
No cuts	1	15.3 ± 1.2
$\beta > 0.8$	0.8971	16.9 ± 1.4
$\beta > 0.9$	0.7472	17.8 ± 1.5
$1.1 > \beta > 0.9$	0.5455	21.5 ± 2.0

Table 5.2: Study of the impact of an optimization cut of the β variable. The efficiency is calculated as the ratio of events that pass the β cut, with respect to the number of reconstructed $t\bar{t}$ + 1-jet events without any extra cut in β .

5.5.3 Quality of the reconstructed events

The sets of cuts proposed in this chapter are optimized to obtain larger efficiencies and purities (good matching between the reconstructed objects and the same objects at parton level) and to reduce the combinatorial background and to minimize the effects due to jet energy corrections to the light jets during the reconstruction of $t\bar{t}$ + 1-jet events.

The efficiency of selection, defined as the ratio between the final number of selected events and the events that passed the basic selection, has been estimated to be 28 – 29% (the efficiency reaches values of $\sim 40\%$ if the p_T cut requirement for the extra jet is 30 GeV). A study of the quality of the reconstruction algorithm has been performed. For that, the matching of the reconstructed objects (light jets associated to the W boson, the b -tagged jets and the extra jet) with their correspondences at parton level (quarks from the W boson decay, b -quarks from the top quark decays and the hardest emission from the $t\bar{t}$ system) is studied. Two objects are considered to match if they are found to be in a cone $\Delta R < 0.4$. This exercise has been performed with the light jets associated to the W -boson and it is found that 39% of the times, the quarks at parton level match with the light jets. A similar exercise has been performed for the $t\bar{t}$ + 1-jet system. The percentage of reconstructed $t\bar{t}$ + 1-jet where all the

jets are matched with the correct partons is 25%. When reconstructing the $t\bar{t}$ + 1-jet as a whole system, the matching criteria allows multiple combinatorics: the system $t\bar{t}$ + 1-jet is considered to be well reconstructed if all its reconstructed jets match with any of the original partons having all partons at least one reconstructed match. The percentage of reconstructed $t\bar{t}$ + 1-jet matched to the parton level, in this case, is 41%. Similar values are obtained, for example, in Ref. [102], for the reconstruction of $t\bar{t}$ events.

5.6 Reconstructed $t\bar{t}$ +1-jet events

The selection of the $t\bar{t}$ + 1-jet sample leads to the event yield displayed in Tab. 5.3. The results are shown separately for the l -jets channels. For the signal and background estimations, the statistical and systematic uncertainties as quoted in Section 5.2.1 are evaluated. The observed number of events is within the error in agreement with the expectation.

	events	stat	syst
Data	2256	-	-
signal	2053 (91.0%)	45	316
W +jets	31(1.4%)	6	15
Z +jets	6(0.3%)	2	3
Single top	62(2.7%)	8	33
WW , ZZ , WZ	1(0.1%)	1	0
Multi-jet	22(1.0%)	5	12
Total Background	121(5.4%)	11	38
Total Predicted	2174	47	318
(data-B) / B	17.7	0.8	2.9

Table 5.3: Similar to Tab. 5.1, but performed after the final selection after $t\bar{t}$ + 1-jet reconstruction.

The observed distributions for a number of variables after applying all analysis cuts are compared to the Standard Model template in Figures 5.3 to 5.4.

Finally, the center-of-mass energy p_s of the $t\bar{t}$ + 1-jet system is reconstructed by summing the four-vectors of the charged lepton, neutrino and the jets. Note that this observable is robust against ambiguities in the combinatorics. In particular, the reconstructed p_s does not depend on the assignment of the two b -jets to the leptonic and hadronic top quark candidates. In Fig. 5.5, the detector-level p_s distribution is shown before (uppermost figure) and after (lowermost figure) the background subtraction and normalization.

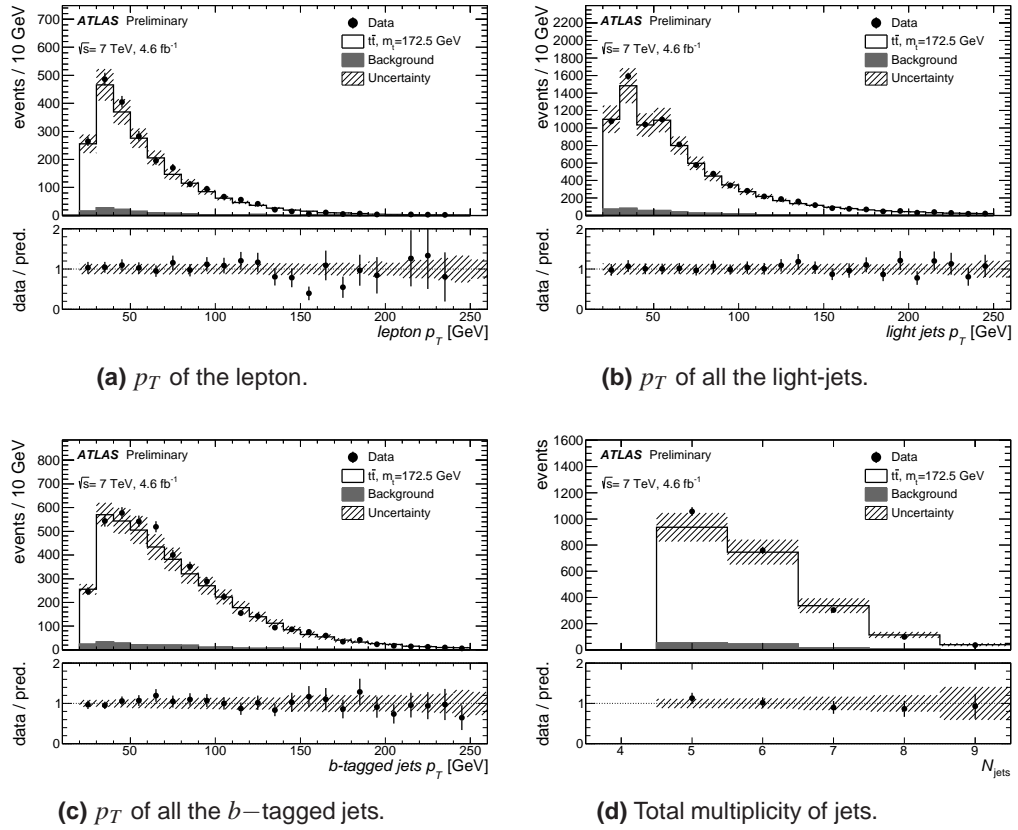


Figure 5.3: The data for different kinematic distributions are compared to the $t\bar{t}$ @NLO+PS calculations (POWHEG+PYTHIA) with an assumed Monte Carlo mass $m_t = 172.5$ GeV after the final kinematic reconstruction of the $t\bar{t}$ + 1-jet events. The background and the uncertainties are evaluated as in Figures 5.1 and 5.2.

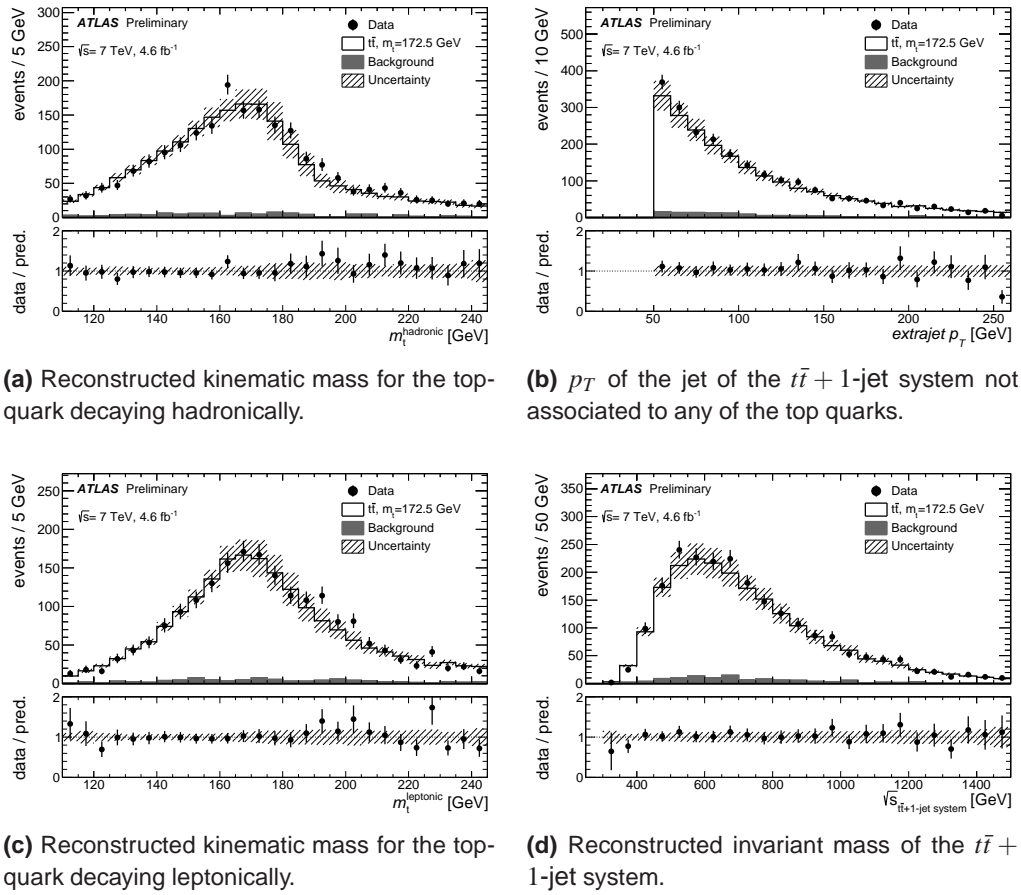
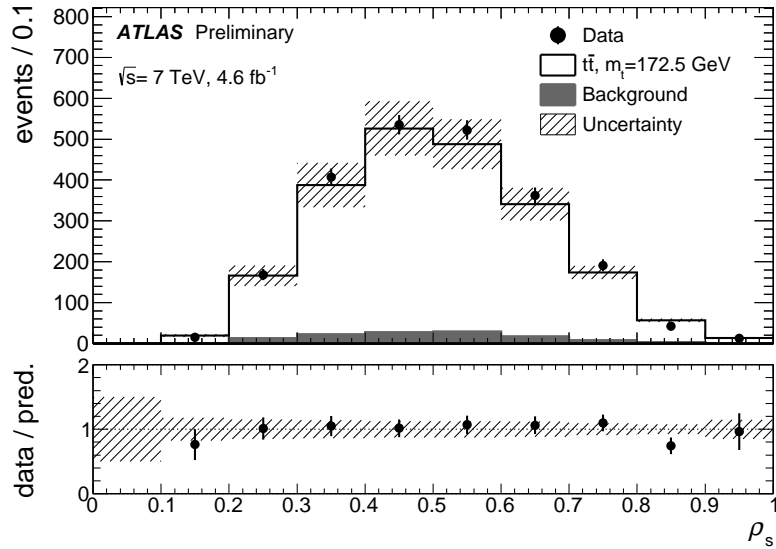
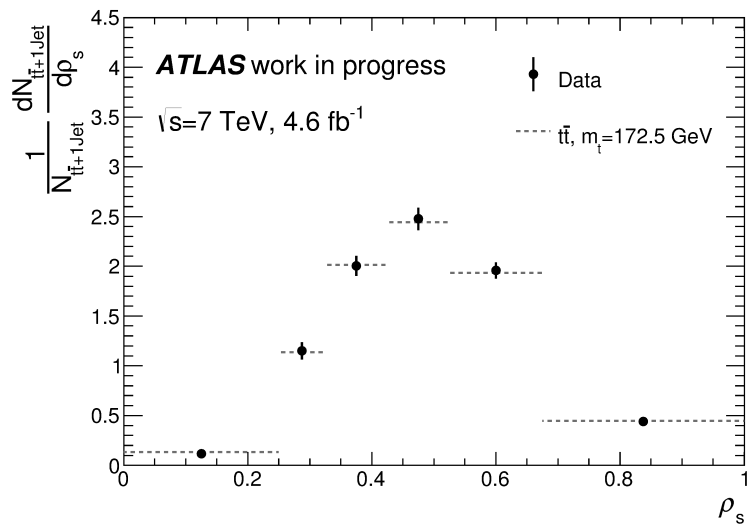


Figure 5.4: Similar to Figure 5.3.



(a) Reconstructed ρ_s distribution compared with signal and background estimations in the same way than in Figure 5.3.



(b) The differential and normalized ρ_s distribution of reconstructed $t\bar{t}$ + 1-jet events at the detector level after the background subtraction.

Figure 5.5: Reconstructed ρ_s distribution before and after background subtraction and normalization. In both cases data are compared to the $t\bar{t}$ @NLO+PS calculations (POWHEG+PYTHIA) with an assumed Monte Carlo masses of $m_t = 172.5$ GeV.

6

Experimental determination of the top-quark pole mass.

The first top-quark pole mass extraction from $t\bar{t} + 1$ -jet events collected by the ATLAS detector is presented in this chapter.

The definition of the $t\bar{t} + 1$ -jet system at the level in which the top-quark mass is extracted is presented in Section 6.1. The unfolding procedure that corrects for the effects of top-quark decay and the finite detector acceptance and resolution is explained in Section 6.2. The extraction of the top-quark pole mass by fitting the observed \mathcal{R} -distribution to the prediction of the $t\bar{t} + 1$ -jet @NLO+PS calculations with POWHEG+PYTHIA is discussed in Section 6.3. The study of the independence of the unfolding procedure on the Monte Carlo mass is presented and discussed in Section 6.4. Other important cross checks of the unfolding procedure are presented in Section 6.5. The uncertainties associated to the top-quark pole mass extraction are summarized in Section 6.6 and the final results are shown in Section 6.7.

6.1 The $t\bar{t} + 1$ -jet system at parton level.

To enable the comparison of the data with respect to the NLO+PS calculation the reconstructed number of events as a function of ρ_s (lowermost plot in Figure 5.4) is corrected, after the background subtraction, for detector effects as well as for particle decays and hadronization effects. Finally, it is normalized. Before starting with the correction algorithm, the following definitions of the $t\bar{t} + 1$ -jet system are introduced:

1. **Parton level:** the top and anti-top quarks are produced on-shell before decaying but QCD radiation including initial (ISR) and final state (FSR) radiation are enabled. This is the level where the corrected data is compared to the theoretical calculation to extract the m_t^{pole} parameter. Parton shower evolution is included at this level. The corresponding theoretical approach is identified as

$t\bar{t} + 1\text{-jet}$ @NLO+PS, as defined in Chapter 3. It is important to remember the result shown in Chapter 3 that shows that the \mathcal{R} calculations from $t\bar{t} + 1\text{-jet}$ @NLO+PS or only NLO are compatible within the scale uncertainties. Moreover, the difference of extracting the m_t^{pole} from a measured \mathcal{R} distribution using one or the other calculation is ~ 0.3 GeV.

2. **Particle level:** based on stable particles before they enter the detector simulation. A measurement of the p_s distribution of $t\bar{t} + 1\text{-jet}$ events at this level is foreseen in a future iteration of this analysis, including the 8 TeV data.
3. **Reco level (or detector level):** the $t\bar{t} + 1\text{-jet}$ events are reconstructed from the detector information as described in Section 5.5. At this level ATLAS MC events and data are compared. Figure 5.5 shows the \mathcal{R} -distribution at this level.

It should be noticed that in all cases the same reconstruction algorithm is applied to define the jets, that is, the anti- k_r algorithm with radius parameter $R = 0.4$ with the same kinematic cuts ($p_T(\text{jet}) > 50$ GeV and $|\eta(\text{jet})| < 2.5$).

6.2 Unfolding procedure

For this analysis it is crucial to use an unfolding procedure (to correct the influence of the decay, hadronization and detector effects) which does not depend on the mass of the Monte Carlo sample used to define the procedure. For that, different unfolding approaches have been considered and studied during the development of the analysis.

It has been observed that a simple bin-by-bin correction cannot be applied without introducing a dependence on the mass used in the modeling of the signal since the endpoint of the \mathcal{R} distribution depends on the top-quark mass. The first method that was proposed to unfold the data, presented in Ref. [11], was based on the shape of the \mathcal{R} distribution. For that a change of variable is introduced and the correction factors are calculated for this intermediate variable instead of being based on p_s . The new variable was chosen to be sensitive to the shape of the distribution making the correction independent of the endpoint of the distribution itself. More precisely, this variable was defined as a function of the integral of the p_s and the correction factors calculated were proved to be independent of the mass used in the Monte Carlo sample for the top-quark mass interval of $m_t = 160 - 180$ GeV. This approach was not finally used in the present analysis since it needs a lot of statistics to give stable solutions. More details about this method are shown in the Appendix A.

The second approach, and the one finally used in the experimental measurement, is based on a regularized inversion of a migration matrix. This unfolding procedure uses response matrices that better account for the correlations between parton and reconstructed level migrations. The inversion of the matrix is performed using a regularized algorithm that minimizes the statistical fluctuations. This method, as it is shown in Section 6.4, is also independent of the Monte Carlo mass used in its definition.

The response matrix accounts for the migration in ρ_s of the events between the parton level and the reconstructed level. As the parton level as defined in the first section of this chapter is not accessible in the default ATLAS MC sample, an additional intermediate level is introduced:

- **POWHEG 1st emission level:** the \mathcal{R} observable is defined using the top quarks before decay and after QCD radiation (ISR or FSR) as before. The additional jet is identified with the first emission in POWHEG¹.

The strategy of this analysis is to correct the data up to the 1st POWHEG emission level using standard ATLAS MC samples. An additional correction is then needed from POWHEG 1st emission level to the parton level. This correction is determined using event samples generated with the same ATLAS POWHEG version and tuning, but including the information needed to define the $t\bar{t} + 1$ -jet as required by the parton level. These samples have been validated using the ATLAS procedure and the results are shown in Appendix F where a comparison between several key distributions in the official and private samples is shown.

Using the nominal $t\bar{t}$ Monte Carlo samples, the migration matrix is constructed. This migration matrix — defined as \mathcal{M} — contain the migrations from the first POWHEG emission level to the reconstructed level for l +jets events. The migration matrix is constructed with simulated events that pass the selection cuts at the POWHEG first emission and at the reconstructed level. This correction is performed by a regularized inversion of the migration matrix using the Singular Value Decomposition (SVD) method [?]. The regularization minimizes the large statistical fluctuations that can appear when directly inverting the matrix. The same procedure is used routinely in the ATLAS top group, for instance in reference [?]. Thus the data correction to the POWHEG 1st emission level can be expressed using the following formula that describes the unfolding of a normalized differential cross section:

$$\mathcal{R}^{\text{1st Emission}}(\rho_{s,j}) \equiv \frac{1}{\Delta(\rho_{s,j})} \frac{\sum_i \mathcal{M}_{ji}^{-1} [D_i - B_i]}{N \epsilon(\rho_{s,j})} \quad (6.1)$$

where in our case $\mathcal{R}^{\text{1st Emission}}(\rho_{s,j})$ is the \mathcal{R} -distribution defined at the 1st POWHEG emission level evaluated in the j -th interval of ρ_s (the j -th bin); $\Delta(\rho_{s,j})$ is the width of the ρ_s j -th bin; \mathcal{M}_{ji}^{-1} are the matrix elements connecting the \mathcal{R} -distribution at reconstruction level to the 1st POWHEG emission level as calculated using simulated data and corresponding only to the selected sample; D_i is the observed \mathcal{R} -distribution in data after selection; B_i the number of background events in the i -th bin and N is the total number of events, obtained by summing up the distribution for all the bins; finally, $\epsilon(\rho_{s,j})$ is the factor which takes into account the correction of the POWHEG first emission \mathcal{R} -distribution due to the event selection. The $\epsilon(\rho_{s,j})$ correction factor

¹In the matching procedure of the POWHEG matrix element with the PYTHIA parton shower the hardest (ISR and FSR) emission is taken care of by POWHEG. For both initial- and final-state radiation, the parton showers are started at the kinematical limit, and emissions above the POWHEG scale (emissions in the parton shower that are harder than the first emission) are vetoed. For a detailed physics discussion, see R. Corke and T. Sjostrand [?]

is evaluated as the ratio of the POWHEG first emission \mathcal{R} distribution before and after applying the event selection and it also accounts for the fraction of events (approximately 15%) in which the POWHEG first emission level does not satisfy the selection requirements ($p_T > 50$ GeV and $|\eta| < 2.5$) but the event is finally reconstructed as $t\bar{t} + 1$ -jet event.

A further bin-by-bin unfolding is applied to correct the POWHEG first emission level to the partonic level:

$$\mathcal{R}^{\text{partonic}}(\rho_{s,j}) \equiv \tau(\rho_{s,j}) \cdot \mathcal{R}^{\text{1st Emission}}(\rho_{s,j}) \quad (6.2)$$

This second correction, $\tau(\rho_s)$, is determined as the ratio between the parton level spectra and the POWHEG emission spectra before the event selection as defined in the theoretical calculation to compare with. This second correction is numerically of relatively minor importance. The bin-by-bin correction is typically of the order 5%. In terms of the top-quark pole mass the full correction accounts for approximately a 1% change.

The expression that summarizes the total correction is:

$$\mathcal{R}^{\text{partonic}}(\rho_{s,j}) \equiv \tau(\rho_{s,j}) \cdot \frac{1}{\Delta(\rho_{s,j})} \frac{\sum_i \mathcal{M}_{ji}^{-1} [D_i - B_i]}{N\epsilon(\rho_{s,j})} \quad (6.3)$$

The response matrix and the two correction factors are shown in Figures 6.1 and 6.2. The choice of the bin size aims to:

- isolate the region where the distribution is more sensitive on the mass, keeping the purity the migrations in this bin as small as possible;
- isolate the region where the normalized curves for different top-quark masses cross and the sensitivity is therefore very poor ($0.525 < \rho_s < 0.675$);
- maximize the number of events in the diagonal of both matrices, having a minimum of 50% of efficiency for each bin in the diagonal.

In Figure 6.1 the diagonal elements of the matrices all exceed 50%, showing that the efficiency condition is indeed met. Specifically, the ρ_s -interval where the \mathcal{R} -distribution is most sensitive to the top-quark mass (large values of ρ_s), presents a large efficiency of 74%.

The statistical uncertainty of the corrected result is evaluated as follows. Pseudo-experiments are created by varying the \mathcal{R} data points within their statistical uncertainty. The pseudo-data sets created in this way are also unfolded with the nominal migration matrix, to propagate the statistical uncertainty of the data to the corrected distribution. The (small) uncertainty in the response matrix due to the limited Monte Carlo statistics is propagated in a similar way, but in this case the data is kept fix and a set of pseudo migration matrices is created according to the statistical uncertainty of the original migration matrix. A set of corrected pseudo-distributions is obtained. Comparing these distributions with the nominal one, the covariance matrix V that mea-

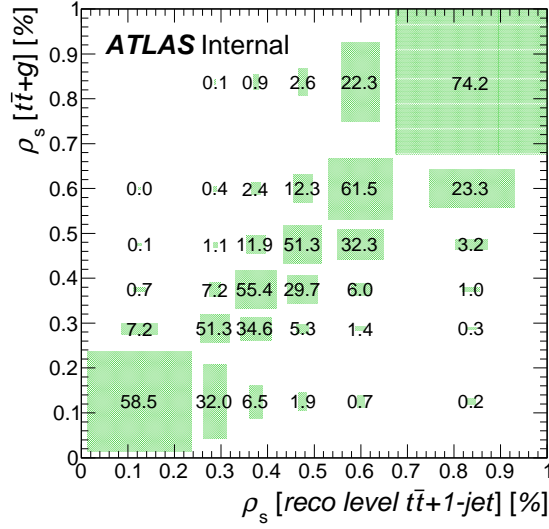


Figure 6.1: The response matrix mapping the reconstructed ρ_s on the POWHEG first emission (where the g corresponds to the POWHEG emission) for lepton+jets events. The efficiency of the diagonal elements is always greater than 50%.

sures the statistical uncertainties of the corrected data is obtained. The covariance matrix V is presented in Appendix B.

6.3 Fit to $t\bar{t} + 1\text{-jet}$ @NLO+PS

To extract the m_t^{pole} from the unfolded \mathcal{R} -distribution, the corrected distribution is fit with the $t\bar{t} + 1\text{-jet}$ NLO+PS calculation using the least square method. The χ^2 to fit to binned data is defined as follows:

$$\chi^2 = \sum_{ij} (\mathcal{R}_i - f_i(m_t^{\text{pole}})) V_{ij}^{-1} (\mathcal{R}_j - f_j(m_t^{\text{pole}})) \quad (6.4)$$

where \mathcal{R}_i is the data corrected measurement in bin i , f_i is the predicted result and V^{-1} is the inverse of the regularized covariance matrix of the unfolded \mathcal{R} -distribution, obtained as described in Section 6.2. The dependence of the prediction $f(m_t^{\text{pole}})$ on the top-quark pole mass is a parametrization of the results in Table 6.1 of the NLO + PS calculation for the $t\bar{t} + 1\text{-jet}$ cross section. The result of a polynomial of second order parametrization is shown in Figure 6.3 (different choices are compared in Appendix C)

The measured m_t^{pole} is the one which minimizes the χ^2 of Eq. (6.4). Its statistical uncertainty is taken as the mass shift that increases the χ^2 by one unit with respect to the minimum ($\Delta\chi^2 = +1$).

In the normalized \mathcal{R} distribution the six bins are no longer independent. The re-

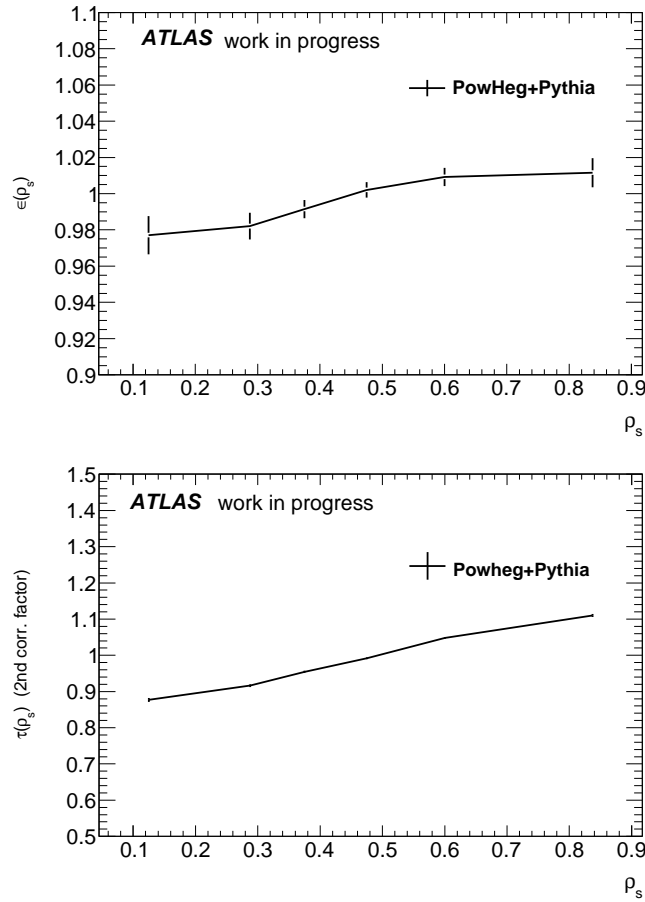


Figure 6.2: First figure: the relative selection efficiency factor, $\epsilon(\rho_s)$. Second figure: the second correction factor $\tau(\rho_s)$.

duced number of degrees of freedom is accounted for by discarding the least sensitive bin in the fit. The effect of dropping one or other bin has been performed observing a standard deviation of the extracted mass of 0.4 GeV and the χ^2 value is kept constant in a window of the $\sim 18\%$ around the nominal value. The naive statistical combination of the top-quark mass values of each bin gives a difference of 0.3 GeV with respect to the obtained by the χ^2 minimization.

6.4 Independence of the unfolding procedure with the Monte Carlo mass.

An important feature to check for this analysis is that the unfolding procedure is independent of the assumed input top-quark mass of the Monte Carlo generator. For this purpose, two different tests have been performed. The first one consist in the

ρ_s	$\mathcal{R}(\rho_s)$					
	m_t^{pole}	170 GeV	172.5 GeV	175 GeV	177.5 GeV	180 GeV
0 to 0.25		0.1327(9)	0.139(4)	0.1425(8)	0.149(1)	0.1548(6)
0.25 to 0.325		1.10(1)	1.134(6)	1.17(1)	1.21(1)	1.251(9)
0.325 to 0.425		1.972(9)	2.027(4)	2.070(9)	2.13(1)	2.185(7)
0.425 to 0.525		2.51(1)	2.561(6)	2.59(1)	2.64(1)	2.674(8)
0.525 to 0.675		2.143(8)	2.125(4)	2.117(7)	2.085(9)	2.060(6)
0.675 to 1.0		0.353(2)	0.316(1)	0.287(2)	0.252(2)	0.223(1)

Table 6.1: The \mathcal{R} -distribution calculated using $t\bar{t} + 1\text{-jet}$ @NLO+PS generated samples for different m_t^{pole} values. The extra jet requirements are $p_T \geq 50$ GeV and $|\eta| \leq 2.5$. The quoted uncertainties reflect the statistical accuracy of the calculation.

unfolding of the data using different Monte Carlo samples to define the unfolding, each one with different top-quark mass as input. The second one consist in applying a fixed unfolding procedure (defined with $m_t = 172.5$ GeV) to different \mathcal{R} distribution simulated with $t\bar{t}$ Monte Carlo samples with different top-quark mass inputs. The statistical uncertainty of the tests performed in the second case is much lower than in the other case, since the number of events in the Monte Carlo samples are larger than in the data samples.

From both tests, the non-dependence of the top-quark mass measurement with the Monte Carlo mass used for the unfolding is inferred.

Unfolding procedure defined with different $t\bar{t}$ samples (with different m_t values) and applied to the data sample.

The data is unfolded with different Monte Carlo samples for $t\bar{t}$ with input masses in the interval $170 \text{ GeV} \leq m_t \leq 180 \text{ GeV}$.

The unfolded \mathcal{R} distributions are shown for four ρ_s bins (the bins in the interval $0.25 < \rho_s < 0.525$ are joint together to increase the statistical resolution and to reduce the fluctuations) in Figure 6.4 as blue points. The \mathcal{R} dependence on the Monte Carlo mass used during the unfolding is compatible, in all bins with a line with zero slope. The red band contains the total statistical uncertainty (due to the number of reconstructed events and to the finite size of the response matrix) for the data unfolded with the nominal $t\bar{t}$ simulations. The error bars in the blue points accounts only for the statistical uncertainty due to the finite number of events of the correspondent response matrix. These errors are not correlated for the different points. At the same time, in the figure, the \mathcal{R} dependence on the m_t^{pole} for $t\bar{t} + 1\text{-jet}$ @NLO+PS calculations is shown (black points), together with its parametrization as a second degree polynomial. In this figure is observed that the value of the unfolded \mathcal{R} distribution does not depends

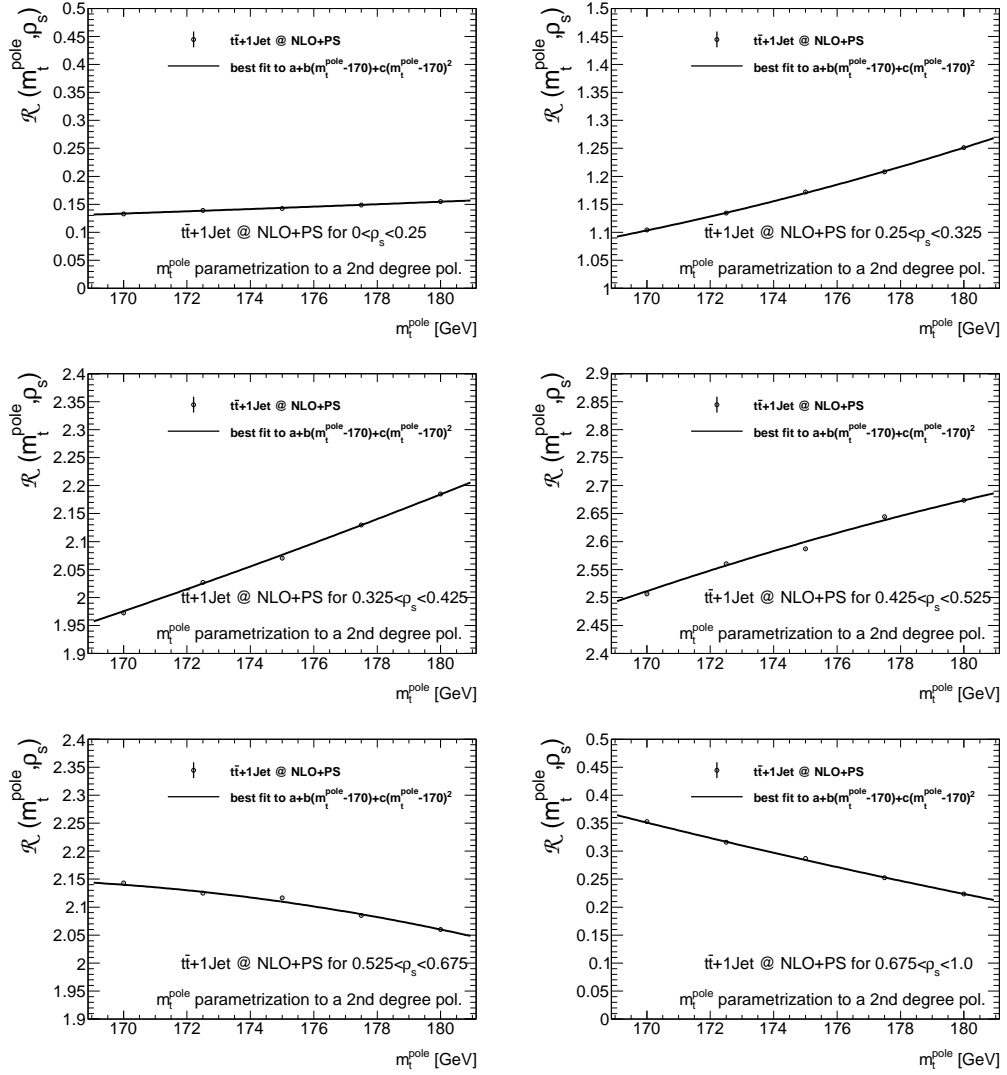


Figure 6.3: Parametrization of the \mathcal{R}_t mass dependence using a polynomial of degree 1: $\mathcal{R}_t(m_t^{\text{pole}}) = a + b(m_t^{\text{pole}} - 170)$ for the six different p_s intervals. Notice that the same $\Delta \mathcal{R}_t$ is shown in the six y-axis.

on the Monte Carlo mass, specially in the most sensitive bins. A remnant dependence in the region of lowest p_s values is observed. The mass resolution in this interval is small, and it does not affect the result.

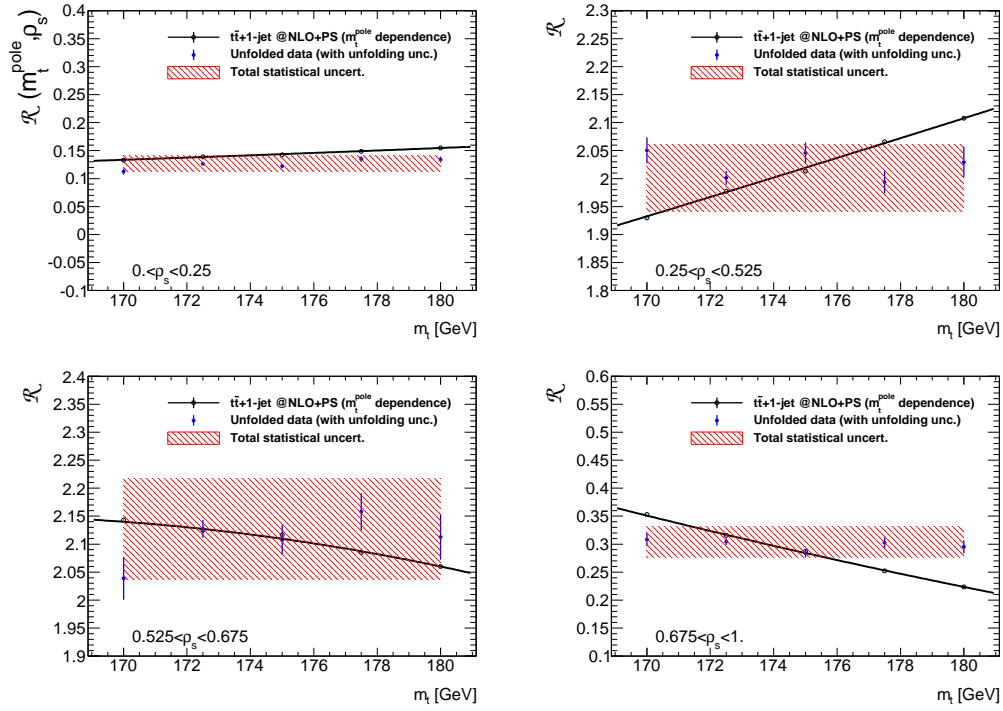


Figure 6.4: The dependence of the unfolded \mathcal{R} distribution on the Monte Carlo top-quark mass. The error bars of the blue points represents the statistical uncertainty associated to the migration matrix and the red bands contain the full statistical uncertainty (migration matrix and data number of events) for the unfolded \mathcal{R} distribution with the nominal Monte Carlo sample ($m_t = 172.5$ GeV). The bins in the $0.25 < p_s < 0.525$ have been added up to increase the resolution for the given statistical uncertainty. For completeness, the theoretical dependence of the \mathcal{R} distribution on m_t^{pole} is shown as the black points. The m_t^{pole} theoretical dependence is parametrized with a second polynomial (black line).

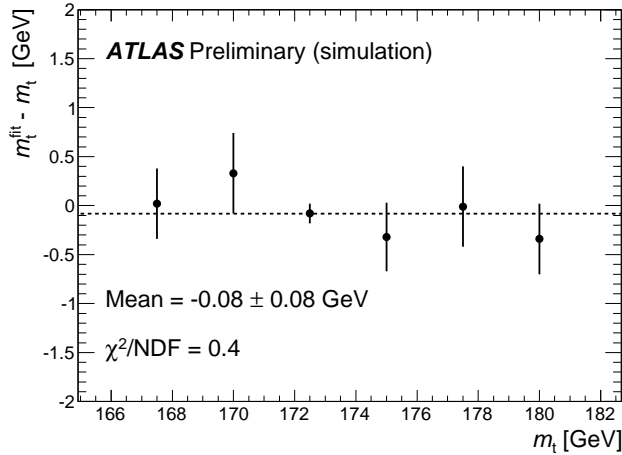


Figure 6.5: The difference between the fitted mass and the top-quark Monte Carlo mass for input spectra generated with POWHEG+PYTHIA and unfolded with the nominal procedure (with fixed $m_t = 172.5$ GeV). The fit is performed with a $t\bar{t}$ @NLO+PS calculation.

Unfolding procedure defined with a common Monte Carlo sample and applied to different $t\bar{t}$ Monte Carlo samples.

The default unfolding procedure is repeated for simulated data using $t\bar{t}$ @NLO POWHEG+PYTHIA Monte Carlo samples with input masses in the interval $167.5 \text{ GeV} \leq m_t \leq 180 \text{ GeV}$, that spans over 15 standard deviations of the most precise determination. The corrected \mathcal{R} -distributions are then fit with the $t\bar{t}$ @NLO+PS calculation (contrary to nominal mass extraction, where the $t\bar{t} + 1$ -jet calculation is used) and the Monte Carlo mass is extracted. In this case it is expected that the fit yields the MC mass assumed in the Monte Carlo sample.

The black points with error bars in Figure 6.5 correspond to the difference between input mass and extracted result for fits of the data unfolded with an input Monte Carlo mass ranging from 167.5 GeV to 180 GeV. All individual results are compatible with 0 within their statistical error (which largest value is approximately 400 MeV). A fit to the points with a first order polynomial yields a slope of 0.02 ± 0.03 , compatible with no dependence on the input Monte Carlo mass within this mass interval.

It is concluded, therefore, that in the interval from 167.5 GeV to 180 GeV and within the statistical uncertainty of our estimation there is no dependence on the assumed Monte Carlo mass.

6.5 Additional cross checks for the unfolding procedure.

Statistical stability of the unfolding procedure.

The matrix unfolding that corrects for detector effects and hadronization is performed by a regularized inversion of the migration matrix using the Singular Value Decomposition (SVD) method [?]. The regularization minimizes the large statistical fluctuations that can appear when the matrix is inverted directly. The regularization of the unfolding is determined by a parameter called *kreg* and the guidelines explained in [?] have been followed to chose its optimal value which has been evaluated to be equal to 5. The unfolded \mathcal{R} -distribution with this optimal *kreg* corresponds to $m_t^{\text{pole}}(l + jets) = 173.7 \pm 1.5$ (stats) GeV. Variations of this *kreg* value of +1 and -1 have also been studied ranging to results of m_t^{pole} within 0.3 GeV.

To crosscheck the consistency of the above results a further test has been performed using pseudodata experiments. A total of 5000 pseudodata \mathcal{R} -sets have been generated around the measured values of the \mathcal{R} -distribution assuming Gaussian statistical errors. For each of these \mathcal{R} -sets the whole unfolding process has been applied and the resulting top-quark mass (m_i) has been compared to that extracted using real data with *kreg* equal to 5. The difference has then been divided by the obtained statistical error (σ_i^m) according to the following formula:

$$P_i = \frac{m_i - m_t^{\text{pole}}(\text{data})}{\sigma_i^m} \quad (6.5)$$

The pull distribution P thus obtained is shown in Figure 6.6. A fit of P to a Gaussian distribution gives a mean value of 0.017 ± 0.012 and a standard deviation of 0.95 ± 0.01 .

Stability of the unfolding procedure with the numbers of steps: two-step unfolding vs one-step unfolding.

The two-step unfolding procedure is scrutinized using POWHEG+PS with the HERWIG parton shower model. In the ATLAS POWHEG+HERWIG samples the information needed to define the $t\bar{t} + 1\text{-jet}$ system at the parton level is available. Thus, we can correct the data directly to the parton level and compare the result to that obtained using the two-step procedure (i.e. through the POWHEG 1st emission level as in the nominal procedure). The results are compatible within 0.1 GeV and with a statistical accuracy of ~ 0.25 GeV.

6.6 Statistic and systematic uncertainties

In this Section the treatment of the uncertainties that affect the extraction of the top-quark pole mass is discussed. The statistical uncertainty of the corrected result is

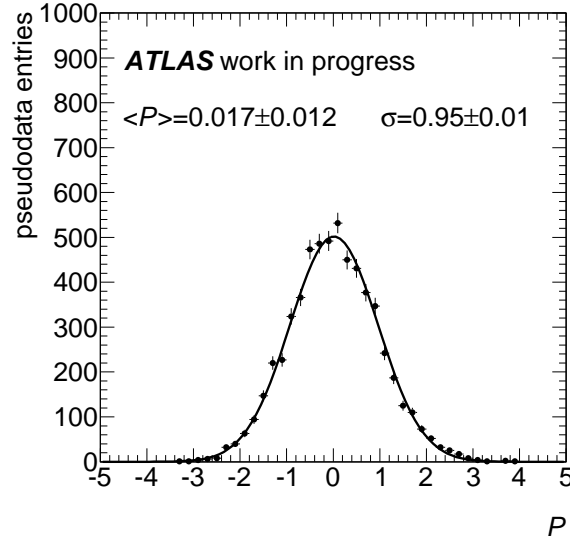


Figure 6.6: Pull distribution evaluated for $k_{reg}=5$.

evaluated by repeating the unfolding procedure on pseudo-experiments corresponding to variations of the \mathcal{R} data points within their statistical uncertainty. The (small) uncertainty due to the limited number of Monte Carlo events used to define the unfolding procedure is evaluated by varying the migration matrices within the statistical uncertainties. It amounts in 0.13 GeV and it is accounted for as a systematic uncertainty. The remaining systematic uncertainties are split in two categories different categories: theoretical uncertainties (Section 6.6.1) and the experimental uncertainties. The experimental uncertainties are divided in: signal- and detector-modeling uncertainties (Section 6.6.3 and 6.6.2) and the background estimation uncertainties (Section 6.6.4).

6.6.1 Theoretical uncertainties

Uncalculated higher orders: an important asset of the top-quark pole mass extraction method followed here is that it allows for a determination of the theoretical uncertainty due to the truncation of the perturbative expansion of the $t\bar{t} + 1$ -jet calculation at NLO. The scale uncertainty on the differential cross-section is evaluated using the conventional procedure. The variation in the extracted top-quark mass is recorded when the corrected data are fitted with NLO+PS calculations performed with factorization and renormalization scales of twice and half the nominal scale ($\mu = 2m_t^{\text{pole}}$, $\mu = m_t^{\text{pole}}/2$).

The alternative choices for the scale lead to a 0.44 GeV lower value for the top-quark pole mass for $\mu = 2m_t^{\text{pole}}$ and a 0.93 GeV higher value for $\mu = m_t^{\text{pole}}/2$. The same uncertainty (obtained on the sum of the electron and muon channels) is assigned also to the individual channels. As a cross-check the impact of the scale

variation in the fit is determined for several Monte Carlo input samples with a Monte Carlo mass in the range 172.5-177.5 GeV. The results are in good agreement with the quoted uncertainty.

PDF and α_s choice: the uncertainty on the proton PDF and on the value of the strong coupling constant α_s used in the $t\bar{t} + 1$ -jet calculation is propagated by repeating a fit to different \mathcal{R} distributions implemented with $t\bar{t} + 1$ -jet NLO+PS calculations which use different PDF sets and α_s values. These PDF sets and α_s values are varied at the same time and are:

- the nominal CT10 PDF set, with $\alpha_s(M_Z) = 0.118$;
- the MSTW2008nlo90cl PDF set, with $\alpha_s(M_Z) = 0.120$;
- the NNPDF PDF set, with $\alpha_s(M_Z) = 0.119$

The theory uncertainty due to PDF and α_s is taken as half of the maximum difference in the resulting top-quark pole mass: $\sigma(m_t^{\text{pole}})(PDF + \alpha_s) = 0.21$ GeV.

The impact of varying only the α_s has been also estimated and found to be very small, $\sigma(m_t^{\text{pole}})(\alpha_s) = 0.01$ GeV, since the dependency of \mathcal{R} on α_s is almost canceled in the ratio. To make this exercise, a variation of $\Delta\alpha_s = 0.002$ is taken which is the maximum difference between the α_s values used by the different PDF groups.

The total theory error is the quadratic sum of the contributions of uncalculated higher orders and the PDF and α_s uncertainties: $\sigma(m_t^{\text{pole}})(\text{theory}) = (-0.49, +0.95)$.

6.6.2 Detector modeling

The impact of uncertainties in the reconstruction efficiency and energy measurement of basic reconstructed objects (leptons, E_T^{miss} and jets) is propagated to the value of the top-quark mass. Variations of all these quantities within their uncertainty are applied to the nominal Monte Carlo sample. The result of unfolding these alternative input spectra with the nominal POWHEG+PYTHIA response matrix is fed into the top-quark mass fit. Half of the difference between the upward and downward variations is taken as the systematic uncertainty.

The largest uncertainties associated to the detector modeling are the JES (including the b JES) and the b -tagging efficiency. For these cases, the uncertainty in the \mathcal{R} distribution, evaluated as the difference between the up and down variations divided by two is shown in Figures 6.7 and 6.8

Jet energy scale (JES) and b -jet energy scale (b JES): to estimate the impact of the jet energy scale uncertainty on the result, the jet energy is scaled up and down within its uncertainty for twenty-one uncorrelated components (called nuisance parameters) which are considered separately [104?]. Their impact on the precision of the mass measurement is presented in Table 6.2. A separate uncertainty is assigned to b -quark jets (labeled b JES) that is uncorrelated with the JES. The JES is the experimental source of uncertainty with the largest impact on the precision of the mass

measurement: the uncertainty on the top-quark mass amounts to 0.94 GeV. The details of the effect of these variations in the \mathcal{R} distribution can be seen in Fig. 6.7. The first figure shows the total JES uncertainty calculated as the addition in quadrature of all the uncorrelated uncertainties, except the b -JES, which is shown in the second figure. The third figure shows the addition in quadrature of both previous results.

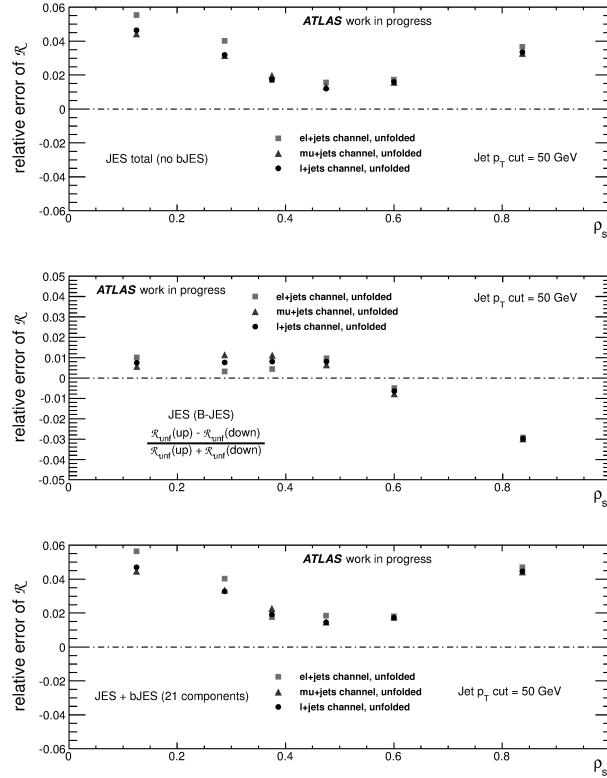


Figure 6.7: Impact of the different JES component's uncertainties on the \mathcal{R} distribution. The first plot shows the impact of the uncertainty of all the JES uncorrelated components on the \mathcal{R} distribution. The second shows only the impact of the b -JES uncertainty. The third one is the quadratic sum of both. The results for the three channels are included for completeness.

Jet energy resolution (JER) and jet reconstruction efficiency (JEFF): the effect of the uncertainty on the jet energy resolution is evaluated by smearing, before the event selection, the energy of the jets by a Gaussian distribution with a width chosen in agreement with the jet energy resolution uncertainty [?]. The corresponding uncertainty in the top-quark pole mass is 0.02 GeV. The JEFF is evaluated by randomly discarding a fraction of jets from the events before the selection (see Ref. [?]). This variation has a small impact (less than 0.05 GeV) on the top-quark mass.

Component	Uncertainty [GeV]
Statistical	0.31
<i>Statistical NP1</i>	0.30
<i>Statistical NP2</i>	0.03
<i>Statistical NP3</i>	0.05
<i>Eta intercalibration (statistical)</i>	0.05
Modeling	0.46
<i>Modeling NP1</i>	0.18
<i>Modeling NP2</i>	0.13
<i>Modeling NP3</i>	0.15
<i>Modeling NP4</i>	0.03
<i>Eta intercalibration (modeling)</i>	0.41
Detector	0.42
<i>Detector NP1</i>	0.42
<i>Detector NP2</i>	0.00
Mixed	0.06
<i>Mixed NP1</i>	0.02
<i>Mixed NP2</i>	0.06
Single particle high p_T	0.00
Relative non-closure MC	0.06
Pile-up offset	0.03
<i>Pile – up offset (NPV term)</i>	0.01
<i>Pile – up offset (μ term)</i>	0.03
Close-by jets	0.02
Flavor	0.16
<i>Flavor composition</i>	0.14
<i>Flavor response</i>	0.08
bJES uncertainty	0.58
Total (without bJes uncertainty)	0.74

Table 6.2: Detailed breakdown of the components of the JES uncertainty.

b -tagging efficiency (BTAG): the corrections that account for differences in the b -tagging efficiency and c -jet and light-jet mistag rates in data and simulation (derived from data including $t\bar{t}$, dependent on the p_T and η) are varied within their uncertainties (see Ref. [105]). The method, called eigenvector method, is based on varying each source of uncertainty by $\pm 1\sigma$, and considering its effect on the scale factor calibration (this discussion is relevant for the MC efficiencies, where only MC statistical uncertainties are implemented) in each bin used for the calibration. A breakdown of the impact of each component is presented in Table 6.3. The total uncertainty in the top-quark mass measurement due to uncertainties related to b -tagging amounts to 0.17 GeV. The estimated b -tagging uncertainty in the \mathcal{R} distribution is shown in Fig. 6.8.

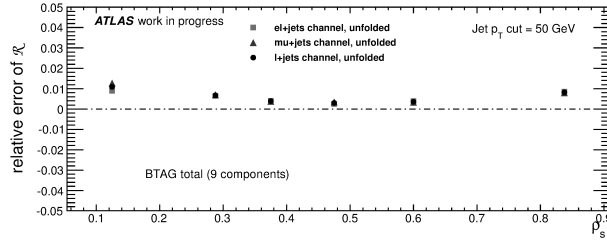


Figure 6.8: Impact of b -tagging efficiency on the \mathcal{R} distribution. The results for the three channels are included for completeness.

Component	Uncertainty [GeV]
b-tagging	0.17
<i>BREAK0 component</i>	-0.02
<i>BREAK1 component</i>	0.04
<i>BREAK2 component</i>	0.01
<i>BREAK3 component</i>	-0.02
<i>BREAK4 component</i>	-0.08
<i>BREAK5 component</i>	0.09
<i>BREAK6 component</i>	0.07
<i>BREAK7 component</i>	-0.09
<i>BREAK8 component</i>	-0.02
c-tagging	0.01
mistagging rates	0.03
Total	0.17

Table 6.3: Details of the different contributions of the BTAG, the CTAG and the mistag uncertainties. The mistag uncertainties are shown after the quadratic sum of all of them, as they are found to be very small.

Lepton identification and lepton energy resolution: the correction factors that account for the efficiencies of lepton identification are measured in data using Z and W decays. For the measurement of the lepton energy or momentum scale uncertainties, a similar procedure is used. The uncertainties are propagated to the top-quark mass, yielding a minor uncertainty of 0.03 GeV.

Modeling of the E_T^{miss} : uncertainties on the energy scale of jets or leptons are also propagated to the uncertainty of the E_T^{miss} . Other contributions to this uncertainty come from the uncertainty on the cell-out terms—soft energy calorimeter depositions not included in the reconstruction of leptons or jets—and from the pile-up modeling. The impact on the precision of the mass measurement is limited: the uncertainty due to this contribution is 0.02 GeV.

6.6.3 Signal modeling

The signal modeling uncertainties come from: the choice of matrix element and parton shower and hadronization model in the simulation of $t\bar{t}$ production and top-quark decays at the LHC, the choice of the PDF, the initial- and final-state radiation modeling (ISR/FSR), the color reconnection modeling, and the underlying event modeling. Their impact on the extracted mass is estimated using alternative Monte Carlo samples that are thought to cover the uncertainty of the signal modeling. The alternative input spectra are corrected using the nominal response matrix and the difference with the result for the nominal Monte Carlo is used to estimate the uncertainty.

The Monte Carlo generator (Generator) and hadronization (HAD): The uncertainty associated with the choice of the matrix element (labeled “generator” uncertainty in the following) is evaluated by comparing two NLO Monte Carlo generators matched with the same parton shower and hadronization program: we compare POWHEG and MC@NLO [? ?] (v4.01) both matched with HERWIG [43] (v6.520) for the parton showering and hadronization and JIMMY [?] (v4.31). The ATLAS AUET2 tune [?] is used. The full difference between the extracted masses is taken as the generator uncertainty. This yields a 0.28 GeV uncertainty. The uncertainty associated to the hadronization is estimated by comparing the results obtained with POWHEG matched with PYTHIA and HERWIG. The full difference is quoted as the hadronization uncertainty. This yields a 0.33 GeV uncertainty. The comparison of the unfolded distributions (for the l +jets channel) is shown in Fig. 6.9.

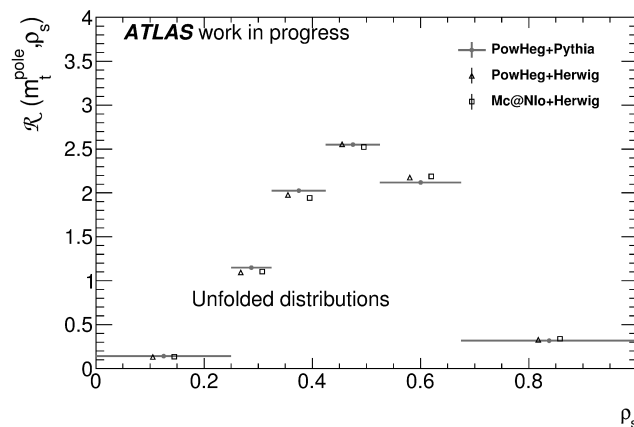


Figure 6.9: Three simulated \mathcal{R} distributions have been unfolded with the nominal unfolding matrix and factors evaluated with the nominal POWHEG+PYTHIA MC. The three simulations have been produced with the AtlasFast setup and correspond to the POWHEG+PYTHIA (nominal, red line), the MC@NLO+HERWIG (squares) and the POWHEG+HERWIG (triangles).

Initial and final-state radiation (ISR/FSR): The effect of the uncertainties in the ISR and FSR modeling is evaluated by comparing two signal samples with varied radiation settings. The samples to evaluate the ISR/FSR uncertainty are generated with ALPGEN+PYTHIA, which is a multileg Monte Carlo that generates, at LO, $t\bar{t}$ + 0, 1, 2, 3, 4, 5 partons. In this case, the official prescription used in direct determinations of the top-quark mass using the 7 TeV data from ATLAS is not followed. This prescription makes use of the ACERMC which generates $t\bar{t}$ events at LO that simulates the production of extra jets only using the parton shower evolution (i.e. PYTHIA). The ALPGEN+PYTHIA approach is considered instead since it is more conservative in the estimation of the uncertainty and it tends to explain better the \mathcal{R} -distribution spectra. The samples to estimate the ISR/FSR uncertainty correspond to variations of the *KTFAC* parameter in ALPGEN by a factor two and one half. This parameter determines the scale at which α_s is evaluated for additional gluon emissions (*KTFAC* therefore governs the relative rate of additional gluon emissions, but keeps the renormalization and factorization scales of the $pp \rightarrow t\bar{t}$ matrix element calculation approximately fixed). Each sample uses the corresponding Perugia 2011 tune [113] (i.e. the *radHi* sample, with *KTFAC*=1/2, uses *PYTUNE 351* - less pronounced activity of the parton shower - and the *radLo* sample, with *KTFAC*=2, uses *PYTUNE 352* - more pronounced activity of the parton shower -). These settings were tuned to fit the jet veto data [?]. These setting have been chosen to tune the jet veto data [?]. The ISR/FSR uncertainty is evaluated by taking half the difference between the results of both samples. This procedure yields a 0.72 GeV uncertainty. The ISR/FSR uncertainty in the \mathcal{R} distribution is shown in Figure 6.10. More details can be found in Appendix E where the two approaches are compared.

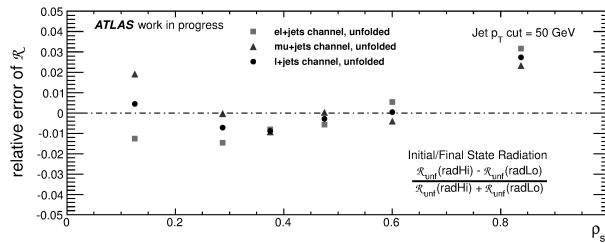


Figure 6.10: Impact on the \mathcal{R} distribution of the initial and final state radiation (ISR/FSR) evaluated with ACERMC+PYTHIA (uppermost plot) and ALPGEN+PYTHIA (lowermost plot). The results for the three channels are included for completeness.

Color reconnection (CR) and underlying event (UE): The impact of the uncertainties in the Monte Carlo models describing color reconnection and underlying event is estimated by comparing several POWHEG Monte Carlo samples with different tunes of the Perugia 2012 (P2012) family [113]. The effect of the color reconnection (CR) modeling uncertainty is estimated as the difference between the result obtained with the nominal POWHEG sample with the nominal P2012 tune and an alternative sample with the P2012 noCR tune which disconnects the color reconnection effects. To esti-

mate the uncertainty in Underlying Event (UE) modeling, the P2012 mpiHi tune, which simulate events with high underlying event activity, is compared with the P2012 tune. In both cases the full difference is taken as the systematic uncertainty. The estimated uncertainties associated to the CR and the UE in the \mathcal{R} distribution are presented in Fig. 6.11.

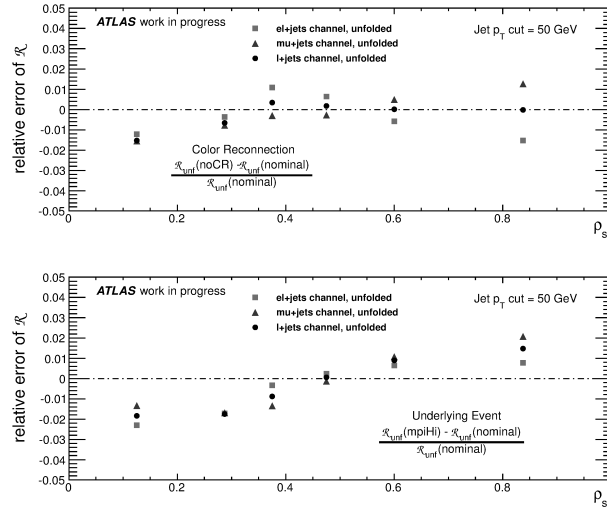


Figure 6.11: Impact on the \mathcal{R} distribution of the color reconnection (uppermost panel) and the underlying event uncertainties (lowermost panel). The results for the three channels are included for completeness.

The PDF choice: Uncertainties in the proton PDFs give rise to uncertainties in the preselection efficiency, via changes in the shapes of the lepton p_T and η distributions. These uncertainties are evaluated following the standard top group prescription based on the PDF4LHC recommendations [56].

For each PDF set considered, including the “error sets” that are provided along with the nominal PDF set, we reweight the baseline MC@NLO+HERWIG $t\bar{t}$ sample according to the x and Q^2 of each colliding parton to model the effect of assuming different PDFs. The resulting spectrum is unfolded to the perturbative level using the nominal POWHEG+PYTHIA response matrices and efficiency corrections. Finally, the fit is repeated to propagate the error to the top-quark pole mass.

The systematic uncertainty is evaluated as half of the maximum difference between the envelopes built with the results obtained for all the subsets included in the CT10 [58], the MSTW2008nlo68cl [41] and the NNPDF2.3 [60]. This yields an uncertainty of 0.54 GeV as it can be seen in Fig. 6.12.

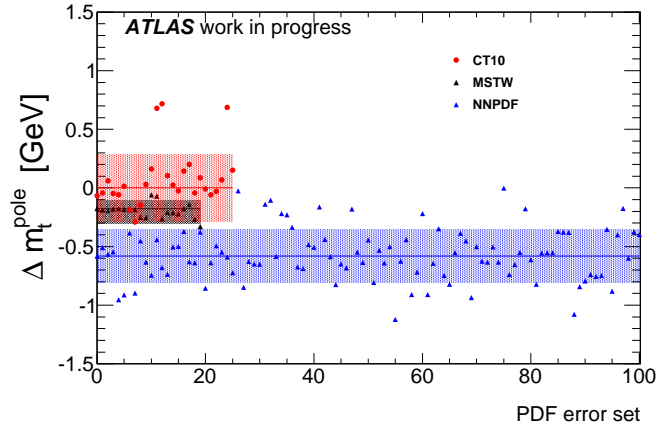


Figure 6.12: Uncertainties associated to the PDF choice for the l +jets channel. Three different PDF sets have been used to measure the $\sigma(m_t^{\text{pole}})$. The 56 different values of CT10 have been plotted as red circles, and the shadow region correspond to the symmetric Hessian. The 40 error set values of the MSTW2008nlo68cl are represented as black triangles and the uncertainty (shadow area) is evaluated as the asymmetric Hessian. The 100 different NNPDF2.3 results are represented as blue squares and the total uncertainty corresponds to the RMS. The three lines correspond to the best fit (CT10 and MSTW2008) of all the results and to the mean of the 100 values obtained by the NNPDF set.

6.6.4 Background modeling

The uncertainty in the background yield is taken into account by varying the normalization of the contribution of several processes. For both W and Z + jets, only the uncertainty on the normalization has been studied, according to Ref. [?]. For other sources shape uncertainties are also taken into account.

The theory uncertainty for inclusive $W(Z)$ +jets is 4%. The additional uncertainty per additional jet is 24% to be added in quadrature. For the signal 5-jet bin this corresponds therefore to 54%.

The shape and normalization uncertainties on the multijet predictions of the $t\bar{t}$ +1-jet reconstruction are propagated to the top-quark mass by propagating the measured uncertainties in the fake and real rates.

The most important background topologies come from the single-top production plus jets. The impact on the top-quark mass has been estimated by comparing the nominal yield (obtained using the POWHEG generator matched with PYTHIA) with the equivalent result with a different set of generators (MC@NLOsimulation for the s - and Wt -channels and ACERMC for the generation of the t -channel events).

The effect of the (Monte Carlo) top-quark mass used in the single top background evaluation has been also estimated by using two different input masses: 172.5 and 175 GeV.

Each of these contributions is given in Table 6.4. Together they amount to a background-related uncertainty of 0.17 GeV on the top-quark pole mass. The fit to

the unfolded data without any background subtraction has been compared with the nominal one as an exercise to estimate possible non-accounted backgrounds uncertainties. This is shown in the last row of Table 6.4. This result indicates that with our final selection the backgrounds are largely reduced and their effects become almost negligible.

Table 6.4: Uncertainty on the top-quark mass due to the background evaluation uncertainties.

Component	Uncertainty [GeV]
W +jets (normalization)	0.05
Z +jets (normalization)	0.02
Multijet (norm and shape)	0.12
Single top (norm and shape)	0.04
Single top (MC mass)	-0.08
Total	0.16
No background	0.13

6.7 Results and discussions

The normalized differential \mathcal{R} -distribution corresponding to the $t\bar{t} + 1$ -jet cross section with respect to the inverse of the invariant mass of the $t\bar{t} + 1$ -jet system $\sqrt{s_{t\bar{t}j}}$, after the background subtraction and the correction for detector and hadronization effects, is presented in Fig. 6.13. The prediction for the $t\bar{t} + 1$ -jet rate at NLO+PS is shown in the same figure for two different values of the top-quark pole mass: $m_t^{\text{pole}} = 170$ GeV and $m_t^{\text{pole}} = 180$ GeV. A zoom in the most sensitive on the top-quark mass ρ_s -interval is shown in Fig. 6.14.

The top-quark pole mass is extracted from a fit to the corrected \mathcal{R} distribution with the $t\bar{t} + 1$ -jet @NLO+PS calculation. The theoretical, statistical and systematic uncertainties, estimated as described in Section 6.6, are summarized in Tab. 6.5. The break-down in individual components of the systematic uncertainties associated to the jet energy scale, the uncertainty on the modeling of the ATLAS b -tagging performance and the yield and shape of the contribution of background processes is presented in Tables from 6.5 to 6.4 in Section 6.6.

The result obtained for the top-quark pole mass is:

$$m_t^{\text{pole}} = 173.71 \pm 1.50 \text{ (stat.)} \pm 1.43 \text{ (syst.)}_{-0.49}^{+0.95} \text{ (theo.) GeV}$$

The theory uncertainty estimates the impact of missing higher orders in the perturbative NLO calculation, the PDF choice and the α_s uncertainty. The experimental

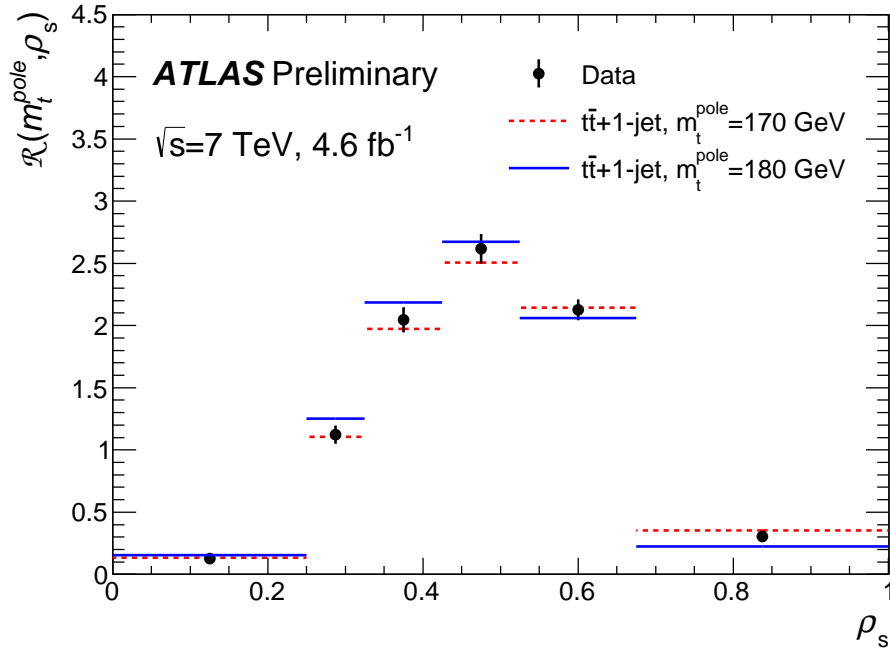


Figure 6.13: \mathcal{R} -distribution at parton level corrected for detector and hadronization effects after the background subtraction. The red-dotted (blue-continuous) lines correspond to the $t\bar{t}+1\text{-jet}$ @NLO+PS calculation using $m_t^{\text{pole}} = 170 \text{ GeV}$ (180 GeV). The black points correspond to the data.

error accounts for the uncertainties due to the modeling of the detector response and the background yield. Also considered in this error are the uncertainties arising from the signal modeling including hadronization. The statistical uncertainty takes into account the limited experimental data sample, as well as the (small) uncertainty due to the Monte Carlo statistics used in the unfolding procedure. The uncertainties are summarized in Tab. 6.5.

Additional cross checks

Dependence of the m_t^{pole} measurement on the p_T cut requirements.

The measurement of the top-quark mass reported here is performed using $t\bar{t}+1\text{-jet}$ events where the extra jet is required to have a transverse momentum greater than 50 GeV. Two alternative choices of this lower p_T cut have been studied: $p_T \geq 30, 40 \text{ GeV}$. The following results are obtained for the top quark mass, including the

Description	Value [GeV]
m_t^{pole}	173.71
Statistical uncertainty	1.50
Monte Carlo statistics	0.13
Signal MC Generator	0.28
Hadronization	0.33
Proton PDF	0.54
ISR/FSR	0.72
Color reconnection	0.14
Underlying Event	0.25
b -tagging efficiency and mistag rate	0.17
Jet reconstruction efficiency	0.05
Jet energy resolution	0.02
Jet energy scale (including b -jet energy scale)	0.94
Missing Transverse Momentum	0.02
Lepton uncertainties	0.07
Background	0.16
Total experimental syst. uncertainty	1.43
Scale uncertainty	(+0.93, -0.44)
Theory PDF uncertainty	0.21
Total theory syst. uncertainty	(+0.95, -0.49)
Total uncertainty	(+2.27, -2.12)

Table 6.5: Value of the inferred top-quark pole mass and of its uncertainties.

statistical error and propagating the dominant systematic uncertainty:

$$\begin{aligned}
m_t^{\text{pole}}(p_T \geq 30 \text{ GeV}) &= 173.72 \pm 1.21 \text{ (stat.)} \pm 1.35 \text{ (JES) GeV} \\
m_t^{\text{pole}}(p_T \geq 40 \text{ GeV}) &= 173.68 \pm 1.38 \text{ (stat.)} \pm 1.09 \text{ (JES) GeV} \\
m_t^{\text{pole}}(p_T \geq 50 \text{ GeV}) &= 173.55 \pm 1.50 \text{ (stat.)} \pm 0.94 \text{ (JES) GeV}
\end{aligned} \tag{6.6}$$

The three measurements yield compatible results (note that the three samples show significant overlap; the statistical error is not corrected for the correlation between the measurements). The statistical uncertainty on the measurement is reduced from 1.5 GeV to 1.4 GeV for a p_T cut at 40 GeV and to 1.2 GeV for a p_T cut of 30 GeV.

The impact on the top quark mass measurement of the dominant systematic uncertainty, due to the jet energy scale uncertainty, is also indicated and it increases as the p_T cut is lowered (the fractional JES uncertainty increases strongly for low- p_T jets). This, added to the fact that a higher p_T cut requirements reduces the higher-order corrections to the \mathcal{R} calculation (see Fig. 3.16 in Section 3.4.2), indicates that the use of large p_T cut requirements offers better prospects.

Top-quark mass determination for the independent channels (e +jets and μ +jets).

The result for the m_t^{pole} inferred from the independent distributions associated to the two different leptonic channels is in good agreement with the extracted m_t^{pole} for the l +jets channel. The unfolding of the \mathcal{R} -distribution obtained for each channels has been performed with the same unfolding matrix to enhance the statistical accuracy and reduce the fluctuations in the estimation of the systematic uncertainties. More information can be found in Appendix E. The results are:

$$\begin{aligned}
m_t^{\text{pole}}(\mu + jets) &= 171.95 \pm 1.96 \text{ (stat.)} \pm 1.41 \text{ (syst.)}_{-0.49}^{+0.95} \text{ (theo.) GeV} \\
m_t^{\text{pole}}(e + jets) &= 175.73 \pm 2.35 \text{ (stat.)} \pm 1.49 \text{ (syst.)}_{-0.49}^{+0.95} \text{ (theo.) GeV} \\
m_t^{\text{pole}}(l + jets) &= 173.71 \pm 1.50 \text{ (stat.)} \pm 1.43 \text{ (syst.)}_{-0.49}^{+0.95} \text{ (theo.) GeV}
\end{aligned} \tag{6.7}$$

Dependence of the m_t^{pole} measurement with the binning choice.

As a cross check the value for the top quark mass is extracted from the \mathcal{R} measurement in each of the bins. In Tab. 6.6, the results are shown for the six bins. The first bin, for the lowest p_s values, has been not considered for the combination of the measurements. In this bin, the sensitivity on the m_t^{pole} is residual. The same is true for the fourth and fifth bins, that correspond to the p_s value where the normalized curves for different values of the top quark mass cross. Indeed, the extracted top quark mass has a large statistical uncertainty in these bins. As expected, the second and especially the fourth bin, closest to the $t\bar{t}$ pair production threshold, have the greatest sensitivity. A naïve combination of the measurements (treating them as if they were independent) for each bin is also shown. The outcome is compared with the result

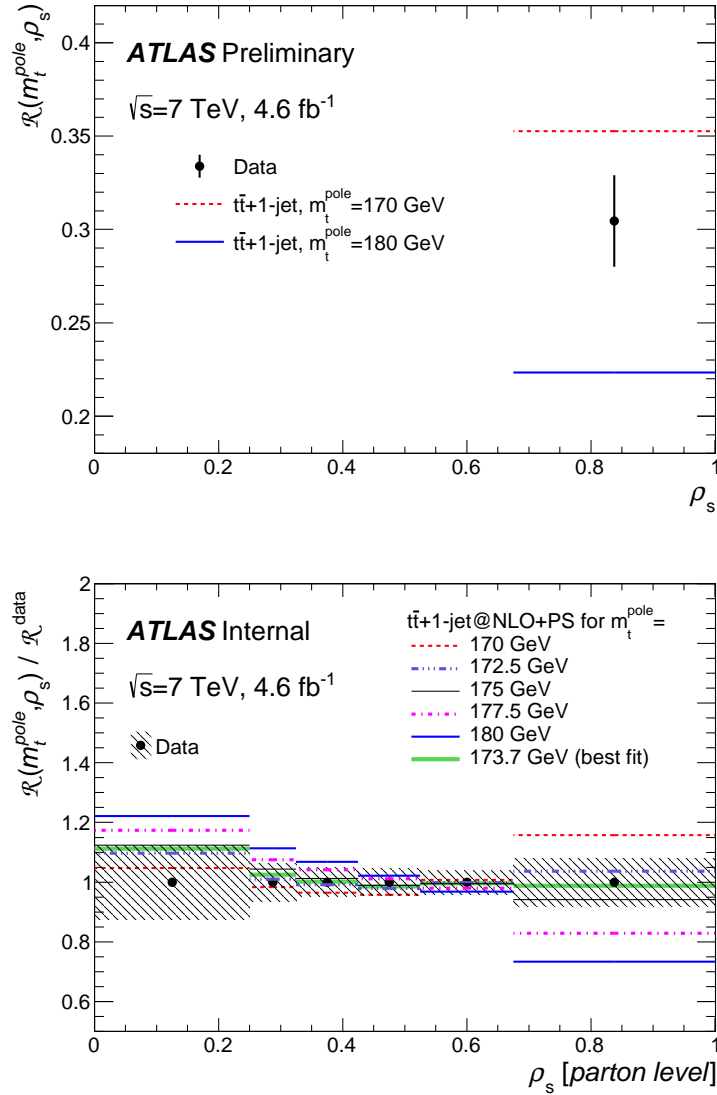


Figure 6.14: First figure: expanded view of the corrected \mathcal{R} distribution at the $0.675 < \rho_s < 1$ interval compared with $t\bar{t} + 1\text{-jet}$ @NLO+PS calculations for two different masses. Second figure: ratio between different \mathcal{R} distributions calculated and the measured at parton level \mathcal{R} distribution. In both figures the black points correspond to the data.

ρ_s	m_t^{pole} [GeV]
0 to 0.25	164 ± 7
0.25 to 0.325	172 ± 5
0.325 to 0.425	174 ± 6
0.425 to 0.525	178 ± 12
0.525 to 0.675	172 ± 26
0.675 to 1.0	173.5 ± 2.1
naive combination	173.3 ± 1.9
m_t^{pole} from χ^2 fit	173.7 ± 1.5

Table 6.6: m_t^{pole} extracted from a fit of the NLO+PS calculation to the \mathcal{R} measurements in the different bins. The next-to-last row presents the average of the measurements weighted by their statistical uncertainty. The last row contains the nominal results obtained with the χ^2 method, which estimates the statistical uncertainties taking in account the fact that the distribution is normalized (one degree of freedom less) and also it takes account for the migrations through the covariance matrix of the unfolded distribution. All uncertainties are statistical uncertainties only.

obtained using the χ^2 fit. The mass extracted from each of the bins is found to be compatible with the other bins and the nominal result within errors. All the results shown in Tab. 6.6 show the great coherence of the results.

A further cross check has been performed: the last bin has been reduced to $0.675 < \rho_s < 0.9$ (instead of $0.675 < \rho_s < 1$). Thus, the threshold region where reliable theoretical predictions are challenging is ignored. The result of the extracted mass from \mathcal{R} defined in the $[0, 0.9]$ interval of ρ_s is compatible with the nominal one with a difference bellow 0.1 GeV. The small difference of the extracted mass shows that the sensitivity to the region with $\rho_s > 0.9$ is limited.

Prospects for future analyses

Preliminary studies to reduce the size of the uncertainties in future measurements using this method have been performed. First, a large (~ 2.5) increase of the statistical precision is expected when the full 8 TeV is used. Second, a reduction of the systematic uncertainties is also expected since the sensitivity to the top-quark mass can be increased by reducing the bin size of the measured distribution while systematic uncertainties have a small dependence on the bin size. This will require improvements in the reconstruction of the $t\bar{t} + 1\text{-jet}$ system and detailed studies of the ρ_s resolution.

Another possible improvement may be achieved by measuring the \mathcal{R} distribution at particle level. This can reduce the dependence on the different fragmentation models.

Prospects for the reduction of uncertainties.

The dominant uncertainty in this measurement is the statistical uncertainty which amounts to $\sigma(m_t^{\text{pole}})(\text{stat.}) = 1.5$ GeV. Repeating this measurement using the data sample collected by the ATLAS experiment in 2012 will reduce the statistical uncertainty to be $\sigma(m_t^{\text{pole}})(\text{stat.}) \simeq 0.6$ GeV since the luminosity increases from 4.6 fb^{-1} to 20 fb^{-1} and the energy of the pp collisions increases from 7 TeV to 8 TeV producing an increase of the $t\bar{t} + 1\text{-jet}$ cross section of $\sim 40\%$.

Moreover, with the larger data set a finer binning would be possible, thus increasing the effective sensitivity to the top-quark mass as is shown in Figure 3.14 in Chapter 3. The bin size used in this analysis reduces the maximum sensitivity to $\mathcal{S} \sim 0.045$. The studies on the reduction of the bin size yields that an increase of the maximum sensitivity by a factor of ~ 1.7 is possible without introducing any increase of the systematic uncertainties. This has been studied for the largest source of experimental systematic uncertainty: the jet energy scale. Therefore, a reduction about 30 – 40% in the estimated uncertainties is considered within reach. Of course, reducing the bin size will be constrained by the resolution of the bin size of the ρ_s variable, which will need more dedicated studies in the future.

With these improvements and assuming a similar behavior of all the systematic uncertainties, a total estimated experimental uncertainty of

$$\sigma(m_t^{\text{pole}}) \sim 1 \text{ GeV}$$

in the determination of the m_t^{pole} might be achievable as compared to the present one.

Besides the improvements in the experimental measurement of the \mathcal{R} distribution, the theoretical calculations may also be improved by including higher order terms in the perturbative expansion. A further improvement could be obtained by using different mass schemes in the calculation as, for instance, the $\overline{\text{MS}}$ scheme. This happens for some specific calculations, as for example in the inclusive top-quark pair cross section [119] where the use of the $\overline{\text{MS}}$ scheme instead of the pole mass scheme introduces an improvement of the perturbative behavior of the QCD calculations leading to a reduction of the uncertainties associated to uncalculated higher order terms. In case of the \mathcal{R} distribution, the effect of using the $\overline{\text{MS}}$ scheme for the calculation is still unknown.

Prospects for the measurement at particle level

The measurement of the \mathcal{R} distribution has been performed at parton level using an unfolding procedure fed with events at reconstructed level. Further studies in the definition of the observable at particle level (based on stable particles before they enter the detector simulation) should be done in order to reduce and better understand the signal modeling uncertainty. This can be done as in the differential $t\bar{t}$ cross section measurements as function of pseudo-top-quark observables [120]. The mentioned pseudo-top-quark observables are defined by stable truth-level particles within given acceptance criteria chosen to minimize the dependence on theoretical models.

Conclusions

Measurements of top-quark parameters (mass, charge, couplings...) are crucial to test the Standard Model and possible extensions. This has been largely discussed along this report, with special focus in top-quark mass measurements. The top quark is the heaviest elementary particle discovered so far. Due to its large mass, it has the largest coupling to the Higgs boson. Therefore, it introduces large corrections into perturbative calculations through loop corrections. For example in the next-to-leading order calculations of the W boson and Higgs boson propagators.

Current top-quark mass measurements reach experimental precisions bellow 1 GeV. Most of these measurements are based on the direct determination of the top-quark mass from the kinematical properties of its decay products or on the top-quark mass extraction from the measurement of the inclusive $t\bar{t}$ cross section. In the first kind of methods, the measured mass is calibrated to the mass definition used in the Monte Carlo generators. The interpretation of the measured mass as the top-quark pole mass has an unknown uncertainty which can be of the order of 1 GeV [5, 6]. The second method shows a limited sensitivity to the top-quark mass, although it measures the mass in a well defined scheme.

Due to these issues the study and application of alternative top-quark mass measurements are important. Some of the desired theoretical properties of these alternative methods are:

1. good sensitivity to the mass;
2. to have to infrared safe and use a well defined mass scheme;
3. the NLO corrections with respect to the LO calculation should be small;
4. to be experimentally accessible.

The first result presented in this thesis, in Chapter 3, consists in the development of a new method to measure the top-quark mass following the above prescriptions. The definition of this observable was motivated by previous analyses performed at LEP (a electron-positron collider). These analyses exploited the dependence of jet

rates production on the b -quark mass since gluon emission from quarks depends on the mass of the emitting quark (gluon emission is suppressed for heavier quarks) [77, 78, 79, 80].

First attempts to define similar observables adapted to the top-quark mass extraction and to the LHC conditions were done using LO Monte Carlo tools (i.e. PYTHIA). With these tools the first point of the checklist mentioned above was proved the sensitive of the jet rates observables on the top-quark mass. After the positive prospects generated with these studies, a close collaboration with theoreticians working on QCD and top-quark physics (Dr. Peter Uwer, Dr. Sven-Olaf Moch and Dr. Simone Alioli from Berlin), was started. The final definition of the observable, the \mathcal{R} distribution, was born within this collaboration. Then, the top-quark mass dependence of the \mathcal{R} distribution and its perturbative behavior was exhaustively studied using different NLO calculations and the points 2-4 of the list were demonstrated to be satisfied. The results were published in Ref. [11].

The method consists in the measurement of the \mathcal{R} distribution defined as the normalized differential $t\bar{t} + 1$ -jet cross section as a function of the inverse of the invariant mass of the system:

$$\mathcal{R}(m_t^{\text{pole}}, \rho_s) = \frac{1}{\sigma_{t\bar{t}+1\text{-jet}}} \frac{d\sigma_{t\bar{t}+1\text{-jet}}}{d\rho_s}(m_t^{\text{pole}}, \rho_s), \quad (8.1)$$

where ρ_s is defined as

$$\rho_s = \frac{2m_0}{\sqrt{S_{t\bar{t}j}}}. \quad (8.2)$$

with m_0 an arbitrary constant, $m_0 = 170$ GeV. A lower cut on the p_T of 50 GeV is required to define the extra jet (defined with the anti- k_T algorithm with $R = 0.4$). The \mathcal{R} distribution calculated using $t\bar{t} + 1$ -jet @NLO for different masses is shown in Figure 3.13 in Chapter 3. For the mass value of $m_t^{\text{pole}} = 170$ GeV, the scale and PDF uncertainties have been included. The top-quark mass sensitivity is enhanced in the interval of large ρ_s values where the production of heavier top-quark masses is suppressed compared to lighter masses.

The top-quark mass extraction from the measurement of the \mathcal{R} distribution shares the rigorous interpretation of the mass with the top-quark mass measurement from the inclusive cross section measurements but gives much larger sensitivity by looking in specific phase space regions where the top-quark mass dependence is enhanced. Moreover, the \mathcal{R} distribution shows a good perturbative behavior with small uncertainties associated to the scale variations or the PDF choice.

Furthermore, when comparing the \mathcal{R} distribution predicted using different calculations ($t\bar{t} + 1$ -jet LO, NLO an NLO+PS, $t\bar{t}$ NLO+PS, where NLO+PS are referred to NLO calculations implemented in POWHEG and matched with a parton shower algorithm, i.e. PYTHIA) only small differences are obtained. Specifically, the extraction of the top-quark mass using a $t\bar{t} + 1$ -jet @NLO or a $t\bar{t} + 1$ -jet @NLO+PS calculation differs only in 0.3 GeV, which is well below the scale uncertainties. Using these tools, the experimental viability of the method was also proven, by estimating the size of the

systematic uncertainties expected to be dominant in an analysis involving real data. With these studies, it was therefore proven that the full list of desired properties of any new method are satisfied by the \mathcal{R} observable.

The main result of this thesis consists in the determination of the top-quark pole mass, m_t^{pole} , from the \mathcal{R} observable measured using real pp collisions at 7 TeV collected by the ATLAS detector at the LHC.

The reconstruction of $t\bar{t} + 1\text{-jet}$ has been performed for the semileptonic decay of the $t\bar{t}$ system: one of the W bosons produced during the decay of the top quarks decays into lepton and neutrino while the other W boson decays into two quarks. Thus, the $t\bar{t} + 1\text{-jet}$ signature in the detector consists of: two b -tagged jets, at least three non b -tagged jets, one high p_T lepton and a large amount of missing energy associated to the neutrino that traverses the detector undetected. The detection and identification of these objects exploits all capabilities of the ATLAS detector. The $t\bar{t} + 1\text{-jet}$ system and the p_s distribution is reconstructed using a kinematical algorithm that optimizes the identification of the W boson candidates and the top-quark candidates.

The top-quark mass determination using the \mathcal{R} distribution has been published in Ref. [12]. The \mathcal{R} distribution at parton level is obtained by subtracting the background events from the measured distribution, normalizing and by correcting the detector and fragmentation effects using an unfolding procedure. Different unfolding procedures have been studied. The chosen one is based in the regularized inversion of a response matrix constructed using Monte Carlo samples. It has been proven that the unfolded \mathcal{R} distribution values, and therefore the extracted m_t^{pole} , does not depend on the Monte Carlo mass used in the samples that define the unfolding procedure.

A complete study of the statistical and systematic uncertainties has been done. The systematic uncertainties have been divided in two categories: experimental and theoretical. The experimental uncertainties are divided in three types: signal-, detector- and background-modeling. The dominant uncertainties are the ones associated to the parton shower modeling (the modeling of the initial and final state radiation at the collinear and soft regime) with $\sigma(m_t^{\text{pole}}) = \pm 0.72$ GeV and to the calibration of the jet energy measurements (the jet energy scale uncertainties) with $\sigma(m_t^{\text{pole}}) = \pm 0.94$ GeV. The largest theoretical uncertainties are associated to the scale variations and to the PDF choice. The former estimates the uncertainty due to higher orders not included in the calculation and is the dominant theoretical uncertainty, with a value of $\sigma(m_t^{\text{pole}}) = {}^{+0.95}_{-0.49}$.

Finally, the top-quark mass has been extracted from the \mathcal{R} distribution. The obtained value for the top-quark pole mass is:

$$m_t^{\text{pole}} = 173.71 \pm 1.50 \text{ (stat.)} \pm 1.43 \text{ (syst.)} {}^{+0.95}_{-0.49} \text{ (theo.) GeV}$$

With a total uncertainty of $\sigma(m_t^{\text{pole}}) = {}^{+2.3}_{-2.1}$ this result represents the most precise top-quark pole mass measurement to date. The value obtained for the top-quark pole mass agrees with the most accurate previous top-quark mass measurement in the pole mass scheme [75] and with the direct top-quark mass measurement [7] well within the systematic and statistical uncertainties. Figure 8.1 shows a comparison with other top-quark pole mass measurements together with the world combination

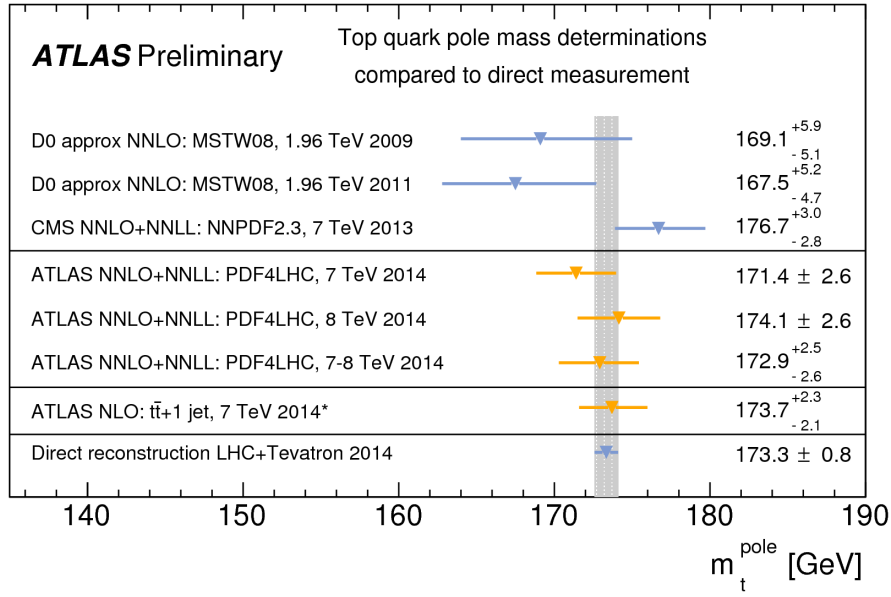


Figure 8.1: Comparative of top-quark pole mass determinations, including the result obtained in this thesis. They are compared with the world combination of direct top-quark mass measurements.

from the kinematic top-quark mass determination.

The dominant uncertainty is due to the limited data statistics considered in the analysis: $\sigma(m_t^{\text{pole}})(\text{stat.}) = 1.5 \text{ GeV}$. This uncertainty is expected to be largely reduced when studying the 20 fb^{-1} data collected in the 8 TeV run of the LHC. Moreover, with the larger data set, an improved top-quark mass sensitivity is possible through the reduction of the bin size of the distribution, which will require dedicated studies on the resolution of the p_s variable. Preliminary studies, described in Chapter 7, indicate that a reduction of $\sim 40\%$ of the systematical uncertainties could be envisaged.

Resumen en español

El llamado Modelo Estándar (ME) de física de partículas es el modelo teórico que describe las interacciones entre partículas a nivel subatómico. El ME asume que toda la materia está formada por partículas elementales, puntuales y sin estructura, y que están caracterizadas por sus números cuánticos.

Estas partículas elementales se clasifican en dos grupos de acuerdo al ME: fermiones y bosones, según estén descritos por la estadística de Fermi-Dirac (partículas de espín $1/2$) o por la de Bose-Einstein (partículas de espín entero) respectivamente.

Los bosones, a su vez, se clasifican en dos grupos: los asociados a las interacciones fundamentales y el bosón de Higgs. Los primeros son los intermediarios de las fuerzas descritas por el ME, que son: la fuerza fuerte, descrita por la Cromodinámica Cuántica, que es responsable de la formación de los núcleos atómicos; y la fuerza electrodébil, que es descrita por la teoría de las interacciones ElectroDébiles y que aglutina el electromagnetismo y la fuerza débil responsable de las desintegraciones radiactivas. El bosón de Higgs se cree que es la partícula recientemente descubierta en el Gran Colisionador de Hadrones (cuyas siglas en inglés son LHC) [1, 2]. Este bosón, de espín, carga y color nulos, está asociado al llamado campo de Brout-Englert-Higgs [19, 20, 21, 22, 23, 24] que permea el vacío y que es responsable de la generación de las masas de las partículas fundamentales. La generación de masas se produce tras la ruptura espontánea de la simetría subyacente en el Modelo Estándar mediante el mecanismo de Brout-Englert-Higgs.

Los fermiones, a su vez, se dividen en dos tipos diferentes: los que, además de las otras, sienten la fuerza fuerte y los que no. Los segundos son llamados leptones, que son los electrones que encontramos en la corteza atómica y su pareja cuántica el neutrino, que son partículas que solo sienten la fuerza débil y por lo tanto interactúan muy poco con la materia. El otro tipo de fermiones son los quarks. Los quarks no se encuentran en la naturaleza como partículas libres e individuales, sino que se encuentran aglutinados por la fuerza fuerte en partículas compuestas que son llamados hadrones (como son, por ejemplo, los protones).

Dado que los quarks no existen como partículas libres, su masa no puede ser medida de la misma forma que lo es, por ejemplo, la masa de los electrones. En el caso de las partículas libres, su masa física está asociada al módulo de su cuadrimomento. En el caso de los quarks, sus masas son acoplamientos efectivos de la teoría y solo pueden ser determinadas experimentalmente a través de su incidencia en observables hadrónicos igual que pasa, por ejemplo, con la constante de acoplamiento

de la fuerza fuerte, que es determinada a través de la medida de secciones eficaces, tasas de producción de partículas etc.,.

El quark top y su masa

Esta tesis está basada en el estudio del quark top y, específicamente, de su masa. ¿Por qué el quark top? ¿Por qué su masa? El quark top es la partícula más pesada del ME: su masa es alrededor de 35 veces la masa del segundo quark más pesado (el quark bottom). Ese valor tan grande de la masa, además, le confiere una característica que lo diferencia de los otros quarks: se desintegra antes de que el proceso de hadronización pueda tener lugar. Además, el quark top posee el mayor acoplamiento con el bosón de Higgs. Por esto mismo el quark top juega un papel especial en la teoría de las interacciones electrodébiles: debido al gran valor de su masa, el quark top introduce enormes correcciones en los cálculos teóricos. Es por eso que la medida de las propiedades del quark top y en concreto de su masa es fundamental.

Actualmente, las mejores medidas de la masa del quark top alcanzan precisiones de $\sim 0.5 \simeq 0.8$ GeV o incluso menores al combinar varias. Los métodos con menor incertidumbre experimental se basan en la medida de la masa del quark top a través de las propiedades cinemáticas de sus productos de desintegración (las llamadas medidas directas de la masa del quark top o medidas de la masa cinemática del quark top). El problema de este método es que tiene una incertidumbre aun desconocida (y que se ha estimado que podría ser del orden de 1 GeV [5, 6]) cuando se interpreta esta masa como la masa polo del quark top (la masa equivalente a la masa definida por el cuadrimomento de una partícula libre). Es, por lo tanto, crucial buscar nuevos y alternativos métodos para medir la masa.

Las características deseadas de cualquier método para medir la masa de un quark pueden ser resumidas en los siguientes puntos:

1. el método debe ser sensible a la masa;
2. el cálculo del observable utilizado en el método debe estar bien definido (correcciones a ordenes mayores que el primero dónde se defina sin ambigüedades la masa que se vaya a medir);
3. las correcciones de ordenes mayores en el cálculo deben ser pequeñas;
4. el observable ha de ser fácilmente medible.

Un ejemplo de método que cumple casi todas estas características es el de la extracción de la masa del quark top a través de su dependencia en la sección eficaz. Midiendo la sección eficaz se satisfacen todos los puntos de la lista anterior pero con el inconveniente de que la sensibilidad con la masa (el primer punto) es limitada.

Un nuevo método para medir la masa polo del quark top

El primer resultado presentado en esta tesis consiste en la definición y desarrollo de un nuevo método para medir la masa del quark top.

Este método está inspirado por métodos similares utilizados en el colisionador leptónico LEP para medir la masa del quark *bottom*. Específicamente, lo que se hacía era inferir la masa del quark a través de la medida de producción de eventos de tres jets: $e^+e^- \rightarrow Z \rightarrow b\bar{b}g$. En esta medida se aprovechaba la dependencia en la masa del quark que radia gluones ya que la emisión de gluones está suprimida para quarks más pesados.

Los primeros intentos para definir observables similares pero adaptados a las condiciones del LHC y a la medida del quark top se llevaron a cabo con métodos Monte Carlo que utilizan cálculos a primer orden (i.e. PYTHIA). Con estas herramientas se comprobó el primer punto de la lista para observables basados en la producción de jets asociados a un par de quark y antiquark top. A partir de estos prometedores estudios, se comenzó una estrecha colaboración con físicos teóricos expertos en el campo: los doctores Peter Uwer, Sven-Olaf Moch y Simone Alioli. Gracias a la estrecha colaboración entre físicos experimentales y teóricos se pudieron comprobar los restantes puntos de la lista y se definió el observable a utilizar: la distribución \mathcal{R} . Los resultados se publicaron en Ref. [11].

El método consiste en la medida de la distribución \mathcal{R} definida como la sección eficaz diferencial y normalizada de producción de eventos $t\bar{t} + 1$ -jet en función de la inversa de la masa invariante del sistema $t\bar{t} + 1$ -jet:

$$\mathcal{R}(m_t^{\text{pole}}, \rho_s) = \frac{1}{\sigma_{t\bar{t}+1\text{-jet}}} \frac{d\sigma_{t\bar{t}+1\text{-jet}}}{d\rho_s}(m_t^{\text{pole}}, \rho_s), \quad (8.3)$$

donde ρ_s es definida como

$$\rho_s = \frac{2m_0}{\sqrt{s_{t\bar{t}j}}}. \quad (8.4)$$

siendo m_0 un valor constant, $m_0 = 170$ GeV, para hacer adimensional la variable ρ_s . Un p_T mayor de 50 GeV se requiere para definir el jet extra (reconstruido utilizando el algoritmo anti- k_T con $R = 0.4$). La distribución \mathcal{R} calculada usando cálculos $t\bar{t} + 1$ -jet @NLO con diferentes masas se muestra en in Figura 8.2 (que aparece en el Capítulo 3). Para un valor $m_t^{\text{pole}} = 170$ GeV de la masa, las variaciones de escala también se muestran así como la predicción con dos PDFs diferentes. La dependencia con la masa del quark top se ve pronunciada en el intervalo de mayores ρ_s donde se observa que la emisión de jets por parte de quarks más pesados está suprimida con respecto a la de los quarks mas ligeros.

Este método satisface los requerimientos listados más arriba, en concreto, con este método la masa está bien definida a través de un cálculo a NLO. Además, este método muestra mayor sensibilidad a la masa del quark top que, por ejemplo, la extracción de la misma de la medida experimental de la sección eficaz inclusiva de eventos $t\bar{t}$. En la Figura 8.2, se muestra además que los errores asociados a la escala y a la elección de PDF son pequeños.

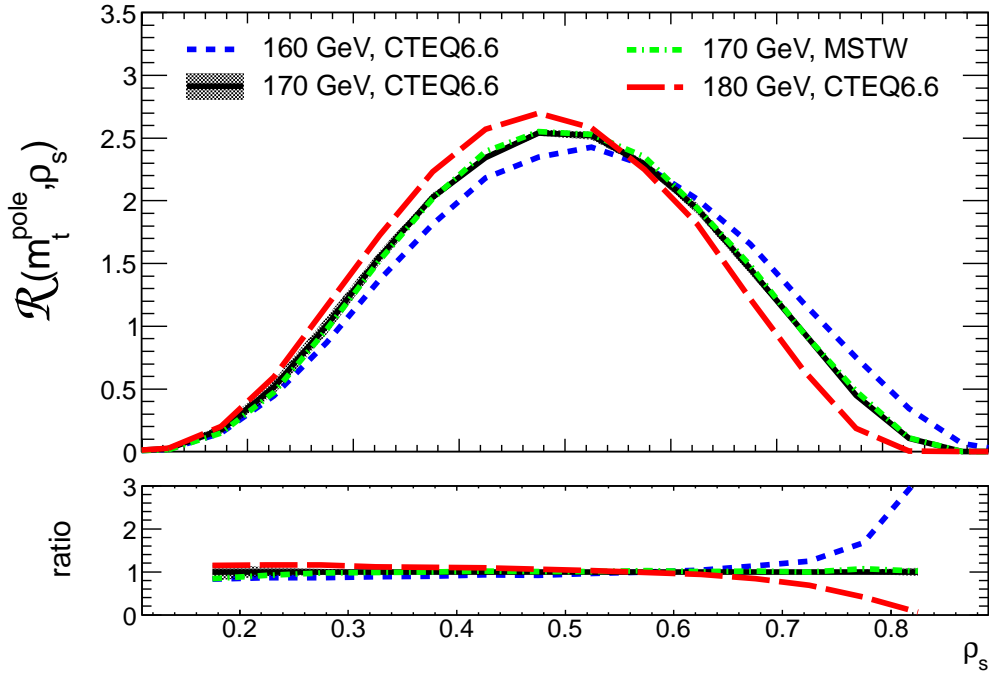


Figure 8.2: $\mathcal{R}(m_t^{\text{pole}}, \rho_s)$ calculada con precisión NLO para diferentes masas $m_t^{\text{pole}} = 160, 170$ and 180 GeV. Para $m_t^{\text{pole}} = 170$ GeV los errores debido a las variaciones de la escala y a la elección de la PDF se muestran. La proporción entre el resultado para $m_t^{\text{pole}} = 170$ GeV y las demás masas se muestra en la parte de abajo. La Figura se ha tomado de la Ref. [11].

En este estudio, además, se compararon diferentes predicciones para el cálculo de \mathcal{R} : $t\bar{t} + 1\text{-jet}$ LO, NLO y NLO+PS, $t\bar{t}$ NLO+PS, donde NLO+PS se refiere a cálculos NLO implementados con POWHEG y combinados con un algoritmo de *parton shower* i.e. PYTHIA. Comparando estas predicciones se demostró que el observable es muy robusto, incluso comparando cálculos de diferentes órdenes (LO vs NLO). En concreto, comparando cálculos $t\bar{t} + 1\text{-jet}$ @NLO con @NLO+PS se observan solo pequeñas diferencias, bien contenidas por las incertidumbres estimadas mediante las variaciones de escala.

Utilizando los cálculos implementados en POWHEG, la viabilidad experimental del método se estudió. Para ello, se estimó el efecto de los errores sistemáticos que se esperaban fueran dominantes (los asociados a la medida y calibración de la energía de los jets). Estos estudios se hicieron con herramientas públicas y no relacionadas con ningún detector en particular. Los estudios implementados en esta dirección resultaron en estimaciones muy cercanas a los valores finalmente medidos en la medida experimental final. Con todos estos estudios se probaron los 5 puntos de la lista de requerimientos.

El resultado principal presentado en esta tesis consiste en la determinación experimental de la masa polo del quark top a través de la medida de la distribución \mathcal{R} . Para ello se utilizaron los datos recogidos por ATLAS durante 2011 en colisiones pp

producidas en el LHC a 7 TeV.

La reconstrucción de los eventos $t\bar{t} + 1\text{-jet}$ se llevó a cabo seleccionando eventos en el canal semileptónico del sistema $t\bar{t}$: que uno de los bosones W producido en la desintegración del top, se desintegre a su vez en un leptón (solo consideramos los casos en los que el leptón es un muón o un electrón) y un neutrino y el otro bosón W en dos quarks. Por lo tanto, los eventos $t\bar{t} + 1\text{-jet}$, se seleccionan requiriendo: al menos 5 jets de los cuáles 2 jets de los jets son identificados como producidos por b -quarks, un leptón de alto p_T y una gran cantidad de energía transversa no detectada asociada a la presencia de un neutrino. La detección e identificación de estos objetos involucra todas las capacidades y subdetectores del experimento ATLAS. A partir de estos objetos reconstruidos, el sistema $t\bar{t} + 1\text{-jet}$ y la variable p_s se reconstruyen utilizando un algoritmo optimizado estudiando la cinemática de los eventos con datos simulados con Monte Carlo.

La determinación de la masa del quark top utilizando la distribución \mathcal{R} se ha publicado en Ref. [12]. La distribución al nivel partónico (dónde se compara con las predicciones teóricas) se obtiene tras, primero, substraer el background a la distribución reconstruida y, segundo, corregir esa distribución utilizando una matriz de respuesta que explica los cambios en p_s entre un evento a nivel partónico y el mismo a nivel reconstruido. El método de corrección elegido se basa en la inversión y regularización de la matriz de respuesta. Uno de los resultados más importantes de esta medida es la comprobación de que el método de corrección no depende de la masa utilizada en las muestras Monte Carlo.

Una vez reconstruida la distribución y corregida a nivel partónica, un estudio completo de las incertidumbres sistemáticas se ha llevado a cabo. Las incertidumbres sistemáticas estudiadas se dividen en dos grupos: las experimentales y las teóricas. Las teóricas son las asociadas a los ordenes no incluidos en la expansión perturbativa utilizada en el cálculo teórico y la asociada a la elección de la PDF del protón. Las incertidumbres sistemáticas experimentales se dividen, a su vez, en tres grupos: modelado de la señal, del detector y de la señal de fondo. Las dominantes son las incertidumbres del modelado de la radiación inicial y final y las incertidumbres debidas a la calibración de la energía de los *jets*.

Resultados y conclusiones

El valor obtenido para la masa polo del quark top y sus incertidumbres son:

$$m_t^{\text{pole}} = 173.71 \pm 1.50 \text{ (stat.)} \pm 1.43 \text{ (syst.)}^{+0.95}_{-0.49} \text{ (theo.) GeV}$$

Con una incertidumbre total de $\sigma(m_t^{\text{pole}}) = {}^{+2.3}_{-2.1}$, este resultado representa la mejor medida de la masa del quark top hasta el momento. Además, el valor medido está en buen acuerdo con los anteriormente obtenidos utilizando la sección eficaz $t\bar{t}$ [75] y con los valores de la masa cinemática [7] considerando las incertidumbres estimadas.

La Figura 8.3 muestra una comparativa de medidas hechas hasta el momento de la masa polo del quark top. La banda gris se corresponde con la combinación de las medidas de la masa cinemática del quark top.

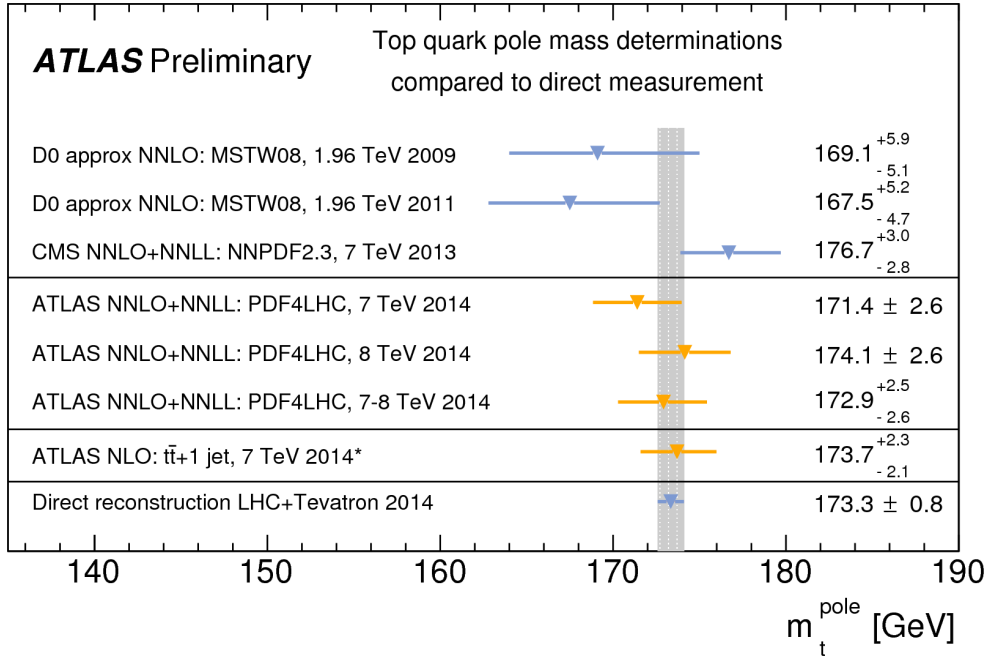


Figure 8.3: Comparativa de diferentes determinaciones de la masa polo del quark top y de la combinación de valores de las medidas de la masa cinemática.

La medida está dominada por la incertidumbre estadística $\sigma(m_t^{\text{pole}})(\text{stat.}) = 1.5$ GeV. Esta incertidumbre será reducida en gran medida cuando los datos recogidos por ATLAS en 2012 se estudien (20 fb^{-1} de colisiones pp a 8 TeV). Además, se ha mostrado en esta tesis que con mayor estadística, se puede reducir la sensibilidad con la masa del quark top al reducir el tamaño de los bins de la distribución ρ_s . Por supuesto esto requiere estudios detallados y concisos de la resolución en ρ_s , pero los estudios preliminares realizados hasta el momento, muestran que una reducción $\sim 40\%$ en las incertidumbres sistemáticas puede ser alcanzable.

Appendices

Appendix A

Unfolding correction based on the shape of the \mathcal{R} distribution.

A correction method based on the shape of the distributions was proposed in Ref. [11]. It consists in the calculation of the correction factors as a function of an intermediate variable, different from ρ_s , which depends on the integral of the \mathcal{R} distribution. This intermediate variable, w , is defined as the cumulative function of \mathcal{R} . For a given ρ'_s value:

$$w(\rho'_s) = \frac{\int_0^{\rho'_s} \mathcal{R}(\rho_s) d\rho_s}{\int_0^1 \mathcal{R}(\rho_s) d\rho_s}, \quad (\text{A.1})$$

then, the correction factors for \mathcal{R} and ρ_s , $f_{\mathcal{R}}$ and f_{ρ_s} , are calculated as

$$f_{\rho_s}(w(\rho_s)) \equiv \frac{w^{\text{partonic}}(\rho_s)}{w^{\text{reco}}(\rho_s)} \quad (\text{A.2})$$

$$f_{\mathcal{R}}(w(\rho_s)) \equiv \frac{\mathcal{R}^{\text{partonic}}(w(\rho_s))}{\mathcal{R}^{\text{reco}}(w(\rho_s))} \quad (\text{A.3})$$

where $f_{\mathcal{R}}$ and f_{ρ_s} are evaluated by comparing the theoretical calculation of \mathcal{R} at partonic level and the \mathcal{R} distribution simulated at reco level¹. The w^{reco} and w^{partonic} are evaluated as the cumulative function of the \mathcal{R} obtained at the reconstruction or the partonic level respectively.

Finally, correction procedure is defined as follows:

$$\mathcal{R}^{\text{partonic}}(\rho_s) \equiv f_{\mathcal{R}}(w(\rho_s)) \cdot \mathcal{R}^{\text{reco}}(f_{\rho_s}(w(\rho_s)) \cdot \rho_s(w^{\text{reco}})) \quad (\text{A.4})$$

¹Notice that in Ref. [11] the correction factors were evaluated by comparing the distributions at particle level (without any simulation of the detector) with the distribution at parton level. Similar behavior is expected when comparing distributions at reconstruction level with distributions at parton level.

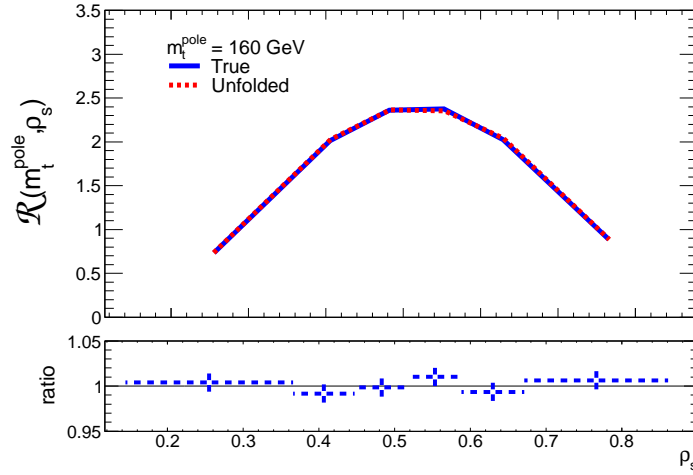


Figure A.1: Mass independence of the unfolding procedure based on the \mathcal{R} shape. Figure from Ref. [11].

The results are shown in Figure A.1. In the figure, a simulation of a reconstructed \mathcal{R} distribution that corresponds to a $m_t = 160$ GeV has been unfolded using the correction factors obtained with simulations performed with $m_t = 170$ GeV. The unfolded distribution is compared with a distribution at parton level calculated with $m_t = 160$ GeV: the differences between the unfolded distribution and the theoretical calculation are very small. The proposed unfolding method needs large large statistics in the samples in order to avoid fluctuations.

The result shows that a mass independent unfolding is possible. This has been checked for a interval of m_t between 160 and 180 GeV where the unfolding is independent with the mass within ~ 0.3 GeV due to the limited statistics of the sample.

Appendix B

Matrix inversion and regularization algorithm

B.1 The regularized covariance matrix

The statistical uncertainty of the corrected result is evaluated by repeating the unfolding procedure on pseudo-experiments corresponding to variations of the \mathcal{R} data points within their statistical uncertainty. The (small) uncertainty due to the limited number of Monte Carlo events used to define the unfolding procedure is evaluated by varying the migration matrices within the statistical uncertainties. It amounts to 0.13 GeV and it is accounted for as a systematic uncertainty.

These uncertainties are described by the regularized covariance matrix of the unfolded \mathcal{R} distribution, V , used in Eq. (6.4) to extract the top-quark mass. Fig. B.1 shows the covariance matrix constructed by combining the propagation of the statistical uncertainty of the data and the Monte Carlo sample.

B.2 One-step unfolding versus two-step unfolding

The unfolding procedure and the definition of the parton and first emission levels to where the data are corrected are presented in Chapter 6. The nominal unfolding procedure corrects the data in two steps: the first uses a matrix unfolding to account for migrations due to detector and hadronization effects that corrects the detector level (reco) result to the POWHEG first emission level; the second consists in a relatively small correction that corrects the first emission level to the parton level as defined in the theoretical calculation. This procedure is adopted due to a technical issue, as the Monte Carlo truth information in the ATLAS POWHEG Monte Carlo samples lack information to correctly define the parton level observables as we need in this analysis.

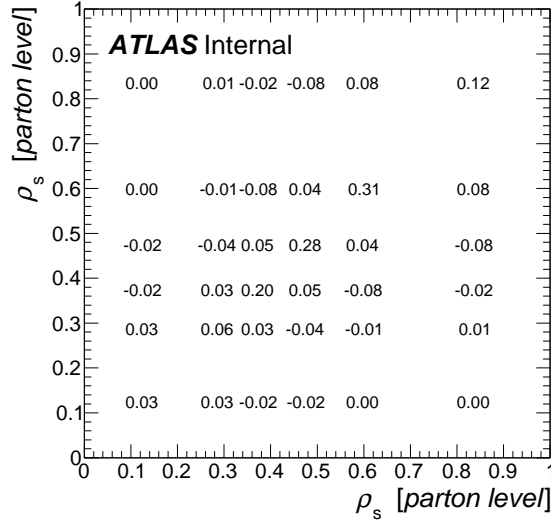


Figure B.1: Regularized covariance matrix of the unfolded $N_{t\bar{t}+1\text{-jet}}$ distribution for the $l + jets$ channel. The matrix is normalized to the number of entries.

Two Monte Carlo samples have been used to define the migration matrices that correct the real/simulated data to the parton and first emission level distributions. The nominal sample used is the POWHEG+PYTHIA sample:

```
mc11_7TeV.117050.TTbar_PowHeg_Pythia_P2011C.merge.NTUP_TOP.e1377
_s1372_s1370_r3108_r3109_p937/
```

A second sample based on POWHEG+HERWIG is used to cross-check the two-step unfolding procedure:

```
user.wbell.mc11_7TeV.105860.TTbar_PowHeg_Jimmy.merge.NTUP_TOP.e1198_a131
_s1353_a139_r2900_whb018/
```

Both Monte Carlo samples are based in $t\bar{t}$ events simulated at NLO accuracy with POWHEG and with the Parton Shower implemented with PYTHIA or HERWIG. The POWHEG+HERWIG samples allow to define the migration matrix that corrects the detector level result to the parton level in a single step.

The technical procedure used to choose the appropriate partons during the analy-

sis are found in the footnotes ¹ and ²

Therefore, a single-step unfolding procedure can be defined using the POWHEG samples matched with HERWIG:

$$\mathcal{R}^{partonic}(\rho_s, j) \equiv \frac{1}{\Delta(\rho_s, j)} \frac{\sum_i \mathcal{M}_{ji}^{-1, partonic} [D_i - B_i]}{N \mathcal{E}^{partonic}(\rho_s, j)} \quad (\text{B.1})$$

and it can be compared with the two-step procedure using the same sample.

The correction matrices for the lepton+jets channel based on POWHEG+herwig Monte Carlo are shown in Figures B.2, B.3 and B.4. The first matrix (in the uppermost plot) corresponds to the $\mathcal{M}^{partonic}$, that corrects from detector level to parton level in one step. The second matrix, Fig. B.3, corrects from detector level to POWHEG first emission level. This matrix is defined in the same way as the nominal unfolding matrix shown in Fig. 6.1. Finally, the migration matrix shown in Fig. B.4 describes the migrations from the parton level to the first emission level. In this case, it is seen that the bins in the diagonal of the matrix contain a larger fraction of the events than in the other cases. Most importantly, partonic events from the bin $0.525 < \rho_s < 0.675$ do not migrate to the $\rho_s > 0.675$ bin at the first emission level. This matrix is not used to perform the second correction factor as this matrix can not be built using the nominal POWHEG+PYTHIA MC samples, but it can be used to explain the small correction of the second factor applied in the two step unfolding procedure.

The efficiencies are also shown, as well as the second correction factor, in Figures B.5 and B.6. Notice that the information of the first emission level is the same for both POWHEG+PYTHIA and POWHEG+HERWIG since the same simulated events by POWHEG are used, but the distributions at the partonic level and at the reconstructed level changes since HERWIG and PYTHIA use different parton shower algorithms (that also affect to the definition of the partonic extra jet) and hadronisation algorithms. The correction factors shown in Fig. B.5 correspond to the two steps correction algorithm. The same correction factors evaluated using POWHEG+PYTHIA Monte Carlo samples

¹ POWHEG+PYTHIA: The top quarks that satisfy $mc_status \rightarrow at(i) == 3$ and $mc_pdgId \rightarrow at(i) == \pm 6$ are chosen as the partonic top-quarks. In this sample, they correspond to the fourth and fifth listed particles, but this can change for other particles, since it has been observed that in other samples the numbering of the particle can change (for example, starting in 1 not in zero, or if the information of the two protons colliding is not included). The first POWHEG emission is identified as the child of the two initial partons that generate the hard interaction (particles number 2 and 3 in the list which correspond to the $parton_1 + parton_2 \rightarrow t\bar{t} + parton_3$) which is not a top or anti-top quark and has $mc_status \rightarrow at(i) == 3$. The relevant information is found in the $mc_child_index \rightarrow at(i).at(j)$ pointer. To define the partonic jet it is needed the list of children of the first emission parton that are produced by the parton shower algorithm: $mc_child_index \rightarrow at(i_{First\ emission}).at(j) = null$. This is not provided in the POWHEG+PYTHIA samples. In our private samples, POWHEG $t\bar{t}$ events matched with PYTHIA have been generated, without including any other information (decays, hadronization, underlying event... etc).

² POWHEG+HERWIG: The partonic top quarks are defined in the same way as in the PYTHIA case. The first emission parton is, in this case, a child of the partons number 0 and 1, which correspond to the hard interaction partons. The status of this parton is $mc_status \rightarrow at(i) == 123$ or 124 . In this samples, the associated parton shower and evolution chain of this parton can be followed recursively using the $mc_child_index \rightarrow at(i_{First\ emission}).at(j)$ pointer. Studying this evolution chain, the final partons ($mc_status \rightarrow at(i) == 2$) before the hadronization process are found. From these partons, using the appropriate jet algorithm, the partonic jet can be reconstructed.

are found in Fig. 6.2. The correction factor shown in Fig. B.6 is the $\epsilon^{partonic}(\rho_s)$ defined in Eq. (B.1).

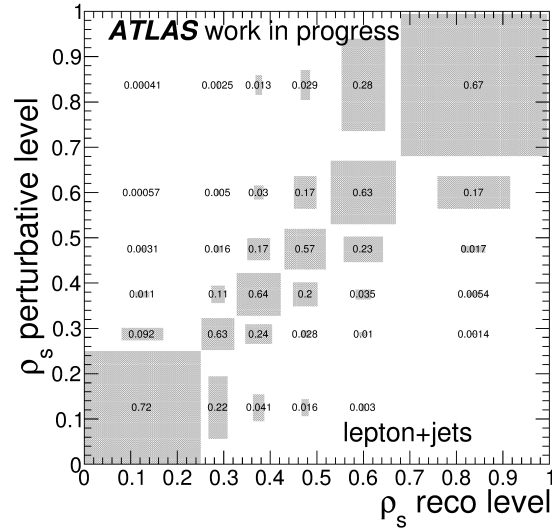


Figure B.2: Migration matrix evaluated with POWHEG+HERWIG MC samples: the single-step response matrix from detector level to parton level is shown.

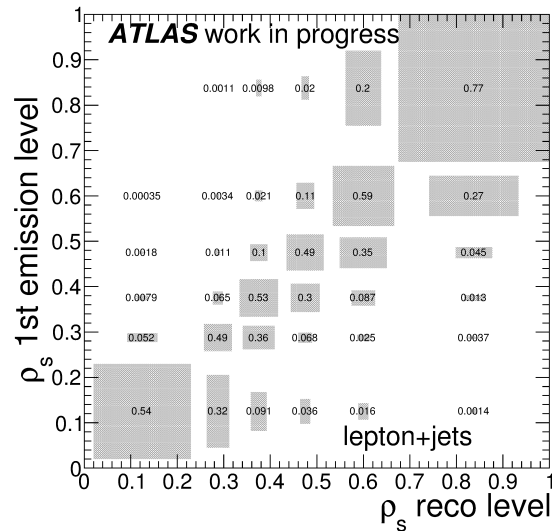


Figure B.3: The detector to POWHEG+HERWIG first emission level response matrix used in the two-step correction.

The central and lowermost plot show the efficiency ϵ and the second correction factor for the two-step unfolding. A fit to the results obtained with the two methods yield

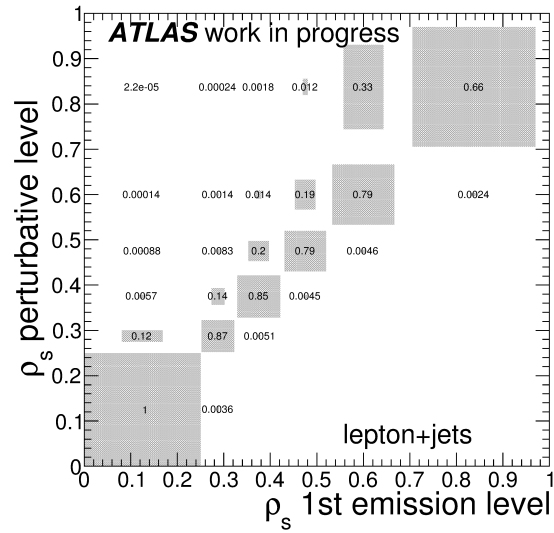


Figure B.4: Migration matrix evaluated with POWHEG+HERWIG MC samples for the POWHEG first emission level to parton level. It is observed that this matrix is very diagonal and has negligible migrations from low ρ_s values at partonic level to large ρ_s values at first emission level. This matrix is not used to perform the second correction factor but it qualitatively justifies the calculation of it as a bin-by-bin correction factor.

results that differ by 0.1 GeV, which is within the statistical uncertainty (~ 0.25 GeV) of the simulated data.

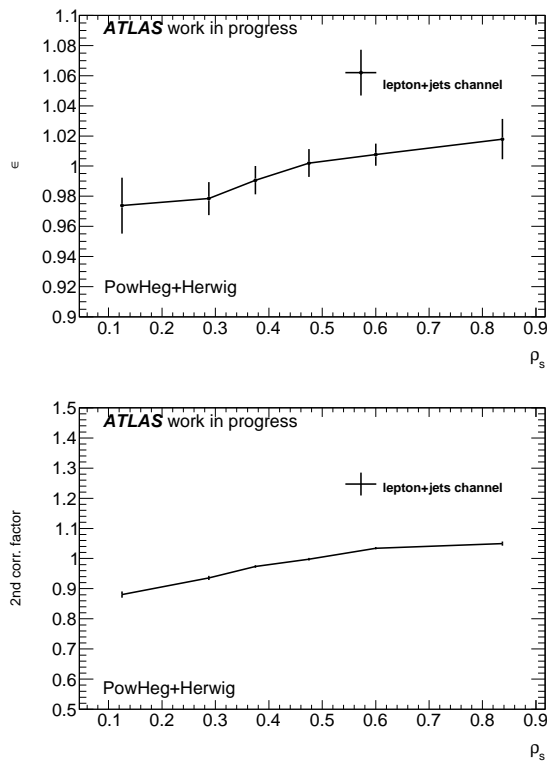


Figure B.5: The ϵ correction factor and the second correction factor for the two-step unfolding evaluated using POWHEG+HERWIG MC samples.

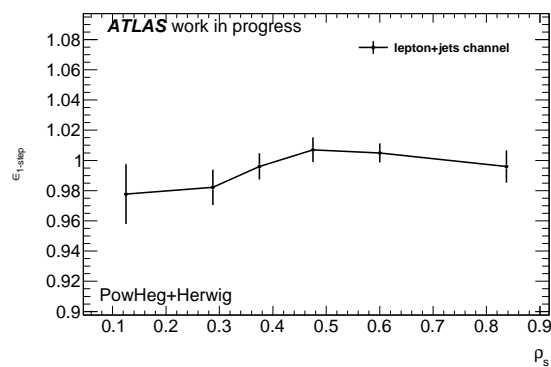


Figure B.6: The efficiency $\epsilon^{\text{partonic}}(\rho_s)$ for the one-step unfolding evaluated using POWHEG+HERWIG MC samples.

Appendix C

Parametrization of the $t\bar{t}$ +1-jet on

m_t^{pole} at NLO+PS accuracy

The mass dependence of the \mathcal{R} distribution is inferred from $t\bar{t}$ + 1-jet calculations at NLO+PS accuracy performed using 5 different top-quark masses (from 170 to 180 GeV in steps of 2.5 GeV). The results of these calculations are shown in Tab. 6.1 in Chapter 6. The mass dependence is parametrized for each of the intervals of p_s in which \mathcal{R} is defined. For that, three parametrization choices have been compared: first, second and third order polynomial .

To study the quality of the parametrization, three linearity tests on the fit procedure have been performed: several \mathcal{R} calculations ($t\bar{t}$ + 1-jet @NLO+PS) with different input value of the pole mass have been fitted using the three different parametrizations. The fit result is compared to the input mass in Figure C.1 (for parametrizations with first, second and third order polynomial). The RMS of the points (differences between m_t^{pole} and m_t^{fit}) are 0.16, 0.12 and 0.12 GeV for the 1st, 2nd and 3rd degree polynomial parametrization. The slope of linear fit to the points is found to be very small (~ 0.005) and the offsets are $(-0.06, -0.002$ and -0.03 GeV for the three different parametrizations. The uncertainty of this offset is, for all the parametrizations, ~ 0.06 GeV thus compatible with zero.

The impact of the choice of the functional form of the parametrization on the extracted mass is estimated by repeating the fits with each of them and tabulating the extracted mass, see Tab. C.1. A change of ~ 10 MeV from the fit of the data using a first or second order polynomial (in the l +jets channel) is observed. The third order polynomial yields nearly identical results to the second order polynomial.

The final choice for the mass dependence parametrization is the 2nd degree polynomial.

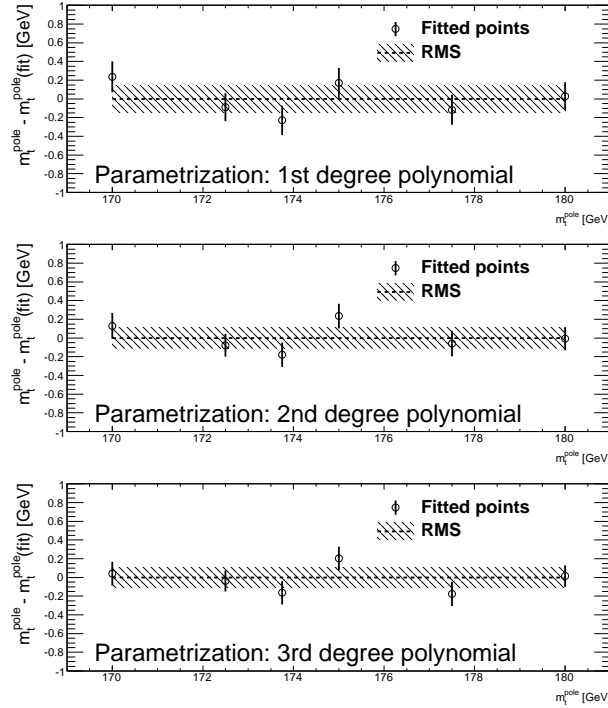


Figure C.1: Linearity test: different m_t^{pole} have been extracted from \mathcal{R} distributions evaluated using $t\bar{t} + 1\text{-jet}$ @NLO calculations. The deviation between the expected and the extracted mass is shown for the 1st, 2nd and 3rd order polynomial parametrizations (first, second and third figures respectively) of the m_t^{pole} dependence of the theoretical \mathcal{R} distributions

Table C.1: Extraction of the top-quark pole mass using different mass parametrizations for the \mathcal{R} distribution. The results for the lepton+jets channel are shown.

Mass extraction on data			
channel	Pol. 1st degree	Pol 2nd degree	Pol. 3rd degree
μ +jets	171.71	171.95	171.92
e l +jets	175.76	175.73	175.82
l +jets	173.72	173.71	173.71
Maximum (l +jets) difference: 10 MeV			
Averaged difference (all channels): 70 MeV			

Appendix D

Estimation of the Initial and final-state radiation (ISR/FSR) uncertainty.

The estimation of the uncertainty due to the mismodeling of the parton shower activity, the initial and final state radiation, has been presented in Chapter 6. In this appendix, two different approaches to estimate this uncertainty are compared: one estimates the uncertainties at the collinear and soft regime for $t\bar{t}$ topologies evaluated at LO, by varying within its uncertainty the α_s value in the evolution of the PS; the second estimates this uncertainty using $t\bar{t}$ calculations where the first emissions, up to the fifth, are evaluated at LO.

The default ATLAS procedure for direct top-quark mass measurements using the 7 TeV data is based on ACERMC+PYTHIA LO $t\bar{t}$ sample, where the extra jet is produced by the parton shower in PYTHIA. The ISR and FSR emission rate are varied by replacing the standard Perugia2011 tune with alternative tunes (essentially, these are variations of α_s in the evolution of the PS). The second approach, used in the differential cross-section measurement, is based on ALPGEN+PYTHIA $t\bar{t}+X$ samples. In this case, the upward and downward variations are evaluated by varying together the *ktfac* of ALPGEN which defines the threshold where ALPGEN (and not PYTHIA) takes care of the parton emission and also by varying at the same time the PYTHIA contribution to the PS (using again the P2011 tunes). In both cases the distributions are unfolded with the nominal POWHEG+PYTHIA Monte Carlo.

The ρ_s distributions for the UP and DOWN variations of the ISR/FSR in both generators are compared in Figure D.1 at the detector level. The same distribution of with the nominal Monte Carlo POWHEG+PYTHIA is shown for reference. All generators have $m_t = 172.5$ GeV. As might be expected, the ALPGEN+PYTHIA calculation provides a better description of the $t\bar{t} + 1$ -jet topologies than the ACERMC approach,

which has only PS accuracy for the extra jet.

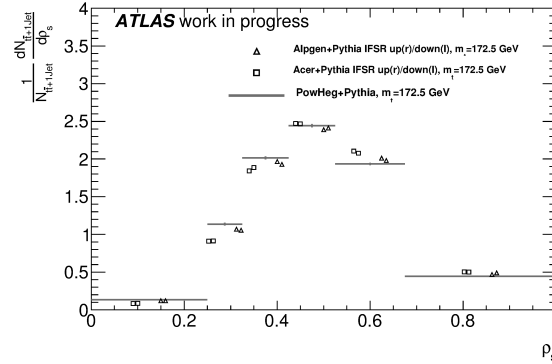


Figure D.1: The normalized ρ_s distribution of $t\bar{t} + 1$ -jet events, as predicted by ALPGEN+PYTHIA and ACERMC+PYTHIA. For both generators the UP and DOWN variations of the ISR/FSR rate are indicated. The nominal POWHEG+PYTHIA distribution is shown for reference.

The systematic uncertainty on the top-quark mass due to the uncertainty in the ISR/FSR modelling amounts to $\Delta m_t^{\text{pole}} = 0.27$ GeV ($l + jets$) if evaluated with the ACERMC samples. The ALPGEN+PYTHIA Monte Carlo samples, yield a larger uncertainty: $\Delta m_t^{\text{pole}} = 0.72$ GeV ($l + jets$). The results in Chapter 6 are based on the latter, more conservative, estimate that shows a better agreement with the data. The comparison of the ISR/FSR uncertainty on \mathcal{R} for both approaches is shown in Fig. D.2.

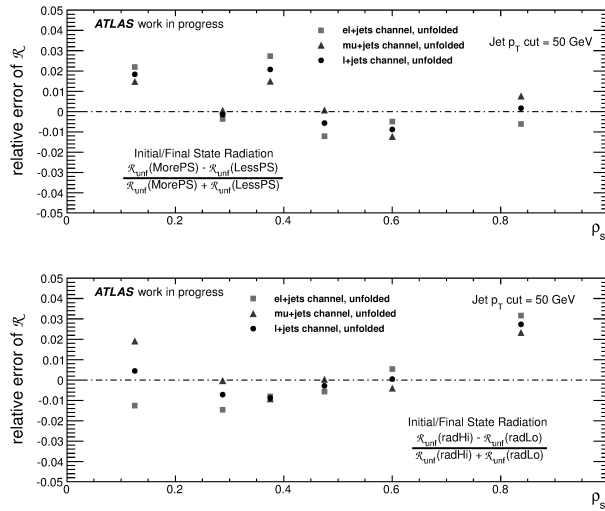


Figure D.2: Impact on the \mathcal{R} distribution of the initial and final state radiation (IFSR) evaluated with ACERMC+PYTHIA (upper plot) and ALPGEN+PYTHIA (lower plot).

Appendix E

Breakdown of the uncertainties evaluated for the different $t\bar{t}$ decay channels.

As a crosscheck, for a better understanding of the systematic uncertainties, their the evaluation is repeated for the three different channels. With this variation, the equivalent results to that shown in Table 6.5 are reproduced. This is shown in Table E.2.

Moreover, a similar exercise has been performed but using three different migration matrices during the unfolding: one for each channel (e , μ or l +jets). The statistical fluctuations during the evaluation of the systematic uncertainties become larger since the e and μ +jets matrices contain half of the statistics of the l +jets correction matrix. The results are shown in Table E.2.

Table E.1: The uncertainties in the top-quark pole mass measurement for the e +jets, μ +jets and the lepton ($l = e, \mu$)+jets channels.

	$\Delta m_t^{\text{pole}} [\text{GeV}]$		
	μ +jets	e +jets	l + jets
Signal modelling			
Generator	0.20	0.30	0.28
HAD	0.38	0.31	0.33
PDF	0.54	0.54	0.54
ISR/FSR	0.70	0.75	0.72
CR	0.12	0.11	0.14
UE	0.23	0.25	0.25
Detector, background modeling uncertainties			
BTAG	0.16	0.18	0.17
JEFF	0.06	0.05	0.05
JER	0.05	0.05	0.02
JES	0.94	1.03	0.94
MET (Cellout&Pileup)	0.04	0.01	0.02
Lepton Id&Energy	0.11	0.03	0.07
Background	0.15	0.18	0.16
Total systematic unc.	1.41	1.49	1.43
Statistical	1.96	2.35	1.50
Theory	+0.95 -0.49	+0.95 -0.49	+0.95 -0.49
Total (syst+stat+theory)	+2.60 -2.47	+2.94 -2.83	+2.27 -2.12

Table E.2: The uncertainties in the top-quark pole mass measurement for the e +jets, μ +jets and the lepton ($l = e, \mu$)+jets channels evaluated using three different migration matrices for the unfolding.

	$\Delta m_t^{\text{pole}} [\text{GeV}]$		
	μ +jets	e +jets	l + jets
Signal modelling			
Generator	0.58	0.21	0.28
HAD	0.32	0.20	0.33
PDF	0.54	0.54	0.54
IFSR	0.77	0.74	0.72
CR	0.08	0.09	0.14
UE	0.21	0.27	0.25
Detector and background modelling uncertainties			
BTAG	0.15	0.18	0.17
JEFF	0.04	0.05	0.05
JER	0.07	0.05	0.02
JES	0.98	0.94	0.94
MET (Cellout&Pileup)	0.03	0.00	0.02
Lepton Id&Energy	0.03	0.03	0.07
Background	0.14	0.19	0.16
Total systematic unc.	1.51	1.39	1.43
bf Statistical	1.96	2.35	1.50
Theory	+0.95 -0.49	+0.95 -0.49	+0.95 -0.49
Total (syst+stat+theory)	+2.65 -2.52	+2.89 -2.77	+2.23 -2.08

Appendix F

Validation of POWHEG samples

The reference ATLAS samples for this analysis correspond to the $t\bar{t}$ @ NLO process generated with the POWHEGMC generator matched to the PYTHIA parton shower. In the standard ATLAS data format the parton-level information to define the $t\bar{t} + 1$ -jet system at this level is incomplete. The correction is therefore performed in two stages. The first is a matrix unfolding to POWHEG first emission level, based on the standard ATLAS samples. The second stage is a relatively small bin-by-bin correction from POWHEG first emission to parton-level. The latter correction is determined using private POWHEG $t\bar{t}$ samples, where the complete information on the parton shower history is retained.

These private POWHEG samples were carefully validated. A sample of figures comparing the distributions of top and anti-top quark and the first gluon emission is included in this appendix. In all cases, the results from the official ATLAS samples are shown in black (continuous) and the private samples in red (dashed).

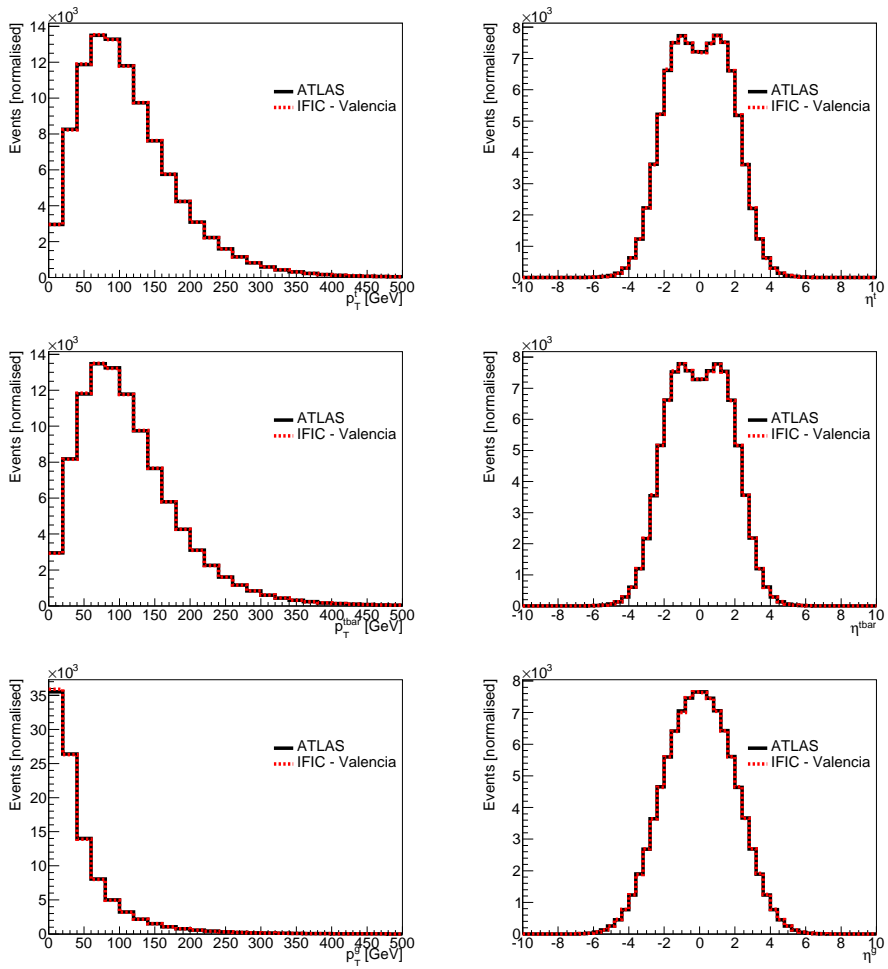


Figure F.1: Comparison of the p_T and pseudo-rapidity distributions of the top quark (upper row), anti-top quark (central row) and the first gluon emission (bottom row)

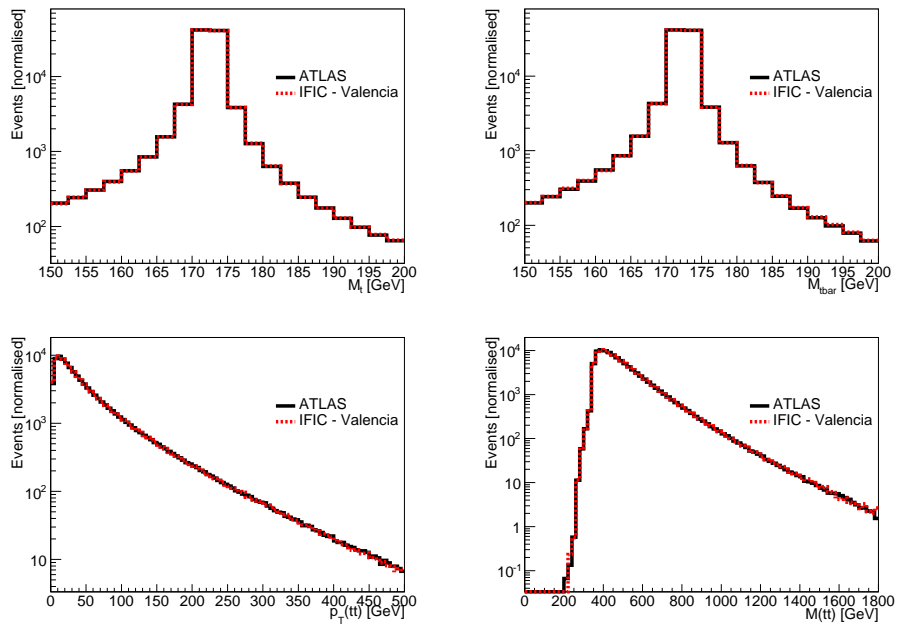


Figure F.2: Comparison of the top and anti-top quark mass distributions (upper row) and the p_T and invariant mass distribution of the $t\bar{t}$ system.

References

- [1] **ATLAS** Collaboration, *Observation of a new particle in the search for the Standard Model Higgs boson with the ATLAS detector at the LHC*, *Phys. Lett.* **B716** (2012) 1–29, [arXiv:1207.7214].
- [2] **CMS** Collaboration, *Observation of a new boson at a mass of 125 GeV with the CMS experiment at the LHC*, *Phys. Lett.* **B716** (2012) 30–61, [arXiv:1207.7235].
- [3] **D0** Collaboration, S. Abachi et al., *Search for High Mass Top Quark Production in $p\bar{p}$ Collisions at $\sqrt{s} = 1.8$ TeV*, *Phys. Rev. Lett.* **74** (Mar, 1995) 2422–2426, [hep-ex/9411001].
- [4] **CDF** Collaboration, F. Abe et al., *Observation of Top Quark Production in $p\bar{p}$ Collisions with the Collider Detector at Fermilab*, *Phys. Rev. Lett.* **74** (Apr, 1995) 2626–2631, [hep-ex/9503002].
- [5] A. H. Hoang and I. W. Stewart, *Top Mass Measurements from Jets and the Tevatron Top-Quark Mass*, *Nucl.Phys.Proc.Suppl.* **185** (2008) 220–226, [arXiv:0808.0222].
- [6] S. Moch et al., *High precision fundamental constants at the TeV scale*, arXiv:1405.4781.
- [7] **ATLAS, CDF, CMS and D0** Collaboration, *First combination of Tevatron and LHC measurements of the top quark mass*, ATLAS-CONF-2014-008 (March, 2014) [arXiv:1403.4427].
- [8] S. Dittmaier, P. Uwer, and S. Weinzierl, *NLO QCD corrections to t anti- t + jet production at hadron colliders*, *Phys. Rev. Lett.* **98** (2007) 262002, [hep-ph/0703120].
- [9] S. Dittmaier, P. Uwer, and S. Weinzierl, *Hadronic top-quark pair production in association with a hard jet at next-to-leading order QCD: Phenomenological studies for the Tevatron and the LHC*, *Eur. Phys. J* **C59** (2009) 625–646, [arXiv:0810.0452].
- [10] S. Alioli, S.-O. Moch, and P. Uwer, *Hadronic top-quark pair-production with one jet and parton showering*, *JHEP* **1201** (2012) 137, [arXiv:1110.5251].

- [11] S. Alioli et al., *A new observable to measure the top-quark mass at hadron colliders*, *Eur. Phys. J* **C73** (2013) 2438, [arXiv:1303.6415].
- [12] **ATLAS** Collaboration, *Determination of the top-quark pole mass using $t\bar{t}+1$ -jet events collected with the ATLAS experiment in 7 TeV pp collisions*, *ATLAS-CONF-2014-053* (Sep, 2014).
- [13] M. E. Peskin, *An Introduction to Quantum Field Theory*. Westview Press, 1995.
- [14] R. K. Ellis, *QCD and Collider Physics*. Cambridge University Press, 1996.
- [15] M. J. Costa, *Determination of the b quark mass at the Mz scale with the DELPHI detector at LEP*. PhD thesis, U. Valencia, València, 2003. Presented on 2003.
- [16] S. Glashow, *Partial Symmetries of Weak Interactions*, *Nucl.Phys.* **22** (1961) 579–588.
- [17] A. Salam, *Weak and Electromagnetic Interactions*, *Conf.Proc.* **C680519** (1968) 367–377.
- [18] S. Weinberg, *A Model of Leptons*, *Phys.Rev.Lett.* **19** (1967) 1264–1266.
- [19] F. Englert and R. Brout, *Broken Symmetry and the Mass of Gauge Vector Mesons*, *Phys. Rev. Lett.* **13** (1964) 321–323.
- [20] P. W. Higgs, *Broken symmetries, massless particles and gauge fields*, *Phys. Lett.* **12** (1964) 132–133.
- [21] P. W. Higgs, *Broken symmetries and the masses of gauge bosons*, *Phys. Rev. Lett.* **13** (Oct, 1964) 508–509.
- [22] G. S. Guralnik, C. R. Hagen, and T. W. B. Kibble, *Global conservation laws and massless particles*, *Phys. Rev. Lett.* **13** (Nov, 1964) 585–587.
- [23] P. W. Higgs, *Spontaneous symmetry breakdown without massless bosons*, *Phys. Rev.* **145** (May, 1966) 1156–1163.
- [24] T. W. B. Kibble, *Symmetry breaking in non-abelian gauge theories*, *Phys. Rev.* **155** (Mar, 1967) 1554–1561.
- [25] J. Beringer et al., *Review of Particle Physics*, *Journal of Physics G* **33** (2006) 1+.
- [26] **CMS** Collaboration, *Precise determination of the mass of the Higgs boson and studies of the compatibility of its couplings with the standard model*, *CMS-PAS-HIG-14-009* (2014).
- [27] **ATLAS** Collaboration, *Measurement of the Higgs boson mass from the $H \rightarrow \gamma\gamma$ and $H \rightarrow ZZ^* \rightarrow 4\ell$ channels with the ATLAS detector using 25 fb⁻¹ of pp collision data*, arXiv:1406.3827.

- [28] A. H. Mueller, ed., *Perturbative Quantum Chromodynamics*. World Scientific Publishing, 1989.
- [29] G. P. Salam, *Elements of QCD for hadron colliders*, arXiv:1011.5131.
- [30] A. Pich, *Lectures given at the ictp summer school in particle physics (trieste)*, 1999. hep-ph/0001118.
- [31] S. Alioli, *Shower monte carlo at nlo with the powheg box: the $t\bar{t}$ + jet hadroproduction case*, in <http://indico.ific.uv.es/indico/conferenceDisplay.py?confId=1810>, 2011.
- [32] J. C. Collins, D. E. Soper, and G. Sterman, *Factorization for short distance hadron-hadron scattering*, *Nuclear Physics B* **261** (1985), no. 0 104 – 142.
- [33] G. T. Hooft, *Renormalization of massless Yang-Mills fields*, *Nucl. Phys* **B33** (1971) 173–199, [arXiv:1011.5131].
- [34] T. D. Lee and M. Nauenberg, *Degenerate systems and mass singularities*, *Phys. Rev.* **133** (Mar, 1964) B1549–B1562.
- [35] T. Kinoshita, *Mass Singularities of Feynman Amplitudes*, *Journal of Mathematical Physics* **3** (1962), no. 4 650–677.
- [36] S. Catani and M. Seymour, *A general algorithm for calculating jet cross sections in nlo qcd*, *Nuclear Physics B* **485** (1997), no. 1–2 291–419.
- [37] Y. L. Dokshitzer, *Calculation of the Structure Functions for Deep Inelastic Scattering and e^+e^- Annihilation by Perturbation Theory in Quantum Chromodynamics.*, *Sov.Phys.JETP* **46** (1977) 641–653.
- [38] G. Altarelli and G. Parisi, *Asymptotic Freedom in Parton Language*, *Nucl.Phys.* **B126** (1977) 298.
- [39] V. N. Gribov and L. N. Lipatov, *Deep inelastic $e p$ scattering in perturbation theory*, *Sov. J. Nucl. Phys.* **15** (1972) 438–450.
- [40] **H1 and ZEUS** Collaboration, *Combined Measurement and QCD Analysis of the Inclusive e^+p Scattering Cross Sections at HERA*, *JHEP* **1001** (2010) 109, [arXiv:0911.0884].
- [41] A. Martin et al., *Parton distributions for the LHC*, *Eur. Phys. J* **C63** (2009) 189–285, [arXiv:0901.0002].
- [42] T. Sjostrand, S. Mrenna, and P. r. Z. Skands, *PYTHIA 6.4 Physics and Manual*, *JHEP* **0605** (2006) 026, [hep-ph/0603175].
- [43] G. Corcella et al., *HERWIG 6: An Event generator for hadron emission reactions with interfering gluons (including supersymmetric processes)*, *JHEP* **0101** (2001) 010, [hep-ph/0011363].

- [44] M. L. Mangano, M. Moretti, F. Piccinini, and M. Treccani, *Matching matrix elements and shower evolution for top-quark production in hadronic collisions*, *JHEP* **0701** (2007) 013, [hep-ph/0611129].
- [45] S. Hoeche et al., *Matching parton showers and matrix elements*, hep-ph/0602031.
- [46] M. L. Mangano, *presentation at the FNAL Matrix Element/Monte Carlo Tuning Working Group*, .
- [47] S. Frixione and B. R. Webber, *Matching NLO QCD computations and parton shower simulations*, *JHEP* **0206** (2002) 029, [hep-ph/0204244].
- [48] S. Alioli et al., *A general framework for implementing NLO calculations in shower Monte Carlo programs: the POWHEG BOX*, *JHEP* **1006** (2010) 043, [arXiv:1002.2581].
- [49] G. P. Salam, *Towards Jetography*, *Eur.Phys.J.* **C67** (2010) 637–686, [arXiv:0906.1833].
- [50] P. Baernreuther, M. Czakon, and A. Mitov, *Percent Level Precision Physics at the Tevatron: First Genuine NNLO QCD Corrections to $q\bar{q} \rightarrow t\bar{t} + X$* , *Phys. Rev. Lett.* **109** (2012) 132001, [arXiv:1204.5201].
- [51] M. Cacciari et al., *Top-pair production at hadron colliders with next-to-next-to-leading logarithmic soft-gluon resummation*, *Phys. Lett.* **B710** (2012) 612–622, [arXiv:1111.5869].
- [52] M. Czakon, P. Fiedler, and A. Mitov, *Total Top-Quark Pair-Production Cross Section at Hadron Colliders Through $O(\frac{4}{3})$* , *Phys. Rev. Lett.* **110** (2013), no. 25 252004, [arXiv:1303.6254].
- [53] M. Czakon and A. Mitov, *NNLO corrections to top pair production at hadron colliders: the quark-gluon reaction*, *JHEP* **1301** (2013) 080, [arXiv:1210.6832].
- [54] M. Czakon and A. Mitov, *NNLO corrections to top-pair production at hadron colliders: the all-fermionic scattering channels*, *JHEP* **1212** (2012) 054, [arXiv:1207.0236].
- [55] M. Czakon and A. Mitov, *Top++: A Program for the Calculation of the Top-Pair Cross-Section at Hadron Colliders*, *Comput.Phys.Commun.* **185** (2014) 2930, [arXiv:1112.5675].
- [56] M. Botje et al., *The PDF4LHC Working Group Interim Recommendations*, arXiv:1101.0538.
- [57] J. Gao, M. Guzzi, J. Huston, H.-L. Lai, Z. Li, et al., *CT10 next-to-next-to-leading order global analysis of QCD*, *Phys.Rev.* **D89** (2014), no. 3 033009, [arXiv:1302.6246].

- [58] H.-L. Lai et al., *New parton distributions for collider physics*, *Phys.Rev.* **D82** (2010) 074024, [arXiv:1007.2241].
- [59] A. Martin, W. Stirling, R. Thorne, and G. Watt, *Uncertainties on $\alpha(S)$ in global PDF analyses and implications for predicted hadronic cross sections*, *Eur. Phys. J* **C64** (2009) 653–680, [arXiv:0905.3531].
- [60] R. D. Ball, V. Bertone, S. Carrazza, C. S. Deans, L. Del Debbio, et al., *Parton distributions with LHC data*, *Nucl.Phys.* **B867** (2013) 244–289, [arXiv:1207.1303].
- [61] S. P. Martin, *A Supersymmetry primer*, *Adv.Ser.Direct.High Energy Phys.* **21** (2010) 1–153, [hep-ph/9709356].
- [62] S. Heinemeyer, W. Hollik, D. Stockinger, A. Weber, and G. Weiglein, *Precise prediction for $M(W)$ in the MSSM*, *JHEP* **0608** (2006) 052, [hep-ph/0604147].
- [63] S. Heinemeyer, W. Hollik, and G. Weiglein, *Electroweak precision observables in the minimal supersymmetric standard model*, *Phys.Rept.* **425** (2006) 265–368, [hep-ph/0412214].
- [64] A. Djouadi, P. Gambino, S. Heinemeyer, W. Hollik, C. Junger, et al., *Supersymmetric contributions to electroweak precision observables: QCD corrections*, *Phys.Rev.Lett.* **78** (1997) 3626–3629, [hep-ph/9612363].
- [65] A. Djouadi, P. Gambino, S. Heinemeyer, W. Hollik, C. Junger, et al., *Leading QCD corrections to scalar quark contributions to electroweak precision observables*, *Phys.Rev.* **D57** (1998) 4179–4196, [hep-ph/9710438].
- [66] A. Dedes and A. Pilaftsis, *Resummed effective Lagrangian for Higgs mediated FCNC interactions in the CP violating MSSM*, *Phys.Rev.* **D67** (2003) 015012, [hep-ph/0209306].
- [67] J. Haestier, S. Heinemeyer, D. Stockinger, and G. Weiglein, *Electroweak precision observables: Two-loop Yukawa corrections of supersymmetric particles*, *JHEP* **0512** (2005) 027, [hep-ph/0508139].
- [68] J. Elias-Miro, J. R. Espinosa, G. F. Giudice, G. Isidori, A. Riotto, et al., *Higgs mass implications on the stability of the electroweak vacuum*, *Phys. Lett.* **B709** (2012) 222–228, [arXiv:1112.3022].
- [69] G. Degrandi et al., *Higgs mass and vacuum stability in the Standard Model at NNLO*, *JHEP* **1208** (2012) 098, [arXiv:1205.6497].
- [70] S. Alekhin, A. Djouadi, and S. Moch, *The top quark and Higgs boson masses and the stability of the electroweak vacuum*, *Phys. Lett.* **B716** (2012) 214–219, [arXiv:1207.0980].
- [71] D. Buttazzo et al., *Investigating the near-criticality of the Higgs boson*, *JHEP* **1312** (2013) 089, [arXiv:1307.3536].

- [72] S. Alekhin, J. Bluemlein, and S. Moch, *The ABM parton distributions tuned to LHC data*, *Phys.Rev.* **D89** (2014) 054028, [arXiv:1310.3059].
- [73] **ATLAS** Collaboration, *Measurement of the Top Quark Mass from $\sqrt{s} = 7$ TeV ATLAS Data using a 3-dimensional Template Fit*, .
- [74] **CMS** Collaboration, *Measurement of the top-quark mass in $t\bar{t}$ events with lepton+jets final states in pp collisions at $\sqrt{s}=8$ TeV*, *CMS-PAS-TOP-14-001* (2014).
- [75] **ATLAS** Collaboration, *Measurement of the $t\bar{t}$ production cross-section using $e\mu$ events with b -tagged jets in pp collisions at $\sqrt{s} = 7$ and 8 TeV with the ATLAS detector*, arXiv:1406.5375.
- [76] M. C. Smith and S. S. Willenbrock, *Top quark pole mass*, *Phys.Rev.Lett.* **79** (1997) 3825–3828, [hep-ph/9612329].
- [77] G. Rodrigo, A. Santamaria, and M. S. Bilenky, *Do the quark masses run? Extracting $m\text{-bar}(b)$ ($m(z)$) from LEP data*, *Phys. Rev. Lett.* **79** (1997) 193–196, [hep-ph/9703358].
- [78] W. Bernreuther, A. Brandenburg, and P. Uwer, *Next-to-leading order QCD corrections to three jet cross-sections with massive quarks*, *Phys.Rev.Lett.* **79** (1997) 189–192, [hep-ph/9703305].
- [79] M. S. Bilenky, S. Caberera, J. Fuster, S. Marti, G. Rodrigo, et al., *$m(b)(m(Z))$ from jet production at the Z peak in the Cambridge algorithm*, *Phys.Rev.* **D60** (1999) 114006, [hep-ph/9807489].
- [80] **DELPHI** Collaboration, *$m(b)$ at $M(Z)$* , *Phys.Lett.* **B418** (1998) 430–442.
- [81] S. Dittmaier, P. Uwer, and S. Weinzierl, *Phenomenological studies of top-pair production + jet at NLO*, arXiv:0905.2299.
- [82] M. Cacciari, G. P. Salam, and G. Soyez, *The Anti- $k(t)$ jet clustering algorithm*, *JHEP* **0804** (2008) 063, [arXiv:0802.1189].
- [83] M. Cacciari, G. P. Salam, and G. Soyez, *FastJet user manual*, *Eur. Phys. J* **C72** (2012) 1896, [arXiv:1111.6097].
- [84] P. M. Nadolsky et al., *Implications of CTEQ global analysis for collider observables*, *Phys. Rev.* **D78** (2008) 013004, [0802.0007].
- [85] H.-L. Lai, J. Huston, S. Mrenna, P. Nadolsky, D. Stump, et al., *Parton Distributions for Event Generators*, *JHEP* **1004** (2010) 035, [arXiv:0910.4183].
- [86] A. Denner et al., *NLO QCD corrections to off-shell top-antitop production with leptonic decays at hadron colliders*, *JHEP* **1210** (2012) 110.

- [87] A. Denner et al., *NLO QCD corrections to off-shell $t\bar{t}$ production at hadron colliders*, *PoS* **2012** (LL2012) 015, [1208.4053].
- [88] S. Frixione, P. Nason, and G. Ridolfi, *A Positive-weight next-to-leading-order Monte Carlo for heavy flavour hadroproduction*, *JHEP* **0709** (2007) 126, [arXiv:0707.3088].
- [89] **ATLAS** Collaboration, *Improved luminosity determination in pp collisions at $\sqrt{s} = 7$ TeV using the ATLAS detector at the LHC*, *Eur. Phys. J* **C73** (2013) 2518, [arXiv:1302.4393].
- [90] CERN, *Cern press*, <http://press.web.cern.ch/>, 2014.
- [91] CERN, *Experiments at cern*, <http://home.web.cern.ch/about/experiments>, 2014.
- [92] **CMS** Collaboration, S. Chatrchyan et al., *The CMS experiment at the CERN LHC*, *JINST* **3** (2008) S08004.
- [93] **ATLAS** Collaboration, G. Aad et al., *The ATLAS Experiment at the CERN Large Hadron Collider*, *JINST* **3** (2008) S08003.
- [94] **ALICE** Collaboration, K. Aamodt et al., *The ALICE experiment at the CERN LHC*, *JINST* **3** (2008) S08002.
- [95] **LHCb** Collaboration, J. Alves, A. Augusto et al., *The LHCb Detector at the LHC*, *JINST* **3** (2008) S08005.
- [96] **LHCf** Collaboration, O. Adriani et al., *The LHCf detector at the CERN Large Hadron Collider*, *JINST* **3** (2008) S08006.
- [97] **TOTEM** Collaboration, G. Anelli et al., *The TOTEM experiment at the CERN Large Hadron Collider*, *JINST* **3** (2008) S08007.
- [98] **MoEDAL** Collaboration, J. Pinfold et al., *Technical Design Report of the MoEDAL Experiment*, .
- [99] **ATLAS** Collaboration, *Atlas multimedia*, <http://www.atlas.ch/photos/index.html>, 2014.
- [100] **ATLAS** Collaboration, *ATLAS inner detector: Technical design report. Vol. 1*, .
- [101] F. Balli, G. Compostella, G. Cortiana, R. Nisius, and J. Schwinding, *Measurement of the Top Quark Mass from $\sqrt{s} = 7$ TeV ATLAS Data using a 3-dimensional Template Fit*, *ATLAS-COM-CONF-2013-058* (Apr, 2013).
- [102] **ATLAS** Collaboration, *Measurement of the top quark mass with the template method in the top antitop \rightarrow lepton + jets channel using ATLAS data*, *Eur. Phys. J* **C 72** (Mar, 2012) 2046. 30 p.

- [103] **ATLAS** Collaboration, *Calorimeter Clustering Algorithms: Description and Performance*, ATL-LARG-PUB-2008-002. ATL-COM-LARG-2008-003 (Apr, 2008).
- [104] **ATLAS** Collaboration, *Jet energy measurement and its systematic uncertainty in proton-proton collisions at $\sqrt{s} = 7$ TeV with the ATLAS detector*, arXiv:1406.0076.
- [105] **ATLAS** Collaboration, *Measurement of the Mistag Rate with 5 fb¹ of Data Collected by the ATLAS Detector*, ATLAS-CONF-2012-040 (Mar, 2012).
- [106] **ATLAS** Collaboration, *Measurement of the b-tag Efficiency in a Sample of Jets Containing Muons with 5 fb¹ of Data from the ATLAS Detector*, ATLAS-CONF-2012-043 (Mar, 2012).
- [107] **ATLAS** Collaboration, *Measuring the b-tag efficiency in a top-pair sample with 4.7 fb⁻¹ of data from the ATLAS detector*, ATLAS-CONF-2012-097 (Jul, 2012).
- [108] **ATLAS** Collaboration, *Performance of Missing Transverse Momentum Reconstruction in ATLAS with 2011 Proton-Proton Collisions at $\sqrt{s} = 7$ TeV*, ATLAS-CONF-2012-101 (Jul, 2012).
- [109] "<https://twiki.cern.ch/twiki/bin/view/atlasprotected/topcommonscales>."
- [110] *Geant4—a simulation toolkit*, *Nuclear Instruments and Methods in Physics Research Section A: Accelerators, Spectrometers, Detectors and Associated Equipment* **506** (2003), no. 3 250 – 303.
- [111] "<https://twiki.cern.ch/twiki/bin/viewauth/atlasprotected/topmc11>."
- [112] S. Frixione, P. Nason, and C. Oleari, *Matching NLO QCD computations with Parton Shower simulations: the POWHEG method*, *JHEP* **0711** (2007) 070, [arXiv:0709.2092].
- [113] P. Z. Skands, *Tuning Monte Carlo Generators: The Perugia Tunes*, *Phys.Rev.* **D82** (2010) 074018, [arXiv:1005.3457].
- [114] M. L. Mangano et al., *ALPGEN, a generator for hard multiparton processes in hadronic collisions*, *JHEP* **0307** (2003) 001, [hep-ph/0206293].
- [115] Pumplin, J. and others, *New generation of parton distributions with uncertainties from global QCD analysis*, *JHEP* **07** (2002) 012, [hep-ph/0201195].
- [116] **ATLAS** Collaboration, *Measurement of the charge asymmetry in top quark pair production in pp collisions at $\sqrt{s} = 7$ TeV using the ATLAS detector*, *Eur. Phys. J.* **C72** (2012) 2039, [arXiv:1203.4211].
- [117] **ATLAS** Collaboration, *ATLAS tunes of PYTHIA 6 and Pythia 8 for MC11*, ATL-PHYS-PUB-2011-009, ATL-COM-PHYS-2011-744 (2011).

-
- [118] **ATLAS** Collaboration, *Measurement of the top quark-pair production cross section with ATLAS in pp collisions at $\sqrt{s} = 7$ TeV*, *Eur.Phys.J.* **C71** (2011) 1577, [arXiv:1012.1792].
- [119] U. Langenfeld, S. Moch, and P. Uwer, *Measuring the running top-quark mass*, *Phys.Rev.* **D80** (2009) 054009, [arXiv:0906.5273].
- [120] **ATLAS** Collaboration, *Differential top–antitop production cross-section measurements in pp collisions at $\sqrt{s} = 7$ TeV as a function of pseudo-top-quark observables in the single-lepton channel using the ATLAS detector*, ATLAS-CONF-2014-059 (Oct, 2014).